General Perturbations Methods for Orbit Propagation with Particular Application to Orbit Lifetime Analysis

Emma Kerr

Supervised by: Malcolm Macdonald

Department of Mechanical and Aerospace Engineering
University of Strathclyde

This dissertation is submitted for the degree of
Doctor of Philosophy

December 2018

Declaration

This thesis is the result of the author's original research. It has been composed by the author and has not been previously submitted for examination which has led to the award of a degree.

Emma Kerr
December 2018

Acknowledgements

Taking on and completing a PhD is not an easy task, it takes a village, so there're many people I need to thank for helping me along the way. Firstly and most importantly, to Malcolm, my supervisor, for your patience and understanding during a difficult time, and your seemingly never ending comments and edits; which, though difficult to disgest at times, made me a better engineer and ultimately got me to this stage. Next, to my family for your love and support, and for not asking the dreaded question too often (how's the PhD going?). To my team, for all the times you've answered my (sometimes) stupid questions, and helped me figure out why Matlab hates me; particularly to my Matlab guru, without your supreme googling abilities I'm not sure I would have ever got my code working. To the many friends I've made along the way, you've read and reread my papers, listened to me practice presentations and of course listened to me rant about how horrible it all is. For all the times you commiserated with me when I had problems and celebrated with me when things go well... even if it was just a piece of code finally working, I never would have finished this thing without you, so thank you all. To two friends in particular, you know who you are, thank you both for the catch-ups where you talked me out of giving up (and occasionally into another glass of wine), and for all the times you've been a sanity check or a sounding board for my crazy ideas. To the new friends I've made in Australia in my last few months, thanks for helping to get me over the finish line with my sanity (mostly) intact. Finally, to everyone I've had the pleasure to work with over the past few years, you made work fun and I'll never be able to thank you enough for that.

Abstract

The average number of spacecraft launched per year has recently and rapidly increased, a trend largely the result of the increased use of small and micro-satellites, platforms such as the CubeSat. This growth trend is unlikely to reverse in the near-term. To mitigate the risk that spacecraft pose to the availability and accessibility of the space environment, space debris mitigation standards currently recommend that spacecraft be removed from low-Earth orbit within 25 years of end-of-mission. In order to prove compliance with these standards, spacecraft operators must demonstrate the evolution of their spacecraft's orbit through the use of orbit propagation software. The aim of this thesis is to improve understanding and accuracy of general perturbations methods for orbit propagation. This thesis tackles this challenge from two different angles. Firstly, the general perturbations method itself is derived using modern mathematical toolsets. Secondly, the input parameters are addressed, these include atmospheric density and ballistic coefficient.

A new parameter is introduced, termed the density index, which enables the solar activity cycle to be captured in a new analytical atmospheric density model. Consequentially, a new solar activity model is developed that uses a single independent variable per solar cycle to describe the solar activity across that cycle, as indicated by the $F_{10.7}$ index. This density index is applied to a new analytical spherically-symmetrical model for atmospheric mass density. When combined with the newly derived general perturbations method for orbit propagation, validation against historical data shows an improvement in orbit lifetime estimates from an average error of 50.44 percent with a standard deviation of 24.96 percent, to an average error of 3.46 percent with a standard deviation of 3.25 percent when compared with the method developed by King-Hele and co-authors including an averaged atmospheric mass density (not including solar activity effects). Furthermore, the new method with the new analytical spherically-symmetrical atmospheric model and solar activity models applied is found to compare favourably against other general and special perturbations methods, including third party, and commercial software, the most accurate of which was found to have an average error of 6.63 percent and standard deviation of 7.00 percent.

The spherically-symmetrical atmospheric model is also extended to include an analytical non-spherically-symmetrical atmospheric density companion model. This improvement allows the method to be applied with confidence to highly inclined orbits and special cases such as sun-synchronous orbits where the inclusion of the effects of atmospheric oblateness and the diurnal bulge will be particularly significant. Using a case study of a sun-synchronous satellite a comparison is drawn between the models, showing that by capturing the effects of a non-spherically-symmetrical atmosphere the orbit lifetime predicted could be up to 10 percent different than when using the spherically-symmetrical model. It is noted that the inclusion of the non-spherically-symmetrical model is less important than the inclusion of the solar activity model.

A new method of determining the average projected area of a randomly tumbling CubeSat is presented, which improves on the accuracy of the method recommended in Section 6.3 of the ISO standard 27852:2010(E). For the range of CubeSat configurations presented it can be seen that the new method improves the error in the average projected area from, approximately 27 percent to within 5 percent. It is of particular note that the ISO standard is found to consistently overestimate the average projected area when considering non-cuboid spacecraft configurations, meaning that when applied to an orbit decay model it will consistently underestimate the orbit lifetime.

A further improvement to the general perturbations method is suggested, using spacecraft orbit decay tracking data to inform orbit predictions. The decay data is used to derive the ballistic coefficient input parameter in order to make the method independent from error in this input. The accuracy of the method including decay data is validated against the original method using historical data.

Finally, some applications of the developed methods are presented, including launch window selection, and post operations predictions. The most notable result of the presented applications is, however, in collision risk analysis. A popular de-orbit concept due to its simplicity is drag augmentation, the use of a deployable surface to increase atmospheric friction. Such concepts have received notable attention, with various funding bodies and licensing authorities supporting technology and flight demonstrations, as well as in the specialist and popular media. However, studies lack a full analysis of the implications of increasing projected area on collision risk, focusing principally on time to de-orbit and assuming a direct correlation with collision risk. Using the volume swept (equivalent to area-time product) during de-orbit as a metric for collision risk it is shown that, contrary to the widely held belief, drag augmentation typically increases collision risk. It is shown that if applied in the worst-case scenario, specifically at the wrong time during the solar activity cycle, drag augmentation can increase the collision risk by an order of magnitude. The legal implications of this are briefly considered, and it is shown that spacecraft operators who inappropriately deploy a drag augmentation device could be argued liable for any subsequent on-orbit collision. As such the viability of drag augmentation as a simple, low-cost end-of-mission spacecraft removal device is diminished and it is anticipated that licensing authorities need to reconsider future and prior approval to deploy such devices.

Table of contents

List of figures

List of tables

Nomenclature

Roman Symbols

e	Exponential operator
A	Variable derived in curve fitting, see equation 3.2
a	Semi-major axis
B	Variable derived in curve fitting, see equation 3.2
B'	Simplification factor, see equation 2.64
B^*	Variation on ballistic coefficient
BC	Ballistic coefficient
c	Variable derived in curve fitting, see equation 3.11
C_D	Coefficient of drag
D	Drag force
DI	Density Index
E	Eccentric anomaly
E_m	Error in orbit lifetime prediction using multiple curve atmospheric density model
E_s	Error in orbit lifetime prediction using single curve atmospheric density model
F	Atmospheric rotation factor
f_T	Component of atmospheric drag in the instantaneous direction of travel
$F_{10.7}$	Index measuring SFU apparent at the 10.7 cm wavelength

g	Acceleration due to gravity
H	Atmospheric density scale height
h	Altitude
I	Integral form of the Modified Bessel function
i	Inclination
k	Simplification factor, see equation 2.26
m	Spacecraft mass
N	Number of viewpoints used in area averaging
P	Variable derived in curve fitting, see equation 3.10
p	Semi-latus rectum
R	Coefficient of determination
r	Position vector of spacecraft
r_p	Radius of perigee
S	Projected area of a spacecraft perpendicular to the direction of travel
S_C	Projected area of a CubeSat
S_{ISO}	Projected area of a spacecraft estimated using ISO standard
SF	Solar Flux
SSN	Sunspot Number
T	Orbit period
t	Time
t_s	Local mean solar time
v	Velocity of a body in orbit
x	Simplification factor, $x = a\varepsilon$
y	Simplification factor, see equation 2.57

z	Simplification factor, $z = \beta x$

Greek Symbols

α	Variable derived in curve fitting, see equation 3.5
β	Inverse of density scale height
χ	Variable derived in curve fitting, see equation 3.3
Δ	Denotes change in succeding parameter
δ	Simplification factor, see equation 2.3
Γ	Gamma function
γ	Variable derived in curve fitting, see equation 3.5
κ	Variable derived in curve fitting, see equation 3.5
μ	Standard gravitational parameter of the central body
Ω	Right ascension of the ascending node
ω	Argument of periapsis
ω_A	Rotational velocity of the atmosphere
ϕ	Variable derived in curve fitting, see equation 3.6
π	Constant, 3.14...
ψ	Variable derived in curve fitting, see equation 3.6
ρ	Atmospheric density
σ	Standard deviation
τ	Orbit Lifetime
θ	True anomaly
υ	Variable derived in curve fitting, see equation 3.6
ε	Eccentricity
φ	Variable derived in curve fitting, see equation 3.4

ξ	Variable derived in curve fitting, see equation 3.6

Acronyms / Abbreviations

^{14}C	Carbon-14
CIRA	COSPAR International Reference Atmosphere
CNES	French National Centre of Space Research
COSPAR	Committee on Space Research
DTM	Drag Temperature Model
ESA	European Space Agency
GEO	Geostationary Earth Orbit
GMAT	General Mission Analysis Tool
GRAM	Global Reference Atmosphere Model
GTO	Geostationary Transfer Orbit
IADC	Inter-Agency space Debris coordination Committee
ISO	International Organisation for Standardisation
JB	Jacchia-Bowman
K-H	King-Hele
LEO	Low Earth Orbit
MK-H	Modified King Hele
MSISE	Mass Spectrometer and Incoherent Scatter Radar Exosphere
NASA	National Aeronautics and Space Administration
NOAA	National Oceanic and Atmospheric Administration
NORAD	North American Aerospace Defense Command
NRLMSISE	US Naval Research Laboratory Mass Spectrometer and Incoherent Scatter Radar Exosphere

SFU	Solar Flux Units
SODA	Solar Dynamo Amplitude
STELA	Semi-analytical Tool for End of Life Analysis
STK	System Tool Kit
TLE	Two Line Element
UN	United Nations

Chapter 1

Introduction

The modern world is fundamentally dependent on satellite applications; everything from our communications and TV services to the monitoring of crop yields, forest fires or coastal erosion is reliant on satellite applications. Satellite based systems are used all around the world and the increasing demand for satellite applications means that more and more spacecraft are being launched into Earth orbit without any universal regulations on post mission disposal. This means that spacecraft can be launched, used and then just left in orbit. These defunct spacecraft pose real danger to live missions. Recently, however, there has been a push towards sustainability as more people are becoming aware of the space debris problem: if more spacecraft are launched without actively removing any, space is going to get relatively crowded, very quickly. In order to facilitate this move towards sustainability this work outlines general perturbations methods for orbit propagation that can be used both to model current space debris and predict the orbit lifetimes of objects given a set of initial conditions such as launch date and initial orbit parameters. The method developed includes analytical solar activity and atmospheric density models along with the general perturbations model for orbit lifetime analysis. The method provides accuracy and is computationally inexpensive and affords operators the opportunity to mitigate the potential risk their spacecraft will pose post-mission.

1.1 Space Debris and the Mitigation Guidelines

The space debris problem is one that has grown from a lack of foresight, or perhaps of knowledge, on the part of the original spacefarers. The first satellites were launched by the Soviet Union and the United States of America, during the cold war. Space was a new frontier and as such had no laws governing its use, so neither party had to consider the future. However, over the years a series of treaties have been drafted to regulate the uses of space.

There are five major international treaties on the uses of space; including the number of countries who have ratified (note ratification means parties are officially bound by the treaty), these are:

1. The Outer Space Treaty: "Treaty on Principles Governing the Activities of States in the Exploration and Use of Outer Space, including the Moon and Other Celestial Bodies"[4]
    - Adopted by the General Assembly in its resolution 2222 (XXI)
    - Opened for signature on 27 January 1967, entered into force on 10 October 1967
    - 105 Ratified[5]
2. The Rescue Agreement: "Agreement on the Rescue of Astronauts, the Return of Astronauts and the Return of Objects Launched into Outer Space"[6]
    - Adopted by the General Assembly in its resolution 2345 (XXII)
    - Opened for signature on 22 April 1968, entered into force on 3 December 1968
    - 95 Ratified[5]
3. The Liability Convention: "Convention on International Liability for Damage Caused by Space Objects"[7]
    - Adopted by the General Assembly in its resolution 2345 (XXII)
    - Opened for signature on 22 April 1968, entered into force on 3 December 1968
    - 94 Ratified[5]
4. The Registration Convention: "Convention on Registration of Objects Launched into Outer Space"[8]
    - Adopted by the General Assembly in its resolution 2345 (XXII)
    - Opened for signature on 22 April 1968, entered into force on 3 December 1968
    - 63 Ratified[5]
5. The Moon Agreement: "Agreement Governing the Activities of States on the Moon and Other Celestial Bodies"[9]
    - Adopted by the General Assembly in its resolution 34/68
    - Opened for signature on 18 December 1979, entered into force on 11 July 1984
    - 17 Ratified[5]

None of these treaties specifically mentions removal of objects launched into space. As with many new frontiers, particularly those born out of war, the focus of the regulations developed to deal with the situation was the immediate challenges posed. In the case of the space regulations, the issue was the use of space for the purposes of war and issues such as the treatment of astronauts who unintentionally land in the wrong place. The space debris problem was not yet a concern, as very few objects were being launched at the time the regulations were being written. However, as space technology developed, new applications were discovered and costs came down; essentially as space became an industry instead of a two-party state-funded and state-run enterprise, new regulations have not been developed to keep up with advancements. The only treaty that, at least in-part, deals with space debris is the Liability Convention. Though untested, Article III of the Liability Convention could be used to argue liability for on-orbit collisions, if fault can be established.

One potential reason for the lack of law development is that space debris is arguably not actually a problem yet because of one fundamental assumption: space is big. While this is true, space is vast, objects in space move very quickly. An object in low Earth orbit, LEO (0-2000 km altitude), travels with a forward velocity of approximately 7-8 km/s. This means that objects in LEO could collide with a relative velocity of up to 16 km/s. There is no way in which a spacecraft could be protected from such a collision, the result would be disintegration of both objects creating a cloud of debris travelling at similar speeds. This cloud would likely go on to create further collisions. A theory on this matter was developed by Donald J. Kessler, known as the Kessler effect or Kessler syndrome. Kessler projected that eventually there would be a high enough density of objects in LEO that a collision between objects could cause a cascade in which each new collision, creating new space debris, would increase the likelihood of further collisions. The implication of this theory is that someday the distribution of debris left behind by the cascade of collisions could render entire orbital regimes useless for future space activities. This phenomenon was demonstrated quite effectively for the general public in the 2013 motion picture ‘Gravity’.[10]

Plotting the trend in the number of objects in space shows a relatively steady increase, see Figure 1.1. While there is some variation in the types of objects, the general trend is a clear gradual increase in the total object count. Note the unknown objects in Figure 1.1 denote the objects which had not yet been identified when this figure was produced.

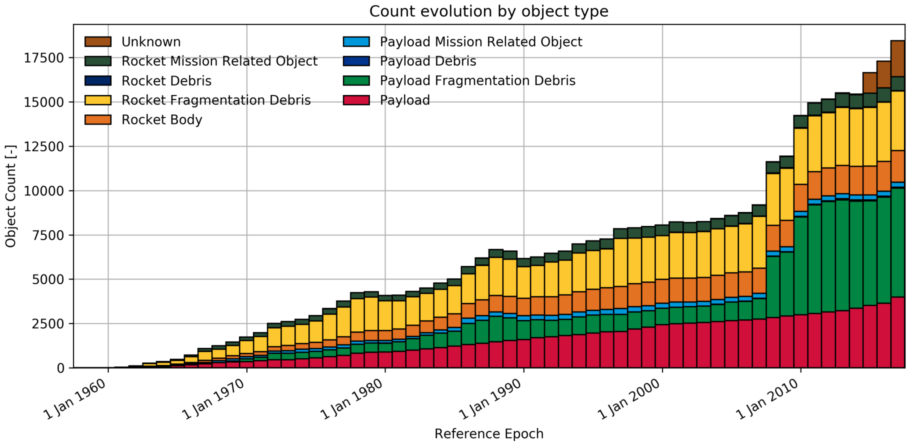

Fig. 1.1 Space Debris Evolution; Image Credit: ESA

There are two notable jumps in the total object count, these occurred in 2007 and 2009, corresponding to the Fengyun anti-satellite test carried out by the People's Republic of China and an accidental orbital collision of two satellites respectively. This collision occurred between the defunct Russian Kosmos2251 military satellite and the operational U.S. Iridium-33 communications satellite at approximately 11.7 km/s.[11] In both the anti-satellite test and the accidental collision the result was the same; the satellites were destroyed and thousands of pieces of debris were generated, some of which have since re-entered. Over the years the U.S. space surveillance network has cataloged over 25,000 objects larger than 10 cm in diameter, there are currently approximately 8,500 objects that are regularly tracked, of which it is estimated that only around 7% are operational satellites.[12] It is estimated that there are on the order of hundreds of thousands or even millions of objects which are untrackable, and yet potentially very dangerous. For example, in May 2016 a window on the International Space Station had to be replaced after a fleck of paint collided with and cracked it. However, since to date there has only been one accidental collision resulting in the total loss of an operational spacecraft it can still be argued that space debris is not an immediate danger, simply a nuisance, so it is difficult to encourage the adoption of mitigation measures, which may restrict mission parameters or drive up costs.

Another major reason for the lack of law development is that, as the possibilities of space expand, many countries begin to protect their own interests; take for example the recent "U.S. Commercial Space Launch Competitiveness Act" passed in the United States allowing companies to mine and own minerals from asteroids.[13] Many, though not all, in the space law community argue that this fundamentally breaks with the intent of the outer space treaty, as the treaty suggests that space should not be used for the gain of any one country: the preamble of the outer space treaty states "*Believing that exploration and use of outer space* *should be carried on for the benefit of all peoples irrespective of the degree of their economic or scientific development*". Furthermore, there is a general belief that the 'age of treaties' is over.

Space activities have become more diverse and new players have emerged, and so the world today is very different than it was when the five treaties were first drawn up. There is now a move towards legislation at a national level; at the beginning of 2017 the United Nations had listed 22 countries that have their own legislation relating to space activities, however this list only includes countries who have registered their laws with the United Nations. The SpaceLegalTech website run by the Toulouse Business School had, however, tracked 18 countries with comprehensive space laws, a further 13 with specific laws relating to space activities, and another 14 with legislation in progress.[14] So there is progress on the national front. In national legislation it is possible for countries to cherry pick which things to legislate. This means that while at least some law is being written, many countries acting in the space industry still have no national legislation, beyond whichever UN treaties they have chosen to ratify.

Besides the UN treaties and national legislation, there are also what are known commonly as best practice guidelines. In these can be found the first mention of space debris in legal terms. The most important, and relevent in view of this thesis, of these guideline documents are the Inter-Agency Space Debris Coordination Committee (IADC) "Space Debris Mitigation Guidelines", and the International Organisation for Standardisation (ISO) "Space systems - Space debris mitigation requirements".[15,16] Both of these documents focus on two major areas of mitigation; firstly they discuss avoiding the intentional release of debris during nominal operations and avoiding break-ups, and secondly they discuss the post mission disposal of spacecraft. The section on avoiding intentional release is fairly straight forward; it is recommended that there be no intentional release of debris, however if necessary the recommendation further stipulates that debris should be released in such a manner that it exits the protected orbital regions detailed in the guidelines: Low Earth Orbit (LEO) and Geostationary Earth Orbit (GEO). The protected LEO region is defined as the spherical region from the surface of a spherical Earth of radius 6378 km to 2000 km altitude. The protected GEO region is defined as the segment of the spherical shell from 200 km below to 200 km above the geostationary altitude (approximately 35786 km) and from -15° to 15° latitude. The section on avoiding break-ups discusses probabilities of break-ups and passivation of the spacecraft, such that the risk of break-up should be kept as low as possible. Finally, the sections on post mission disposal suggest that a spacecraft should be removed within 25 years of decommissioning if it travels through either of the protected regions. Though the current versions of the guidelines use 25 years from decommissioning as the standard for post mission disposal, future revisions are likely to reduce this period. It is also discussed that, if re-entry is to be attempted, it should be done in such a way to minimise potential risk to life and property. This means that larger spacecraft which are likely to survive re-entry, at least in part, should perform a controlled re-entry with an impact zone away from populated areas. Both documents also recommend that a space debris mitigation plan be established and documented for each project undertaken.

The ISO and IADC, and/or other, best practice guidelines have been written into law in certain countries, such as France. If enough countries follow suit it is possible that these guidelines could become customary international law, meaning all space actors would have to consider them. Typically, these guidelines have been written by engineers rather than lawyers, thus their focus is on the technical requirements, rather than legal issues. As such, in some cases, engineers choose to follow them regardless of the legislation, for moral reasons if not legal necessity.

The ISO and IADC space debris mitigation guidelines specify a time period in which spacecraft must be removed. Therefore, in cases where active removal methods are not employed, orbit propagation must be used to generate predictions on when a spacecraft will exit the protected regions naturally due to orbit evolution.

1.2 Orbit Propagation

Orbit propagation is one of the fundamental challenges in orbital mechanics, with many forces disturbing perfect orbital motion. The factors affecting this motion include everything from solar activity and geomagnetic activity to the oblateness of the Earth. Propagation of an orbit essentially allows a user to predict the future position of an object in-orbit. The perturbation forces, such as atmospheric friction (commonly referred to as 'atmospheric drag'), must be captured in the orbit propagation in order for the method to accurately predict the future position of an object. The more perturbation forces included, the more accurate the propagation method will be.

Over the years many attempts have been made to develop propagation methods. These methods fall into two main categories: general and special perturbations methods, which are often colloquially known as analytical and numerical methods respectively.

While numerical methods have been studied extensively and are generally considered more accurate, this accuracy comes at the cost of time and/or computing power. Numerical methods iterate over many steps, meaning large volumes of data are generated and the method becomes computationally expensive and thereby potentially time-consuming. As computing technology evolves numerical methods have become less time-consuming but they will never be as computationally efficient as an analytical solution. Analytical solutions are computationally inexpensive but are heavily reliant on accurate input parameters. Typically, analytical methods are constructed by focussing on specific situations, such as the particular orbit that a object is in, then making simplifications such as ignoring less influential perturbations. In this way the problem can be simplified so that an equation can be designed to approximate the motion of the object.

A further two options should also be considered: third party software, and graphical or look-up methods, which are both derivatives of general and special perturbations methods. Both of these options as well as general and special perturbations methods are discussed in more detail in the following sections.

1.2.1 Special Perturbations

The typical special perturbations method for orbit lifetime analysis involves propagating an orbit in steps, using the output of the first iteration to inform the input of the second and so on. Purely numerical solutions generally model a perfect Keplerian orbit, then add perturbations, such as atmospheric drag or third body perturbations, to reflect the actual motion. However, there are some exceptions to this, semi-analytical methods for example do not follow this model.

Semi-analytical and Semi-numerical solutions are solutions that attempt to capture the best of both general and special perturbations solutions, by being both fast and reliable. Semi-analytical methods are generally stepped versions of purely analytical solutions, i.e. they take an analytical solution for the whole orbit lifetime and apply it over a series of steps breaking the propagation into smaller steps. This increases the time required to find a solution but makes including time-variant perturbations such as atmospheric drag much easier, thereby theoretically increasing accuracy. Semi-numerical solutions are similar to semi-analytical, however they start with a numerical solution and decrease the number of integration points in order to speed up the solution at the cost of some accuracy.

1.2.2 General Perturbations

General perturbations methods are perhaps the simplest methods, they generally rely on a single equation or set of equations that describe orbital motion. The perturbation forces included vary from method to method. However, there is one commonality to all general perturbations methods, they rely heavily on the accuracy of their input parameters. Since a single equation is used to propagate an orbit, from the start to the end of the orbital life of a spacecraft, the input parameters have large significance and as such small errors in these parameters can have relatively large effects on the predictions made. These input parameters are: the orbit parameters, the spacecraft geometry, mass and drag coefficient, and the atmospheric density. Of these, only the orbit parameters are fixed. If the spacecraft is thrusting the mass will vary with time, though typically the mass-time relationship is well defined based on the propulsion method included. If the spacecraft is spherical then the area would be known, however spherical spacecraft are rare. Therefore, there are four basic uncertainties in the input parameters which must be considered: the spacecraft mass, area and drag coefficient, and the atmospheric density. This thesis aims to address the uncertainties in area, drag coefficient and atmospheric density and thereby improve the accuracy of general perturbations methods.

1.2.3 Third Party Software

Since orbit propagation is a relatively specialised task many companies looking to launch a spacecraft may not have the expertise in house to complete it. However, over the past decade or so many software solutions, some of them commercial, have become available. These software solutions can be used to complete orbit propagation without requiring specialised knowledge. While most software solutions are based on numerical methods, there are a few exceptions such as STELA (Semi-analytical Tool for End of Life Analysis) developed by the French National Centre of Space Research, CNES, which, as the name states, is based on a semi-analytical method. These software solutions range in price and accuracy depending on the methods embedded.

1.2.4 Graphical and Look-up Table

Look-up methods are very rarely used as they are typically too generalised to be widely useful. Graphs and tables are created using general or special perturbations methods for prototypical spacecraft of designated mass in designated orbits. They can be used effectively to give approximate results without performing any calculations, however an accurate result would require custom built graphs and tables. Custom building graphs means the user must employ a general or special perturbations method with uncertainties attached to the input parameters.

1.2.5 Accuracy Comparison

The easiest way to demonstrate the accuracy comparison of analytical and numerical methods is to view them on a schematic, see Figure 1.2.

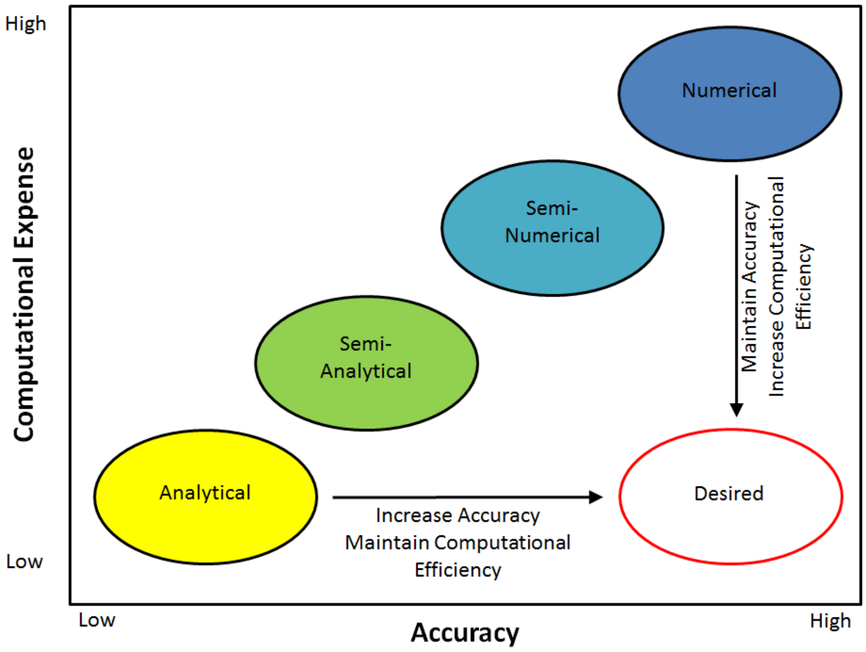

Fig. 1.2 Orbit propagation method accuracy trade-off schematic

Moving from left to right in Figure 1.2 the accuracy increases and from bottom to top the computational expense increases. Figure 1.2 shows the typical position of the various methods on the schematic, however, the position of each of the numerical methods is dependant on the fidelity of the integrator employed in each. The desired state for a method is to be computationally inexpensive while delivering accurate results. In order to achieve the desired state beginning with a numerical solution, accuracy must be maintained while somehow decreasing the computational expense. Currently, the only way to decrease the computational expense of a numerical method is by decreasing the fidelity, however, this also decreases the accuracy. Therefore, considering instead an analytical solution; by improving the solution, for example by removing simplifications made in the derivation or removing uncertainties in the input parameters, the accuracy of the method can be increased without increasing the computational expense. Thus, the desired state can be achieved. Following this reasoning, the work presented in this thesis focusses on improving analytical methods in order to achieve the desired state.

1.3 Applications of General Perturbations Methods

Once a method has been validated it could be used in many areas, however there are three areas where the use of general perturbations methods for orbit lifetime analysis could be very effective. These are; space debris mitigation regulatory compliance assessment, space debris analysis and orbit catalogue propagation, and mission analysis. The particular strength of a general perturbations method is that it can be used in a Monte Carlo analysis to rapidly find solutions for cases where input parameters are still in question or are simply unknown. The addition of a Monte Carlo analysis to an already computationally expensive numerical method is impractical.

1.3.1 Space Debris Mitigation Regulatory Compliance

A fully validated method is essential for space debris mitigation regulatory compliance assessment. An operator could use either general or special perturbations methods. However, the simple mathematical relationships in general perturbations analysis can be helpful. For example, an operator wishing to find out the maximum allowable altitude from which their spacecraft will decay with the 25 year period could simply reverse their calculations, setting the lifetime to 25 years and rearranging to find the initial altitude. Furthermore, a Monte Carlo analysis can be used with the general perturbations method to deal with uncertain parameters such as solar activity, which is notoriously difficult to predict beyond a few years into the future. Compliance assessors, who may be dealing with large volumes of objects to assess, could also benefit from the computationally inexpensive nature of a general perturbations method.

1.3.2 Space Debris Analysis and Orbital Catalogue Propagation

Space Debris Analysis and Orbit Catalogue Propagation share one major challenge, volume. For space debris analysis, some input parameters, such as mass or drag coefficient, may be unknown so must be considered using ranges, for example by applying a Monte Carlo analysis. Then for orbit catalogue propagation, as discussed in Section 1.1 there are tens of thousands of objects in orbit being tracked at any given time. In both cases general perturbations methods are ideal as they require very little time to run high volume analyses.

1.3.3 Mission Analysis

Much like in space debris analysis, in mission analysis sometimes parameters are left open, for example launch date. Using a Monte Carlo analysis on a general perturbations method could inform the mission plan, particularly issues such as geometry and launch date which have an impact on the mission lifetime. Essentially mission analysis can be treated as one large trade-off analysis problem, however often factors involved in the trade-off are interdependent thus having an efficient and accurate means of narrowing the field of possibilities is vital.

1.4 Review of General Perturbations Methods in the Literature

As previously discussed, both the IADC and ISO mitigation guidelines state that a spacecraft should be removed within 25 years of decommissioning if it travels through either of the protected regions detailed in the guidelines: LEO and GEO.[16,15] This guideline of removal within 25 years means that, in cases where active removal is not applied, in order to prove compliance prior to launch an operator must complete an orbit lifetime assessment to generate predictions on when their spacecraft will exit the protected regions. This analysis could be completed using any of the methods previously discussed. A further standard has been generated by ISO discussing the estimation of orbit lifetime.[17] This standard and the work done to develop it, particularly the work by Oltrogge and Chao, discuss the advantages and disadvantages of three different methods for orbit lifetime estimation and give guidance on how to use each method effectively.[18] The methods detailed are high precision numerical integration, rapid semi-analytical orbit propagation, and numerical table look-up analysis and fit formula evaluations. There is, however, one further method not considered, general perturbations methods. This method is often dismissed for long-term orbit propagation due to problems with accuracy.[19] In the ISO standard for orbit lifetime estimation (ISO27852) heavy emphasis is placed on the numerical methods as the most reliable, even the name with the addition ‘high precision’ suggests these methods should be used, however without a systematic validation this conclusion should not be drawn.

Primary body atmospheric drag acts against the velocity vector resulting in a reduction in orbit energy, and hence semi-major axis. Consequently, it is the principal contributor to artificial satellite orbit decay in Earth orbit below 1000 km altitude. The magnitude of this frictional force is directly proportional to the atmospheric density, which is intrinsically time-variant due to the influence of solar activity, leading to significant variations in the atmospheric density over time at even the same altitude.[20] Naasz, Berry, and Schatten use propriety third-party software, applying special perturbations, to show the impact that variations in solar activity have on satellite orbital lifetime predictions, confirming the correlation between high solar activity levels and shorter orbit lifetimes, and conversely low solar activity levels and longer orbit lifetimes.[21] Vallado and Finkleman extend that work to consider the effect of solar cycle variations on orbit lifetime predictions, once again applying special perturbations methods to find a direct relationship between solar activity and orbit lifetime.[22] More specifically, they found that solar activity was the largest contributor to variation in atmospheric density at a fixed altitude. Consequently the effect of solar activity cannot be neglected. However, general perturbations methods taking into consideration atmospheric drag have commonly neglected solar activity, leading to a significant lack of accuracy in such methods.

Vallado and Finkleman also discuss the solar radio flux at wavelength 10.7 cm (2800 MHz), the $F_{10.7}$ index, which is commonly used as an indicator of the solar activity level, and its use in empirical models of atmospheric density, finding that it is the most suitable proxy for solar activity.[22]

The most commonly cited general perturbations method for predicting the orbital lifetime of low-eccentricity satellites in the presence of a time-invariant and spherically symmetrical retarding atmosphere is the method presented by Cook, King-Hele and Walker but later expanded by King-Hele herein referred to as the 'King-Hele method'.[23,24] This method is based on power series expansions of the eccentricity, semi-major axis and eccentric anomaly. It is also worth mentioning that there are many other methods of orbit lifetime prediction such as that presented by Swinerd and Boulton, who adopt Cook, King-Hele and Walker's power expansion method and produce orbital lifetime equations incorporating the effect of atmospheric oblateness with diurnal density variations.[25] Griffin and French also build on the work of Cook, King-Hele and Walker introducing a new equation for the orbit lifetime of spacecraft in initially circular orbits.[26] In a series of papers Sharma takes a different approach, using K-S elements to build the analytical solution for orbit lifetime prediction.[27–30] Sharma first explores a basic method with test cases covering the eccentricity range from 0.001 to 0.1. The method is then improved by expanding to include higher order terms with test cases with eccentricities in the range 0.001 to 0.8. Martinusi, Dell'Elce and Kerschen have demonstrated an averaging technique used to obtain a first-order approximate solution for the motion of a satellite in low Earth orbit.[31,32] However, no author has published so extensively, and with such a thorough approach, as King-Hele and his various co-authors, who over the years have systematically presented papers detailing the impact of various effects on the orbit decay of satellites in Earth orbit. An 8-part series of papers titled "The Contraction of Satellite Orbits Under the Influence of Air Drag" explores various effects and the corresponding orbit lifetime prediction methods dealing with these effects. Part 1 in the series introduces a basic method for orbit lifetime prediction of satellites in low eccentricity ($\varepsilon < 0.2$) orbits, which is then expanded in part 2 to address the issue of an oblate atmosphere.[24,33] Part 3 addresses higher eccentricity orbits $(0.2 \leq \varepsilon < 1)$.[34] Part 4 builds on part 1 to include the effect of variations in scale height with altitude.[35] Then part 5 builds on part 2 to include the day-to-night variation in atmospheric density.[36] Part 6 builds on part 5 looking in more depth at the effects of day-to-night variation in density on near-circular orbits.[37] Part 7 combines work from parts 3 and 5 by examining the effects of altitude varying scale height on high eccentricity orbits.[38] Finally, part 8 looks at how perturbations due to odd zonal harmonics of the geopotential affect the orbit lifetime of a satellite in an oblate atmosphere.[39] It is noteworthy that despite this detailed and methodical approach the effect of solar activity was not addressed in this series of papers. Another important point of interest is that in many cases general perturbations methods are not validated. The lack of validation could be due to the lack of available data required for validation at the time the methods were developed, however, validation could have been completed as that data became available. Where validation is considered, typically the methods are compared with numerical methods to ascertain their accuracy. There is, in this comparison, an inherent presumption that the numerical method is accurate, however numerical methods are still approximations, though to a lesser degree than analytical models, and are therefore subject to error when compared to real cases.

It is worth noting the promising results from Barrio and Palacián; they propose a method for orbit lifetime analysis of high eccentricity orbits based on Lie transformations.[40] The results suggest their theory may be useful in simulating geosynchronous transfer orbits. The work of Titov, Burt and Josyula is also of interest as they demonstrate the importance of understanding the accuracy of input parameters and their uncertainties.[41] They particularly focus on quantifying uncertainties in the computed flow parameters from a hypersonic aerothermodynamic particle implementation of a direct simulation Monte Carlo solution for spacecraft drag. They show that uncertainties in the atmospheric density input parameter are the main contributor to uncertainty in the drag force; however no consideration was given to separating the solar activity as a source of uncertainty. They also discuss propagating the input parameter uncertainties through the model to produce an estimate of the contribution to the resulting output uncertainty.

To the best of the author's knowledge, the only attempt made to consider the effect of solar activity in general perturbations methods was made by King-Hele and Walker.[42] They incorporate the solar activity using a so-called 'solar cycle factor', which is a basic correction factor applied to the orbit lifetime estimate after the prediction (neglecting solar activity) has been made. While this method could be employed for approximate calculations, it does not capture the mechanism by which solar activity affects the spacecraft drag calculation. As such, this method would be unlikely to give reliable results and no validation of the method is available in the literature.

To incorporate solar activity induced variations on atmospheric density the stochastic nature of solar activity must be considered. When this is introduced to the atmospheric density calculation, which in turn is applied to the orbit lifetime calculation, the solution becomes time dependent due to the variability in solar activity, within the current cycle and from cycle to cycle. Therefore, the mission epoch must be considered.

Modelling the solar activity cycle accurately is critical to gaining an accurate model for atmospheric density. Considerable attention has been given to predicting variations in the solar activity cycle. For example, Schatten has published extensively in collaboration with various authors on the solar activity cycle and solar activity.[43–46] To studying the solar activity cycle in general terms, many authors have focused specifically on the shape of the cycle and its apparent deviation from a typical periodic sinusoidal.[47–49]

The magnitude of the force created by drag is directly proportional to the atmospheric density at the orbit altitude.[20] However, this property is notoriously difficult to predict as the atmosphere varies in shape and size due to many effects including, but not limited, to solar activity, geomagnetic activity, atmospheric oblateness and time-dependent variations such as the diurnal variation. The omission of these effects means that special cases such as polar and sun-synchronous satellites cannot be assumed to be accurately modelled using a spherically-symmetrical model of the atmosphere as the high inclination and very slow right ascension drift could cause the orbit to experience an abnormal atmospheric density.

Two deviations from the spherically-symmetrical atmosphere are discussed in this thesis; atmospheric oblateness and the diurnal variation. Atmospheric oblateness is the term used to describe the bulge in the atmosphere centred on the equator, caused by the oblateness of the Earth.[19] The diurnal variation is the variation in atmospheric density caused by the relative position of the sun and has a period of one solar day. As the sun moves overhead, i.e. when local mean solar time approaches midday, the atmosphere overhead expands; then as the sun drops lower in the sky the atmosphere overhead begins to contract, reaching full contraction during the nighttime. The variation typically lags behind the sun's movement, with maximum expansion and contraction occuring at approximately 3 p.m. and 3 a.m. local time. The relative motion of the Earth and sun means that this bulge is not always in the same geographic location over the Earth. The bulge is centered on the equator but moves to higher or lower latitudes depending on the relative positions of the sun and Earth.[19]

Various attempts have been made to include the effects of atmospheric oblateness and the diurnal variation in general perturbations analysis. Studies completed by Cook, King-Hele and Walker showed that modifications could be made to orbit lifetime equations to account for these effects.[33,36,37,39] Swinerd and Boulton completed a similar study, this study included both oblateness and the diurnal variation.[25] Sharma completed comparable studies using

K-S elements in place of the power series expansions of semi-major axis, eccentricity and Eccentric anomaly used in Cook, King-Hele and Walker's publications.[27–30] However, to the author's knowledge no attempt has been made to separate the effects into a simple analytical atmospheric density model which could be applied to any general perturbations model.

The magnitude of the primary body atmospheric drag force is directly proportional to the cross-sectional area of a spacecraft. This area is often referred to in the literature as the spacecraft cross-section, however this is not always the case, instead it is the area seen when observing the spacecraft along the velocity vector. When considering non-convex solids, for example a spacecraft with deployable panels, the area required for the atmospheric drag calculation is the area that would be orthographically projected onto a plane perpendicular to the velocity vector. Therefore, herein this area will be referred to as the projected area.

In most cases, the projected area will vary over time depending on an object's attitude control capability or lack thereof. Accurate estimation of atmospheric drag is particularly important when considering spacecraft with longer orbit lifetimes as a small error in an input parameter such as projected area will compound over the orbit lifetime of a spacecraft and create a large error in the orbit lifetime prediction. Therefore, it is paramount to ensure accuracy in the input parameters considered in the atmospheric drag calculation. Estimating the projected area can be difficult especially when considering spacecraft with complex structures and even more so when trying to estimate the area of a spacecraft randomly tumbling. Several methods of calculating the projected area have been presented; the method presented by Ben-Yaacov, Elderman and Gurfil provides the most promise for incorporation into general perturbations methods. It calculates the projected area by projecting each of the individual faces of a spacecraft onto a plane perpendicular to the required view vector then removing any shaded areas.[50] This method allows for the estimation of the projected area of a spacecraft in fixed attitude relative to the velocity vector, however if the spacecraft tumbles this method would be incapable of determining an accurate projected area. In order to apply the projected area of a tumbling spacecraft, to a general perturbations method, a method to calculate the average projected area is required.

To the best of the author's knowledge the only method offering an average 'cross-sectional area' calculation for spacecraft is the ISO standard 27852:2010(E).[17] This standard states that, in lieu of a more detailed numerical integration model, a flat plate model should be used. However, this model is incapable of providing accurate results when considering any configuration other than a cuboid without deployable structures.

The development of orbit lifetime analysis has been given extensive consideration; both general and special perturbations methods have been discussed at length. However, little focus has been given to refining the accuracy of such methods and to the author's knowledge no attempt has been made to incorporate decay data into general perturbations methods.

1.5 Objectives

The aim of this study is to develop methods that can be applied to improve the accuracy of any general perturbations orbit propagation method and validate these using a reliable general perturbations method for orbit lifetime analysis.

The objectives of this study are to:

1. Develop a general perturbations method for orbit propagation.
2. Develop an analytical spherical-symmetrical time-invariant atmospheric model. Then expand this model to be non-spherically-symmetrical, and time-variant by including solar activity, the diurnal effect and atmospheric oblateness.
3. Develop a model for estimating the ballistic coefficient of a spacecraft.
4. Verify and validate the developed models using historical data.

The key contribution to knowledge of this dissertation is new general perturbations methods for orbit propagation. This includes a new general perturbations method for orbit lifetime analysis, an analytical model for solar activity, an analytical atmospheric density model with the option to include the diurnal effect and atmospheric oblateness, and methods of improving the accuracy of the ballistic coefficient input parameter. The separate components of this method could be used in many areas; for example the new atmospheric density model could be used to more accurately model manoeuvres for spacecraft, and the solar activity model could be used to determine the levels of solar radiation impacting spacecraft in orbit. Furthermore, the complete method could be expanded beyond the applications presented herein, with a few minor modifications, for use in many other applications such as long term conjunction assessment or space environment modelling.

1.6 Outline

A brief introduction to general perturbations methods was given in Chapter 1, along with the many factors affecting the accuracy of these methods. The applications for such methods and the reasons for requiring a high level of accuracy from such methods were also discussed. Each further chapter will therefore be a step towards achieving the improvement in accuracy.

Chapter 2 introduces a standard general perturbations method for orbit lifetime analysis, without any adornment. As the most commonly cited general perturbations method, the King-Hele method is initially chosen for validation of the models developed herein. However, the King-Hele method was developed before modern mathematical tools were available, therefore the method was re-derived in Chapter 2. It is found that some modifications can be made, such as removing some of the simplifications made in derivation of the original method.

Chapter 3 explores the atmospheric density input parameter and the factors affecting it. Typically, general perturbations methods fail to include time-variant effects on atmospheric density, such as solar activity. Therefore, in Chapter 3, a new parameter, the 'density index', is introduced to incorporate the effect of solar activity in the calculation of the atmospheric density used in orbit lifetime predictions. A spherically-symmetrical analytical atmospheric density model is derived, with a non-spherically symmetrical companion model addressing the addition of atmospheric oblateness and the diurnal variation. Including atmospheric oblateness and the diurnal variation makes the model more complex, however more widely applicable.

Chapter 4 focuses on modelling the ballistic coefficient of a spacecraft more accurately. The ballistic coefficient is the combination of the mass, projected area and drag coefficient input parameters. With regards to the projected area, when considering non-convex or tumbling spacecraft this area will vary through the orbit lifetime making it challenging to accurately estimate prior to launch. A correction factor for the ISO standard is introduced in Chapter 4 to model the average projected area of a CubeSat to a greater degree of accuracy. This method could, however, be extended to incorporate larger spacecraft. CubeSats offer an interesting test case as they are becoming an increasingly controversial topic in the space community. They have been considered by some simply as debris due to their typically short orbit lifetimes and high failure rates.[51] However, others dispute this classification, in fact companies such as Clyde Space Ltd. and Spire Global, Inc. have shown that CubeSats are a commercially viable platform on which to build a successful business. When dealing with more complex shapes and much larger spacecraft calculating the average projected area is more difficult. The more complex the shape of a spacecraft is, the more likely it becomes that errors in the input parameters will occur. Estimating the drag coefficient can also be problematic as it varies depending on spacecraft geometry and composition, atmospheric conditions and altitude.[17] Drag coefficient and projected area are of course estimated prior to launch, however as a spacecraft decays it is possible to use the decay data to derive them. A method is presented in Chapter 4 to increase the accuracy of orbit lifetime predictions by introducing orbit decay data to try to improve input parameter estimation and thus improve the prediction.

Chapter 5 discusses the validation of each of the models developed in Chapters 2-4. In this chapter the Modified King-Hele method developed in Chapter 2 is applied, with the new atmospheric models from Chapter 3 and ballistic coefficient models from Chapter 4, to a set of historical missions in order to validate the method. Furthermore, an accuracy comparison of the Modified King-Hele method to other orbit lifetime estimation methods is drawn.

Chapter 6 explores some of the applications for general perturbations methods.

Finally, Chapter 7 provides a summary and review of the preceding chapters and outlines future work.

1.7 List of Publications

This section details the papers published by the candidate in support of the application for the degree of Doctor of Philosophy.

1.7.1 Journal Publications

1. Emma Kerr and Malcolm Macdonald. Incorporating Solar Activity into General Perturbation Analysis of Atmospheric Friction. *Journal of Guidance, Control, and Dynamics*, 41(6):1320–1336, jun 2018

2. Daniel KL Oi, Alex Ling, Giuseppe Vallone, Paolo Villoresi, Steve Greenland, Emma Kerr, Malcolm Macdonald, Harald Weinfurter, Hans Kuiper, Edoardo Charbon, and Rupert Ursin. Cubesat quantum communications mission. *EPJ Quantum Technology*, 4(1):6, 2017

1.7.2 Conference Papers

1. Emma Kerr, Malcolm Macdonald, and Philipp Voigt. Taxonomy and Analysis of Issues Facing Post Mission Disposal Concept. In *68th International Astronautical Congress*, Adelaide, Australia, 2017

2. Emma Kerr and Malcolm Macdonald. General Perturbations Method for Orbit Lifetime Analysis Incorporating Non-Spherically-Symmetrical Atmospheres. In *AIAA/AAS Astrodynamics Specialist Conference*, Long Beach, CA, USA, 2016. American Institute of Aeronautics and Astronautics

3. Emma Kerr and Malcolm Macdonald. Improving the Accuracy of Orbit Lifetime Analysis using Enhanced General Perturbation Methods. In *26th AAS/AIAA Space Flight Mechanics Meeting*, Napa, CA, USA, 2016
4. Ciara McGrath, Emma Kerr, and Malcolm Macdonald. An analytical low-cost deployment strategy for satellite constellations. 2015
5. Emma Kerr and Malcolm Macdonald. Improving the Accuracy of General Perturbations Methods for Spacecraft Lifetime Analysis. In *66th International Astronautical Congress*, Jerusalem, Isreal, 2015
6. Emma Kerr and Malcolm Macdonald. A General Perturbations Method For Spacecraft Lifetime Analysis. In *25th AAS/AIAA Space Flight Mechanics Meeting*, Wiliamsburg, VA, USA, 2015

Chapter 2

General Perturbations Orbit Lifetime Analysis Method

The models which will be developed in Chapter 3 and 4 can be applied to any propagation technique; special perturbations, or general perturbations. Due to the analytical nature of the models they are of most benefit to general perturbations methods. Therefore, for demonstration purposes the King-Hele method for orbit lifetime analysis, discussed in Section 1.4, will be modified to include the new models developed. The King-Hele method was derived before modern mathematical toolsets were available, therefore before any modifications are added the method is re-derived to check its correctness and remove some of the simplifications made, such as removing higher order terms.

2.1 Orbit Geometry

To understand the orbit propagation method it is first essential to consider the construction of the orbit itself. The area of interest, in the context of the propagation of objects in planetary orbit, are elliptical Keplerian orbits. The basic construction of an elliptical orbit can be seen in Figure 2.1. In Figure 2.1 a central body would exist at point C, one of the focal points of the ellipse. The solid red line represents the path an object in orbit around that central body would follow.

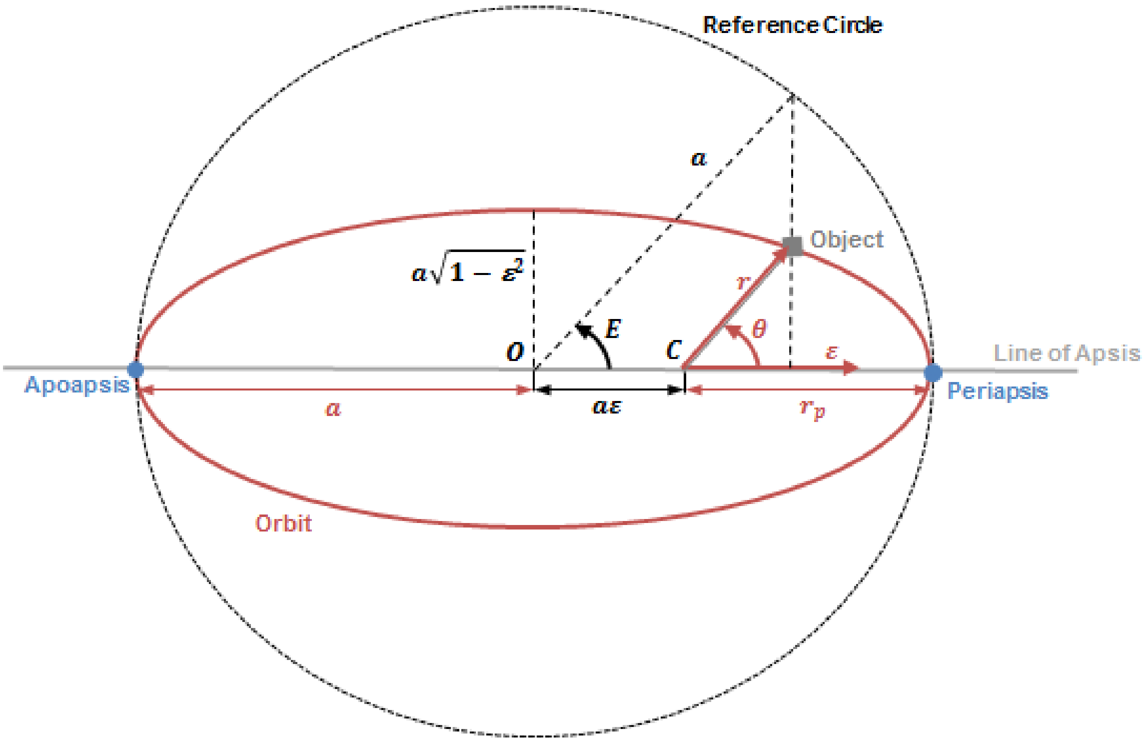

Fig. 2.1 Orbit Geometry

Any Keplerian orbit can be described by five key parameters known as the classical orbital elements or Keplerian elements. A sixth element is used to describe the position of an object in the orbit. These six elements are:

- Semi-Major Axis (a)
- Eccentricity (ε)
- Inclination (i)
- Right Ascension of the Ascending Node (Ω)
- Argument of Periapsis (ω)
- True Anomaly (θ)

The semi-major axis and eccentricity define the size and shape of the orbit, as can be seen in Figure 2.1. The inclination, right ascension of the ascending node and argument of periapsis define the orientation of plane with respect to a reference frame, as can be seen in Figure 2.2. Finally, the true anomaly is used to determine the position of an object along the orbit, with respect to the point of closest approach to the central body, known as periapsis. The opposite point on an orbit to periapsis, the point of furthest approach, is termed apoapsis.

The periapsis and apoapsis of an object specifically in Earth orbit are known as perigee and apogee respectively. Figures 2.1 and 2.2 also show the position vector of an object in orbit, r, radius of periapsis, r_p, and Eccentric anomaly, E.

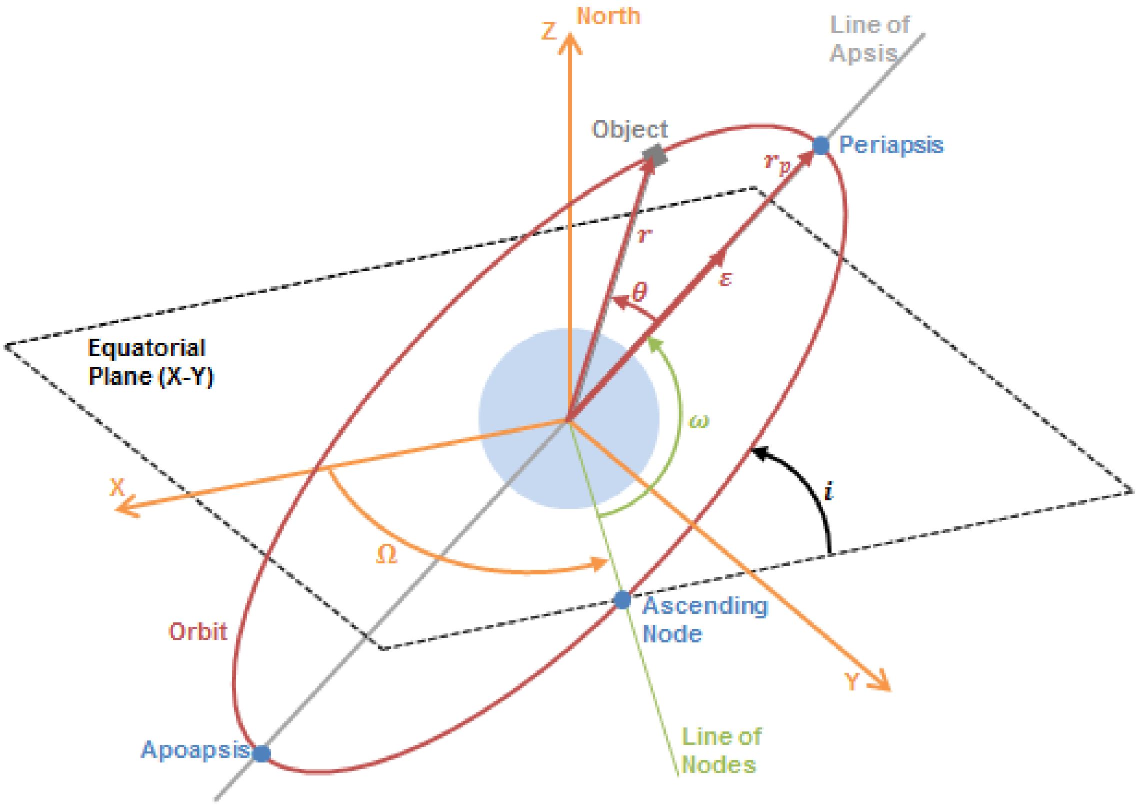

Fig. 2.2 3D Orbit Geometry

2.2 Derivation of Orbit Lifetime Equations

The most significant perturbation affecting a body in a low altitude orbit, about a central body with an atmosphere, is atmospheric drag. Therefore, the drag force must be calculated. This is done using the standard drag equation[19],

$$D = -\frac{1}{2}\rho v^2 F S C_D, \tag{2.1}$$

where ρ is atmospheric density, v is the velocity of the body, C_D is the coefficient of drag of the body, S is the projected area of the body in the instantaneous direction of travel and F is a factor taking into account the rotation of the atmosphere. The rotation factor, F, can be calculated as

$$F = \left(1 - \frac{r\omega_A}{v}\cos(i)\right)^2, \tag{2.2}$$

where r is the orbit radius, ω_A is the rotational velocity of the atmosphere, and i is the inclination of the orbit. The component of acceleration due to drag in the instantaneous direction of travel, termed the tangential component, f_T, is then found by letting

$$\delta = \frac{FSC_D}{m}, \tag{2.3}$$

where m is the mass of the body, such that

$$f_T = -\frac{1}{2}\rho v^2 \delta. \tag{2.4}$$

The component of acceleration due to lift is generally considered to be negligible[23]; it is therefore disregarded for the purposes of this work. The contraction or decay of an orbit, subject to atmospheric drag, over time can be largely characterised by the changes in two of the Keplerian elements: the decrease in the semi-major axis and the decrease in the eccentricity.[23] These can be found from first principles or directly from the Lagrange planetary equations of motion, which describe the rate of change of the classical orbital elements with respect to time.[19] The derivation of Lagrange equations is commonly found in literature.[19,20,60,61] The relevant Lagrange equations in Gaussian form are:

$$\frac{da}{dt} = \frac{2\sqrt{a^3}}{\sqrt{\mu(1-\varepsilon^2)}}\left[\varepsilon\sin(\theta)F_R + \frac{a}{r}(1-\varepsilon)F_S\right] \tag{2.5}$$

$$\frac{d\varepsilon}{dt} = \frac{\sqrt{a(1-\varepsilon^2)}}{\sqrt{\mu}}\left[\sin(\theta)F_R + \left(cos(\theta) + \frac{\varepsilon + \cos(\theta)}{1+\varepsilon\cos(\theta)}\right)F_S\right] \tag{2.6}$$

where μ is the standard gravitational parameter of the central body, and F_R and F_S respectively denote the radial and along track components of the disturbing force, in this case atmospheric drag. In order to apply equation 2.4, equations 2.5 and 2.6 must be rotated into the lift/drag frame, giving equations 2.5 and 2.6 in terms of their tangential and normal components.[23] After performing this translation and assuming that lift component is zero, the relevant Lagrange planetary equations can be simplified to

$$\dot{a} = \frac{2a^2v}{\mu}f_T \tag{2.7}$$

and

$$\dot{\varepsilon} = \frac{1}{v}\left[2f_T(\varepsilon + \cos(\theta))\right]. \tag{2.8}$$

Substituting equation 2.4 into, and rearranging equations 2.7 and 2.8, they become

$$\dot{a} = -\frac{\rho a^2 v^3 \delta}{\mu} \tag{2.9}$$

and

$$\dot{\varepsilon} = -\rho v \delta \left(\varepsilon + \cos(\theta)\right). \tag{2.10}$$

It is, however, more convenient geometrically to work in terms of eccentric anomaly. The geometry of an elliptical orbit as shown in Figure 2.1 demonstrates the connection between the eccentric anomaly, E and true anomaly, θ such that

$$r\cos(\theta) = a\left(\cos(E) - \varepsilon\right), \tag{2.11}$$

$$r\sin(\theta) = a\sqrt{1-\varepsilon^2}\sin(E), \tag{2.12}$$

and

$$r = \frac{a\left(1-\varepsilon^2\right)}{1+\varepsilon\cos(\theta)}. \tag{2.13}$$

Rearranging equation 2.11 to the form

$$\cos(E) = \frac{a\varepsilon + r\cos(\theta)}{a}, \tag{2.14}$$

then substituting in equation 2.13, equation 2.14 becomes

$$\cos(E) = \frac{\varepsilon + \cos(\theta)}{1+\varepsilon\cos(\theta)}. \tag{2.15}$$

by combining equations 2.13 and 2.15 and rearranging, the following relationship is found

$$\varepsilon + \cos(\theta) = \frac{a}{r}\left(1-\varepsilon^2\right)\cos(E). \tag{2.16}$$

This relationship can then be used to transform equation 2.10 so that it becomes

$$\dot{\varepsilon} = -\rho v \delta \left[\frac{a}{r}\left(1-\varepsilon^2\right)\cos(E)\right]. \tag{2.17}$$

Then following the King-Hele derivation method[23], an integration with respect to eccentric anomaly is performed, such that

$$\frac{\mathrm{d}\varepsilon}{\mathrm{d}E} = \frac{\mathrm{d}\varepsilon}{\mathrm{d}t} \Big/ \frac{\mathrm{d}E}{\mathrm{d}t}. \tag{2.18}$$

The variation of eccentric anomaly with respect to time, $\mathrm{d}E/\mathrm{d}t$, is derived by starting with equation 2.13 and substituting in equation 2.11 such that

$$r = \frac{a\left(1-\varepsilon^2\right)}{1+\varepsilon\left(\frac{a}{r}\left(\cos(E)-\varepsilon\right)\right)}. \tag{2.19}$$

Simplifying equation 2.19 gives

$$r = a\left(1-\varepsilon\cos(E)\right), \tag{2.20}$$

and letting

$$p = a(1-\varepsilon^2), \tag{2.21}$$

equation 2.13 can be simplified to

$$r = \frac{p}{1+\varepsilon\cos(E)}. \tag{2.22}$$

Differentiating equations 2.20 and 2.22, with respect to time, they become

$$\dot{r} = a\varepsilon\sin(E)\dot{E} \tag{2.23}$$

and

$$\dot{r}\frac{p}{r^2} = \varepsilon\sin(\theta)\dot{\theta}. \tag{2.24}$$

Moving to polar coordinates (r,θ), in order to deal with the differentiation of θ with respect to time, acceleration with respect to time can be represented as

$$\begin{aligned} \ddot{r} &= (\ddot{r}-r\dot{\theta}^2)_r + (r\ddot{\theta}+2\dot{r}\dot{\theta})_v \\ &= (\ddot{r}-r\dot{\theta}^2)_r + \left(\frac{1}{r}\frac{\mathrm{d}}{\mathrm{d}t}(r^2\dot{\theta})\right)_\theta. \end{aligned} \tag{2.25}$$

If the only force acting is radial, then the transverse component must equal zero, thus $(r^2\dot{\theta})$ must be constant. Therefore letting

$$r^2\dot{\theta} = k, \tag{2.26}$$

$\dot{r}$ is found as

$$\begin{aligned} \dot{r} &= -\frac{1}{r^2}\frac{\mathrm{d}r}{\mathrm{d}\theta}\dot{\theta} \\ &= -k\frac{\mathrm{d}r}{\mathrm{d}v}. \end{aligned} \tag{2.27}$$

Differentiating, equation 2.27 becomes

$$\begin{aligned} \ddot{r} &= \frac{\mathrm{d}\theta}{\mathrm{d}t}\frac{\mathrm{d}\dot{r}}{\mathrm{d}\theta} \\ &= -k^2r^2\frac{\mathrm{d}^2r}{\mathrm{d}\theta^2}, \end{aligned} \tag{2.28}$$

and substituting this into equation 2.26, it becomes

$$\ddot{r} = \left(-k^2r^2\frac{\mathrm{d}^2r}{\mathrm{d}\theta^2} - k^2r^3\right)_r . \tag{2.29}$$

Assuming the radial acceleration is equal to the attraction force of μ/r^2 per unit mass, equation 2.29 becomes

$$-k^2\frac{\mathrm{d}^2r}{\mathrm{d}\theta^2} - rk^2 = -\mu. \tag{2.30}$$

Then by rearranging, equation 2.30 becomes

$$\frac{\mathrm{d}^2r}{\mathrm{d}\theta^2} + r = \frac{\mu}{k^2}. \tag{2.31}$$

Since equation 2.31 is an ordinary differential equation it has the general solution:

$$r = \frac{\mu}{k^2}(1 + \varepsilon\cos(\theta)). \tag{2.32}$$

Substituting equation 2.32 into equation 2.22, p is found as

$$p = \frac{h^2}{\mu}, \tag{2.33}$$

thus equation 2.26 becomes

$$\dot{\theta} = \frac{(p\mu)^{\frac{1}{2}}}{r^2}. \tag{2.34}$$

Substituting equation 2.34 into equation 2.24, $\dot{r}$ is found as

$$\dot{r} = \varepsilon\sin(\theta)\left(\frac{\mu}{p}\right)^{\frac{1}{2}}, \tag{2.35}$$

and substituting this into equation 2.23, it becomes

$$a\varepsilon\sin(E)\dot{E} = \varepsilon\sin(\theta)\left(\frac{\mu}{p}\right)^{\frac{1}{2}}. \tag{2.36}$$

Sunstituting in equations 2.12 and 2.21 and rearranging, equation 2.36 becomes

$$\dot{E} = \left(\frac{1}{r}(1-\varepsilon^2)^{\frac{1}{2}}\right)\left(\frac{\mu}{a(1-\varepsilon^2)}\right)^{\frac{1}{2}}. \tag{2.37}$$

Simplifying equation 2.37, it becomes

$$\dot{E} = \frac{1}{r}\left(\frac{\mu}{a}\right)^{\frac{1}{2}}. \tag{2.38}$$

Substituting in equations 2.17 and 2.38, equation 2.18 becomes

$$\frac{\mathrm{d}\varepsilon}{\mathrm{d}E} = -\rho a\delta\left(\frac{a}{r}\right)^{\frac{1}{2}}\left(\frac{rv^2}{\mu}\right)^{\frac{1}{2}}\left(1-\varepsilon^2\right)\cos(E). \tag{2.39}$$

In order to simplify further the rv^2/μ term must first be expressed in terms of eccentric anomaly, using polar coordinates, velocity may be expressed as

$$v = (\dot{r})_r - (r\dot{\theta})_\theta \tag{2.40}$$

and thus v^2 is

$$v^2 = \dot{r} + (-r\dot{\theta})^2. \tag{2.41}$$

Substituting in equations 2.34 and 2.35, equation 2.41 becomes

$$v^2 = \left(\varepsilon\sin(\theta)\left(\frac{\mu}{p}\right)^{\frac{1}{2}}\right)^2 + \left(\frac{(p\mu)^{\frac{1}{2}}}{r}\right)^2, \tag{2.42}$$

thus with some manipulation

$$\frac{rv^2}{\mu} = \frac{r}{\mu}\left[\left(\varepsilon\sin(\theta)\left(\frac{\mu}{p}\right)^{\frac{1}{2}}\right)^2 + \left(\frac{(p\mu)^{\frac{1}{2}}}{r}\right)^2\right]. \tag{2.43}$$

Substituting in equation 2.22, equation 2.43 becomes

$$\frac{rv^2}{\mu} = \frac{r}{\mu}\left[\left(\varepsilon\sin(\theta)\left(\frac{\mu}{p}\right)^{\frac{1}{2}}\right)^2 + \left(\frac{(p\mu)^{\frac{1}{2}}}{\frac{p}{1+\varepsilon\cos(\theta)}}\right)^2\right], \tag{2.44}$$

then by expanding and simplifying this becomes

$$\frac{rv^2}{\mu} = r\left[\frac{\varepsilon^2+1+2\varepsilon\cos(\theta)}{p}\right]. \tag{2.45}$$

Substituting in equation 2.21, and rearranging, equation 2.45 becomes

$$\frac{rv^2}{\mu} = r\left[\frac{2(1+\varepsilon\cos(\theta))}{p} + \frac{\varepsilon^2-1}{a(1-\varepsilon^2)}\right], \tag{2.46}$$

and substituting in equation 2.22 and simplifying this then becomes

$$\frac{rv^2}{\mu} = 1 - \frac{r}{a}. \tag{2.47}$$

Substituting in equation 2.20 and simplifying, equation 2.47 becomes

$$\frac{rv^2}{\mu} = 1 + \varepsilon\cos(E). \tag{2.48}$$

Thus, equation 2.39 becomes

$$\frac{\mathrm{d}\varepsilon}{\mathrm{d}E} = -\rho a\delta\left(\frac{1+\varepsilon\cos(E)}{1-\varepsilon\cos(E)}\right)^{\frac{1}{2}}\left(1-\varepsilon^2\right)\cos(E). \tag{2.49}$$

Through a similar process equation 2.9 may be manipulated and $\mathrm{d}a/\mathrm{d}E$ can be found as

$$\frac{\mathrm{d}a}{\mathrm{d}E} = -\rho a^2\delta\frac{(1+\varepsilon\cos(E))^{\frac{3}{2}}}{(1-\varepsilon\cos(E))^{\frac{1}{2}}}. \tag{2.50}$$

Letting $x = a\varepsilon$, $\mathrm{d}x/\mathrm{d}E$ is calculated as

$$\frac{\mathrm{d}x}{\mathrm{d}E} = a\frac{\mathrm{d}\varepsilon}{\mathrm{d}E} + \varepsilon\frac{\mathrm{d}a}{\mathrm{d}E}. \tag{2.51}$$

Substituting equations 2.49 and 2.50 in, equation 2.51 becomes

$$\frac{\mathrm{d}x}{\mathrm{d}E} = -\rho a^2\delta\left(\frac{1+\varepsilon\cos(E)}{1-\varepsilon\cos(E)}\right)^{\frac{1}{2}}\left(\cos(E)+\varepsilon\right). \tag{2.52}$$

Equations 2.50 and 2.52 are expanded using a power series expansion. The King-Hele derivation excludes terms of the order ε^3 and higher, herein terms of order ε^4 and higher are excluded thus from this point forward this is the Modified King-Hele method. This expansion gives

$$\begin{aligned}\frac{\mathrm{d}a}{\mathrm{d}E} = -\rho_0\mathbf{e}^{(\beta(a_0-a-x_0))}a^2\delta\Big[1 + 2\varepsilon\cos(E) + \frac{3}{4}\varepsilon^2\left(\cos(2E)+1\right)\\ + \frac{1}{4}\varepsilon^3\left(\cos(3E)+3\cos(E)\right)\Big]\mathbf{e}^{(\beta x\cos(E))}\end{aligned} \tag{2.53}$$

and

$$\begin{aligned}\frac{\mathrm{d}x}{\mathrm{d}E} = -a^2\rho_0\mathbf{e}^{(\beta(a_0-a-x_0))}\delta\Big[\cos(E) + \frac{1}{2}\varepsilon\left(\cos(2E)+3\right)\\ + \frac{1}{8}\varepsilon^2\left(\cos(3E)+11\cos(E)\right) + \frac{1}{16}\varepsilon^3\left(\cos(4E)+8\cos(2E)+7\right)\Big]\mathbf{e}^{(\beta x\cos(E))},\end{aligned} \tag{2.54}$$

where β is the inverse of the density scale height[23] and the subscript 0 denotes initial conditions. Simplifying using the integral form of the Modified Bessel function, $\mathrm{I}_n[arg]$, then integrating equations 2.53 and 2.54 gives

$$\begin{aligned}\Delta a = -\rho_0 \mathbf{e}^{(\beta(a_0 - a - x_0))} a^2 \delta \Bigg[2\pi \Bigg(& \mathrm{I}_0[\beta x] + 2\varepsilon \mathrm{I}_1[\beta x] + \frac{3}{4}\varepsilon^2 \left(\mathrm{I}_2[\beta x] + \mathrm{I}_0[\beta x]\right) \\ & + \frac{1}{4}\varepsilon^3 \left(\mathrm{I}_3[\beta x] + 3\mathrm{I}_1[\beta x]\right) \Bigg) \Bigg]\end{aligned} \tag{2.55}$$

and

$$\begin{aligned}\Delta x = -\rho_0 \mathbf{e}^{(\beta(a_0 - a - x_0))} a^2 \delta \Bigg[2\pi \Bigg(& \mathrm{I}_1[\beta x] + \frac{1}{2}\varepsilon \left(3\mathrm{I}_0[\beta x] + \mathrm{I}_2[\beta x]\right) \\ & + \frac{1}{8}\varepsilon^2 \left(11\mathrm{I}_1[\beta x] + \mathrm{I}_3[\beta x]\right) + \frac{1}{16}\varepsilon^3 \left(7\mathrm{I}_0[\beta x] + 8\mathrm{I}_2[\beta x] + \mathrm{I}_4[\beta x]\right) \Bigg) \Bigg].\end{aligned} \tag{2.56}$$

After simplifying by letting $z = \beta x$ and,

$$y_n = \frac{\mathrm{I}_n[z]}{\mathrm{I}_1[z]} \tag{2.57}$$

and dividing equation 2.55 by equation 2.56, $\mathrm{d}a/\mathrm{d}x$ can be calculated as

$$\frac{\mathrm{d}a}{\mathrm{d}x} = \frac{y_0 + 2\varepsilon + \frac{3}{4}\varepsilon^2 (y_2 + y_0) + \frac{1}{4}\varepsilon^3 (y_3 + 3)}{1 + \frac{1}{2}\varepsilon (3y_0 + y_2) + \frac{1}{8}\varepsilon^2 (11 + y_3) + \frac{1}{16}\varepsilon^3 (7y_0 + 8y_2 + y_4)}. \tag{2.58}$$

Finally, expanding using a power series equation 2.58 becomes

$$\begin{aligned}\frac{\mathrm{d}a}{\mathrm{d}x} = {} & y_0 + \frac{1}{2}\varepsilon \left(4 - 3y_0^2 - y_0 y_2\right) + \frac{1}{8}\varepsilon^2 \left(-29y_0 + 18y_0^3 - 2y_2 + 12y_0^2 y_2 + 2y_0 y_2^2 - y_0 y_3\right) \\ & + \frac{1}{16}\varepsilon^3 \left(-32 + 113y_0^2 - 54y_0^4 + 38y_0 y_2 - 54y_0^3 y_2 + 2y_2^2 - 18y_0^2 y_2^2 - 2y_0 y_2^3 + 6y_0^2 y_3 \right. \\ & \left. + 2y_0 y_2 y_3 - y_0 y_4\right).\end{aligned} \tag{2.59}$$

To move ahead it is convenient to split into various cases according to eccentricity. This split allows specific assumptions to be applied to each case, as appropriate. The cases considered herein are low eccentricity ($\varepsilon < 0.02$) and circular ($\varepsilon = 0$). The choice of $\varepsilon < 0.02$ for the low eccentricity case follows King-Hele's derivation; this assumption is found to be sound as will be seen in the Chapter 3, Section 5.1.2. A further case of ($0.02 < \varepsilon < 0.2$) was also considered, however, the assumptions made were found to be faulty and as such this case is not included here.

2.2.1 Low Eccentricity ($\varepsilon < 0.02$)

Using the expression

$$\frac{T}{T_0} = \left(\frac{a}{a_0}\right)^{\frac{3}{2}}, \tag{2.60}$$

where T is the orbit period, and allowing that for one revolution

$$\Delta t = T_0 \left(\frac{a}{a_0}\right)^{\frac{3}{2}}, \tag{2.61}$$

then dividing equation 2.56 by equation 2.61, $\mathrm{d}x/\mathrm{d}t$ can be calculated as

$$\begin{aligned}\frac{\mathrm{d}x}{\mathrm{d}t} = \frac{-2\pi\delta a_0^2\rho_0}{T_0}\mathbf{e}^{\left(\left(1-\frac{3H}{a_0}\right)\ln\left[\frac{z_0\mathrm{I}_1[z_0]}{z\mathrm{I}_1[z]}\right]+\frac{2H}{a_0}\left(z_0\frac{\mathrm{I}_0[z_0]}{\mathrm{I}_1[z_0]}-z\frac{\mathrm{I}_0[z]}{\mathrm{I}_1[z]}\right)-\frac{x_0}{H}\right)}\Bigg(1 \\ -\frac{H}{a_0}\ln\left[\frac{z_0\mathrm{I}_1[z_0]}{z\mathrm{I}_1[z]}\right]\Bigg)^{\frac{1}{2}}\left(\mathrm{I}_1[z]+\frac{1}{2}\varepsilon\left(3\mathrm{I}_0[z]+\mathrm{I}_2[z]\right)\right),\end{aligned} \tag{2.62}$$

where H is the density scale height. Replacing ε equation 2.62 becomes

$$\begin{aligned}\frac{\mathrm{d}z}{\mathrm{d}t} = \frac{1}{H}\Bigg(\frac{-2\pi\delta a_0^2\rho_0}{T_0}\Bigg(1 \\ -\frac{H}{a_0}\ln\left[\frac{z_0\mathrm{I}_1[z_0]}{z\mathrm{I}_1[z]}\right]\Bigg)^{\frac{1}{2}}\left(\frac{x_0\mathrm{I}_1[z_0]}{Hz\mathrm{I}_1[z]}\right)\mathbf{e}^{\left(-\frac{3H}{a_0}\ln\left[\frac{z_0\mathrm{I}_1[z_0]}{z\mathrm{I}_1[z]}\right]+\frac{2H}{a_0}\left(z_0\frac{\mathrm{I}_0[z_0]}{\mathrm{I}_1[z_0]}-z\frac{\mathrm{I}_0[z]}{\mathrm{I}_1[z]}\right)-z_0\right)}\Bigg(\mathrm{I}_1[z] \\ +\frac{zH}{2a_0}\left(3\mathrm{I}_0[z]+\mathrm{I}_2[z]\right)\Bigg)\Bigg).\end{aligned} \tag{2.63}$$

To simplify equation 2.63 the term B' is introduced as

$$B' = \frac{2\pi}{T_0}\delta\rho_0 x_0\mathrm{I}_1[z_0]\,\mathbf{e}^{(-z_0)}. \tag{2.64}$$

Using B' equation 2.63 simplifies to

$$\begin{aligned}\frac{\mathrm{d}z}{\mathrm{d}t} = -\frac{a_0^2B'}{H^2z}\left(1-\frac{H}{a_0}\ln\left[\frac{z_0\mathrm{I}_1[z_0]}{z\mathrm{I}_1[z]}\right]\right)^{\frac{1}{2}}\Bigg(1 \\ +\frac{zH}{2a_0}\left(3y_0+y_2\right)\Bigg)\mathbf{e}^{\left(-\frac{3H}{a_0}\ln\left[\frac{z_0\mathrm{I}_1[z_0]}{z\mathrm{I}_1[z]}\right]+\frac{2H}{a_0}\left(z_0\frac{\mathrm{I}_0[z_0]}{\mathrm{I}_1[z_0]}-z\frac{\mathrm{I}_0[z]}{\mathrm{I}_1[z]}\right)\right)}.\end{aligned} \tag{2.65}$$

Equation 2.65 can then be simplified by rearranging, expanding and using the recurrence relationship

$$y_2 = y_0 - \frac{2}{z} \tag{2.66}$$

and approximation

$$zy_0 = 2 + \frac{1}{5}z^2. \tag{2.67}$$

as per King-Hele.[23] Equation 2.65 therefore becomes

$$-\frac{a_0^2 B'}{H^2}\frac{\mathrm{d}t}{\mathrm{d}z} = z + \frac{7Hz}{2a_0}\ln\left[z_0 \mathrm{I}_1\left[z_0\right]\right] - \frac{2Hzz_0^2}{5a_0} - \frac{5Hz}{a_0} - \frac{7H}{2a_0}\left(\frac{\mathrm{d}}{\mathrm{d}z}\left[\frac{1}{2}z^2\ln\left[z\mathrm{I}_1\left[z\right]\right]\right]\right) - \frac{7H}{10a_0}z^3. \tag{2.68}$$

By integrating and rearranging equation 2.68 becomes

$$B'\tau = \frac{1}{2}\varepsilon_0^2\left(\left(1 - \frac{z^2}{z_0^2}\right)\left(1 - \frac{H}{a_0}\left(5 + \frac{11z_0^2}{20} - \frac{7z^2}{20}\right)\right) - \frac{7Hz^2}{4a_0z_0^2}\ln\left[\frac{z_0\mathrm{I}_1\left[z_0\right]}{z\mathrm{I}_1\left[z\right]}\right]\right). \tag{2.69}$$

Finally the orbit lifetime can be found by substituting $z = 0$ into equation 2.69; the equation for orbit lifetime is therefore

$$\tau_L = \frac{\varepsilon_0^2}{2B'}\left(1 - \frac{H}{a_0}\left(5 + \frac{11z_0^2}{20}\right)\right). \tag{2.70}$$

2.2.2 Zero Eccentricity ($\varepsilon = 0$)

The case for zero eccentricity is much simpler, as all eccentricity terms can be removed early in the derivation. As $\varepsilon = 0$, equation 2.55 becomes

$$\Delta a = -2\pi\rho_0 a^2 \delta \mathbf{e}^{(\beta(a_0 - a))}. \tag{2.71}$$

Dividing equation 2.61 by equation 2.71, $\mathrm{d}t/\mathrm{d}a$ is calculated as

$$\frac{\mathrm{d}t}{\mathrm{d}a} = \frac{T_0\left(\frac{a}{a_0}\right)^{\frac{3}{2}}}{-2\pi\rho_0 a^2 \delta \mathbf{e}^{(\beta(a_0 - a))}}. \tag{2.72}$$

Integrating, equation 2.72 becomes

$$t_0 - t = \frac{HT_0}{2\pi\rho_0 a_0^2 \delta}\left(\mathbf{e}^{(\beta(a - a_0))} - 1\right) \tag{2.73}$$

and finally substituting in equation 2.60 the lifetime for a spacecraft in circular orbit is

$$\tau_L = \frac{HT_0}{2\pi\rho_0 a_0^2 \delta}\left(1-\mathbf{e}^{\beta a_0\left(\left(\frac{T_f}{T_0}\right)^{\frac{2}{3}}-1\right)}\right). \tag{2.74}$$

The solution found here is identical to that found by King-Hele.[23] This is because the simplifications made in the low eccentricity case when following the King-Hele derivation method were to ignore higher order eccentricity terms, which is necessary in the zero eccentricity case. Due to the approximations made in the derivation of the low eccentricity method, simply substituting in $\varepsilon = 0$ into equation 2.70 does not yield equation 2.74; however the resulting orbit lifetime estimation given by both equations for spacecraft with very low initial eccentricities ($\varepsilon < 0.001$) are comparable as will be seen is Section 5.1.2.

Chapter 3

The Earth's Atmosphere

Calculating atmospheric density at a given altitude is challenging due to the time-variant nature of the atmosphere and the complexity of the interactions affecting it. This chapter will explore atmospheric density modelling and some of the associated challenges.

Atmospheric models can be static profiles, global analytical fits, or time-variant.[20] Time-variant models aim to capture causes of temperature fluctuations in the upper atmosphere. For example, extreme ultraviolet radiation from the Sun causes near-instantaneous heating of the upper atmosphere, and hence rapidly effects atmospheric density.[20] Meanwhile, other causes of atmospheric variation, such as geomagnetic activity, exhibit a cause and effect delay making their effects more difficult to capture.[20]

Many different models of the atmosphere exist and there are many reasons to use any one of them, however none of them are perfect, each having its challenges. To begin to build a model of atmospheric density many assumptions have to be made, such as assuming that the lower atmosphere rotates with the Earth. A more complete list of these assumptions can be found in the survey by Vallado and Finkleman.[22] Furthermore, each atmospheric density model has its own lengthy set of inputs and outputs. Ideally, however, it would be more efficient and user-friendly to have a single standard analytical equation for total atmospheric density based on altitude and solar and geomagnetic activity levels. In order to build such an equation, a data set is required. Therefore, several of the most notable atmospheric density models available are considered for this purpose, these are:

- 1976 Standard Atmosphere
- 1977 Jacchia Reference Atmosphere
- 1990 Mass Spectrometer and Incoherent Scatter Radar Exosphere (MSISE-90)
- 2000 US Naval Research Laboratory Mass Spectrometer and Incoherent Scatter Radar Exosphere (NRLMSISE-00)

- 2007 Global Reference Atmosphere Model (GRAM-07)
- 2008 Jacchia-Bowman Empirical Thermospheric Density Model (JB2008)
- 2009 Drag Temperature Model (DTM)
- 2012 Committee on space research International Reference Atmosphere (CIRA)

It should be noted this list is not exhaustive, however these are the most notable, therefore their main properties were examined to choose the most suitable from among them to move forward with.

The 1976 Standard Atmosphere is a series of idealised steady-state models, which define values for atmospheric temperature, density, pressure and various other properties. The standard atmosphere is defined up to an altitude of 1000 km.[62]

The Jacchia Reference Atmosphere is an atmospheric model that defines atmospheric temperatures, densities, pressures and other properties at altitudes from 90 km up to 2500 km. The Jacchia model includes latitudinal, seasonal, geomagnetic and solar effects. The model was first released in 1970 and updates were released in 1971 and 1977. The Jacchia models are based largely on satellite drag data.[63]

The MSISE-90 model is an empirical model, which was released in 1990 and is defined for altitudes up to 700 km. MSISE-90 defines atmospheric temperature and densities based on the earlier MSIS-86 and data gathered from sounding rockets and space shuttle flights. New incoherent scatter results were also included to improve accuracy.[64]

The NRLMSISE-00 model is an empirical model which was released in 2000 based on the earlier MSIS-86 and MSISE-90 models. NRLMSISE-00 is defined up to 1000 km. Extensive satellite drag data gathered from on-board accelerometers is used to improve accuracy. The model requires many inputs including the time and date, geodetic altitude and latitude, longitude, solar flux data, magnetic flux data and local apparent solar time.[65,66]

The GRAM-07 model was released in 2007 and is defined for all altitudes. GRAM-07 incorporates the MET-2007, Jacchia-Bowman 2006, and NRLMSISE-00 models to provide both mean values and perturbations of atmospheric density, temperature, and pressure.[67,68]

The JB2008 model is an empirical thermospheric density model, released in 2008 based on the earlier JB2006 model. The model includes data on solar and geomagnetic activity and is validated through comparisons with accurate drag data from missions operating in the altitude range 175-1000 km. Accelerometer data from the CHAMP and GRACE missions is also incorporated to validate the geomagnetic storm equations.[69,70]

The DTM model is a semi-empirical model which gives details on the temperature, density and composition of the Earth's atmosphere. DTM incorporates high accuracy and high resolution density data inferred from accelerometers onboard the CHAMP and GRACE missions.[71]

The CIRA model was released in 2012 and is valid for altitudes above 120 km. It incorporates many of the most notable atmosphere models in current literature; including, but not limited to, NRLMSISE-00, JB2008, GRAM-07 and DTM.[72] The CIRA model allows a user to choose between data sets, and provides analysis to show which is the best data set for specific applications.

Of the considered models the NRLMSISE and CIRA models were found to provide the most useful output format: total atmospheric density data with reference to altitude and solar activity. The CIRA model is the more recent of the two, containing NRLMSISE as well as more recent information and empirical data, it is therefore considered to provide the best estimate of the total atmospheric density profile of the Earth's atmosphere. As future models become available they could also be incorporated or considered instead of the CIRA model to improve the density curve fit. In this chapter two analytical atmospheric density models are derived; firstly, a spherically-symmetrical model then, a non-spherically-symmetrical model. The CIRA data is used to derive the spherically-symmetrical model, however unfortunately as it does not contain the appropriate information needed to derive the non-spherically-symmetrical model, therefore NRLMSISE data is used to derive the non-spherically-symmetrical model. A comparison of predictions made using each is provided.

In the first section of this chapter, using the total atmospheric density data from CIRA, an analytical equation for the Earth's atmospheric density is derived using regression analysis. As will be discussed later, the new density index parameter is then applied to capture solar activity effects. The approach taken to develop a global analytical fit for the Earth's atmospheric density negates the need for input parameters such as the local apparent solar time or geodetic latitude and longitude, which are typically required by empirical and time-variant models. However, it does potentially limit the methods applicability to, for example, non-Sun-synchronous orbits where the fixed local apparent solar time, and hence the atmospheric diurnal effects, may not be well-captured. Therefore, in the second section of this chapter a non-spherically-symmetrical model is derived by adding a correction to the spherically-symmetrical model based on the local mean solar time. This correction allows the model to be applied to those special cases where it is necessary to consider the local mean solar time.

3.1 Spherically Symmetrical Atmosphere

Using regression analysis, specifically curve fitting, an equation to describe the CIRA total atmospheric density data can be derived. Traditionally, an exponential curve fit is used to describe atmospheric density data, however such curves are generally only suitable when considering altitudes up to 100 km; when considering higher altitudes they become less accurate.[19] Macdonald et al. proposed a power fit model, however, they did not expand on how accurate it may be in comparison to the exponential fit.[73]

The exponential model connects the altitude to atmospheric density as

$$\rho = \rho_r \mathbf{e}^{\frac{h_r - h}{H}} \tag{3.1}$$

where ρ_r is the atmospheric density taken at a reference altitude usually set at sea level, h_r is the reference altitude and H is the density scale height usually set at 7 km. If the orbit is elliptical, the altitudes are typically taken at periapsis. The difficulty in using this formulation is that it hinges on the use of a reference density and scale height, which are arbitrarily chosen. An expert in atmospheric modelling could arguably use this formulation effectively, however a layman would be unlikely to. Meanwhile, a power model connects the altitude to the atmospheric density as

$$\rho = Ah^B \tag{3.2}$$

where A and B are independent variables derived in the regression analysis.

The exponential model, being the traditional approach, is more often discussed but, as can be seen in Figure 3.1, the power model provides a visibly more accurate fit. The coefficients of determination, R^2, of each of the two curves are shown in Figure 3.1, verifying mathematically that the power curve is the better fit. Furthermore, the use of the power curve is recommended as it removes any confusion over which scale height is the correct. The scale height can be a difficult parameter for a layman to understand and use correctly, thus removing it from the equation will allow laymen to use the model with ease.

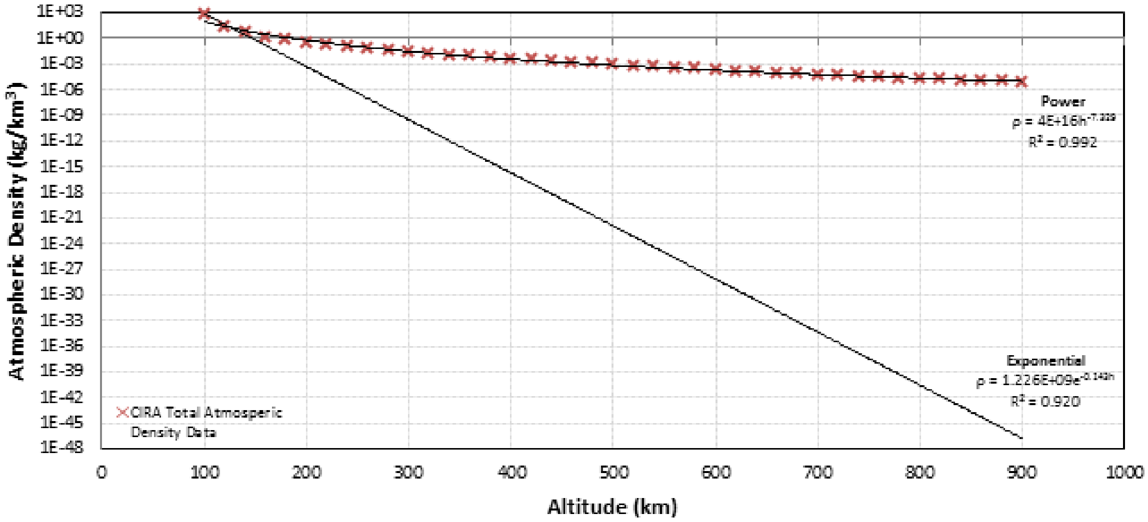

Fig. 3.1 Power and Exponential curve-fit model comparison for average total atmospheric density; with CIRA-12 data also shown as crosses (N.B. logarithmic y-axis)

The curves shown in Figure 3.1 model the average total atmospheric density data. However, the CIRA model provides data for low, average, and high solar activity conditions, corresponding to values of 70, 140, and 250 Solar Flux Units, SFU, respectively.[72] This data is therefore used to generate two further power curves, see Figure 3.2, to describe the total atmospheric density with relation to altitude and solar activity level. The coefficients for equation 3.2 used to produce the curve fits displayed in Figure 3.2 are shown in Table A.1 in Appendix A.

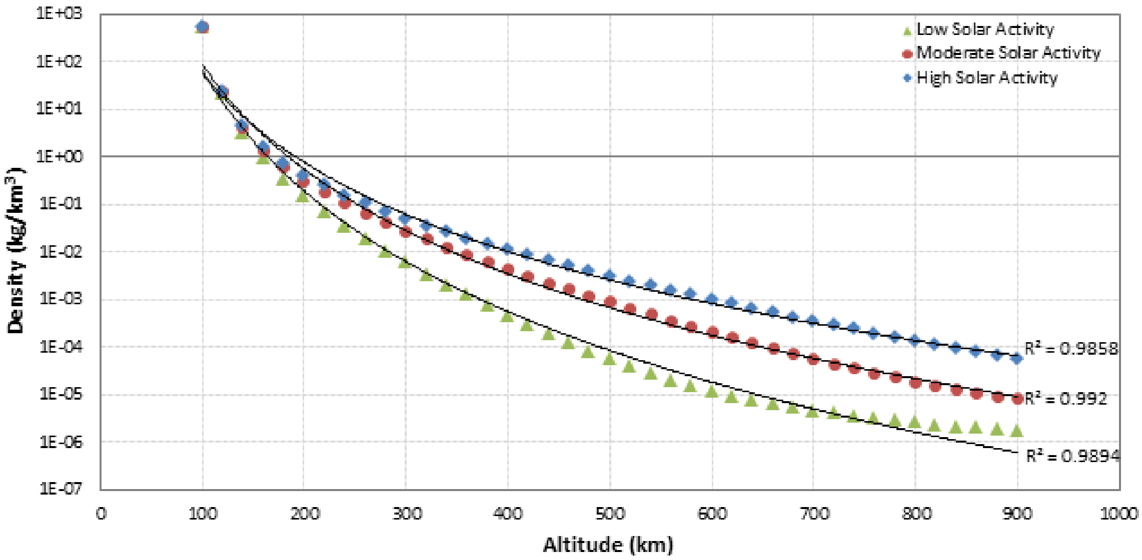

Fig. 3.2 Power curve-fit for atmospheric density at low, average, and high solar activity levels; with CIRA-12 data also shown by markers (N.B. logarithmic y-axis)

It can be seen in Figure 3.2 that the density at any solar activity level is not as accurately described for all altitudes, by one complete curve, as may be desired. Therefore a series of curves is derived by separating the CIRA density data into subsets of 100 km altitude ranges to better fit the data. These series are produced for each of the three solar activity level data sets; the results are shown in Figure 3.3. The coefficients for equation 3.2 used to produce the curve fits displayed in Figure 3.3 are shown in Table A.2 in Appendix A. A full series of graphs showing more detail on the individual curve fits shown in Figure 3.3 can be found in Appendix B.

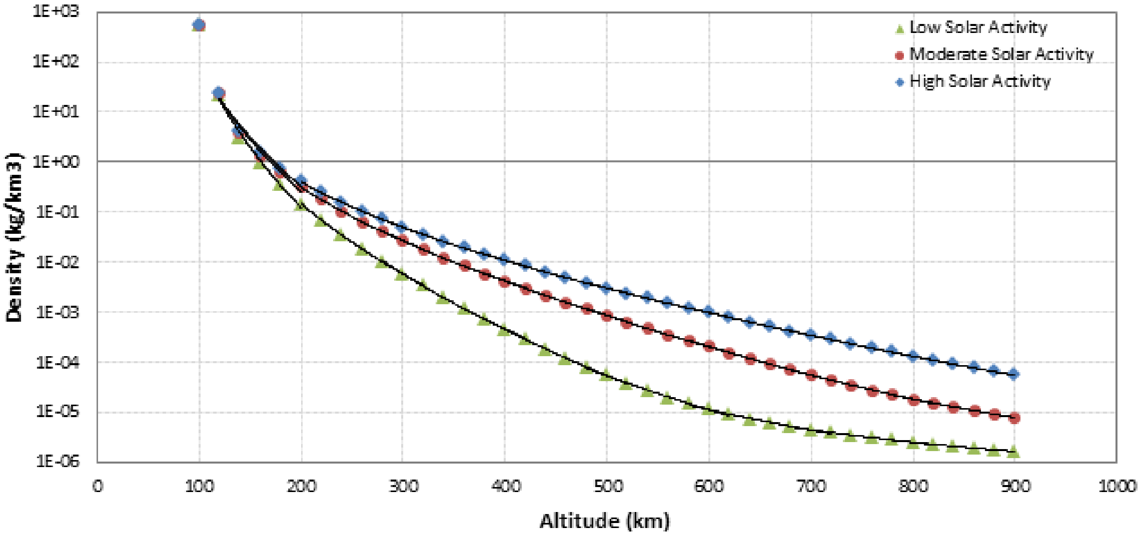

Fig. 3.3 Segmented power curve-fit for atmospheric density at low, average, and high solar activity levels; with CIRA-12 data also shown by markers (N.B. logarithmic y-axis)

This approach produces a more accurate fit over the entire data set however it can be seen that the transition between curves at lower altitudes is problematic. To solve this problem the curves fit to the 100-200 km and 200-300 km data subsets are extended to find the point of intersection; for this particular data set and curve fit this is at 180 km rather than 200 km. This point is then used as the transition altitude to avoid discontinuities in the model. The improvement in accuracy provided by moving from single to multiple curves is minor when considering the R^2 values. However, as will be seen, this minor improvement translates directly into a larger overall improvement in orbit lifetime predictions.

3.1.1 The Solar Cycle

The solar activity cycle is, on average, a 22-year cycle including two polar reversals. Due to the insensitivity of the indices used to measure solar activity to magnetic polarity, the solar activity cycle can be considered for the purposes of this work as, on average, an 11-year cycle.[2,49] The cycle is only loosely considered 11 years as each cycle is unique; there have been individual cycles recorded as short as 9 years and as long as 14 years.[49] As shown in Table 3.1, the most recent cycles vary between approximately 9.9 and 11.8 years.

Table 3.1 Solar Flux Curve Fit Properties

Cycle No.	ϕ	ψ	υ	ξ	t_0 (Date)	t_0 (Months)	Duration (Years)
18	0.003248	43.63	0.71	70	01-01-1944	0	10.4
19	0.005198	40.14	0.71	70	01-06-1954	125	10.2
20	0.001296	52.58	0.71	70	01-08-1964	247	11.8
21	0.002795	44.89	0.71	70	01-05-1976	388	10.3
22	0.004192	41.66	0.71	70	01-08-1986	511	9.9
23	0.001923	48.35	0.71	70	01-07-1996	630	11.8
24	0.001404	45.73	0.71	70	01-06-2009	785	-

The most widely accepted model of the sun in current literature is the magneto-hydrodynamic dynamo model, specifically the Babcock-Leighton dynamo, shown in Figure 3.4.[74,43,44,46,75] This model provides a reasonable explanation of the mechanism behind the solar activity cycle. However, it does not well explain the variation in amplitude of individual cycles. This uncertainty in cycle-to-cycle amplitude variation means that there is an unavoidable challenge in predicting future cycles.[46,75]

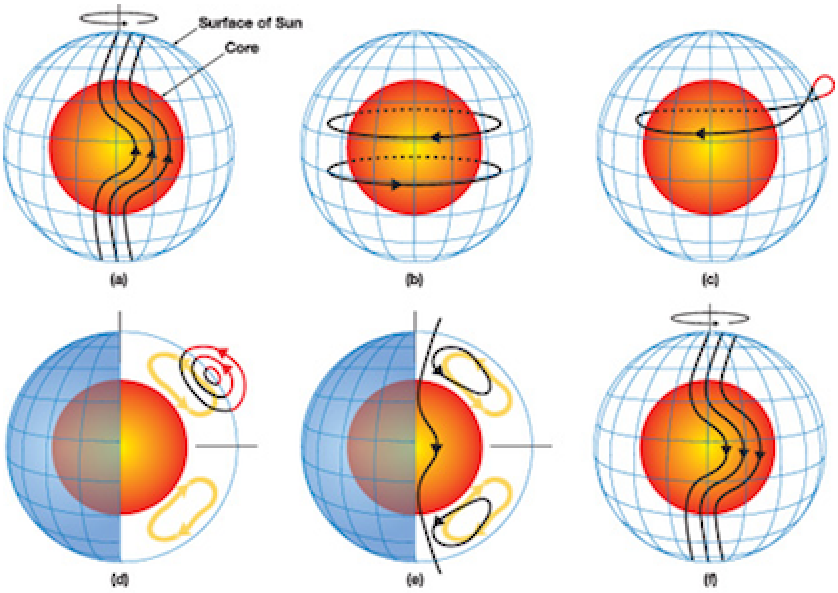

Fig. 3.4 Babcock-Leighton Dynamo Model of the Solar Cycle. Image Credit: University Corporation of Atmospheric Research[1]

The cycle begins with poloidal field, shown in Figure 3.4a. The field experiences shear induced by differential rotation, as the rotation at the equator is around 20% faster than at the poles, this shearing action eventually induces a toroidal field, as shown in Figure 3.4b. New poloidal fields are then set up as the toroidal fields lift and twist releasing the surfacing flux, as shown in Figures 3.4c and 3.4d. These poloidal fields established at the surface then move towards the poles carried by the subsurface meridional circulation where they reverse the poloidal field still present from the beginning of the cycle, as shown in Figure 3.4e. Finally the new poloidal field of opposite polarity is established for the cycle to begin again, as shown in Figure 3.4f. This process takes the first 11 years of the total 22-year cycle; the process is then repeated, over the next 11-year period, in the opposite direction, eventually resetting the entire system. This polarity does not affect the intensity of solar activity experienced at Earth so the cycle is, as discussed previously, usually considered as, on average, an 11-year cycle rather than a 22-year cycle.[75]

The irregular nature of solar activity is often represented using the $F_{10.7}$ index, which measures the solar flux apparent at the 10.7 cm wavelength in Solar Flux Units (1 SFU = $10^{-22}\text{Wm}^2\text{Hz}^{-1}$). Fluctuations caused by solar storms are inherently unpredictable and can cause short term spikes in atmospheric density; generally these spikes average out over time allowing them to be neglected when considering atmospheric density over long time periods. However, depending on the timeframe being considered an uncertainty should be introduced to account for these spikes. The scale of this uncertainty is not well defined in the literature and is therefore up to the user's best judgement. Figure 3.5 shows the daily, monthly-averaged and yearly-averaged solar flux. Approximately three measurements of solar flux are taken per day, a daily average is the average of these three measurements. However, Tapping showed that the noontime measurement could be used as the daily data point with less than 20% error.[76] A monthly average is the average of the daily values for a specific month and a yearly average is the average of the daily values for a specific year. While values for the various parameters may be much more easily read from the yearly trend, it must be remembered that such smoothed data does not demonstrate the true maxima and minima. Rather, such spikes in solar activity due to, say solar storms, are smoothed, giving lower maxima and higher minima. Consequently, when averaging to calculate monthly or yearly data sets as performed herein, further uncertainty is introduced.

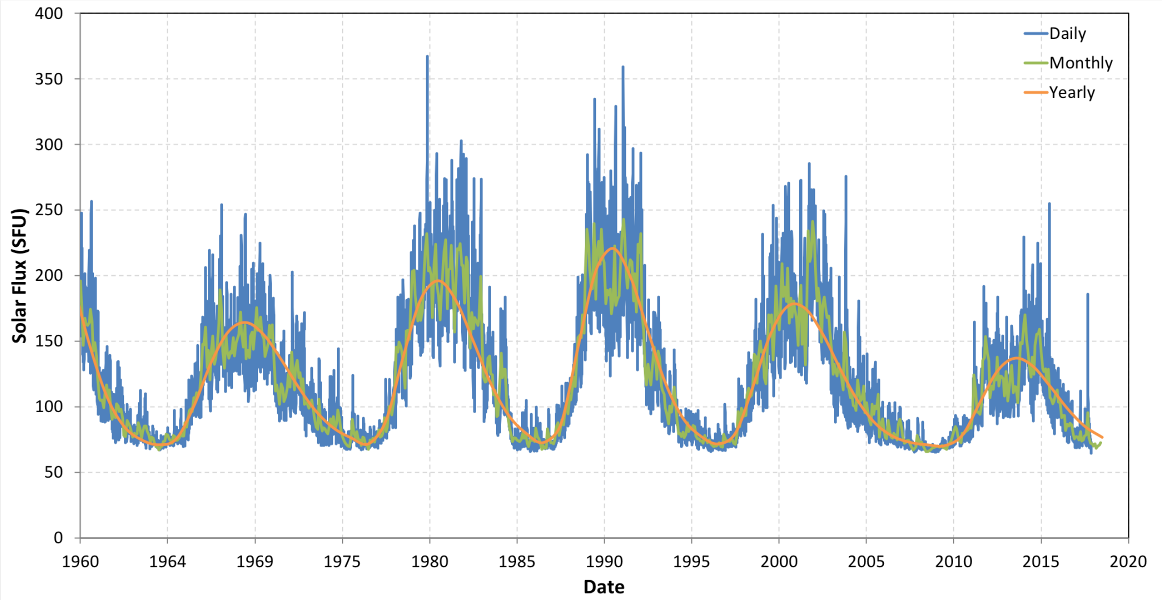

Fig. 3.5 Daily (Blue), Monthly-Averaged (Green) and Yearly-Averaged (Orange) Solar Flux Data, provided at spaceweather.gc.ca[2]

Grand Minima and Maxima

Another feature of the solar activity cycle which should be considered is grand minima and maxima, which are prolonged periods of minimum or maximum activity respectively. The most famous of these was the period from 1645-1715, now known as the Maunder minimum. The period was named after E. Walter Maunder, who was the first to publish, in 1890, on the absence of solar activity during the period.[77–80] The absence was, however, discovered much earlier than these published works, by astronomers of the time who merely noted it as strange. Figure 3.6 shows the yearly averaged sunspot numbers dating back to before the Maunder minimum period. The variability of the amplitude of individual solar cycles can be clearly seen in Figure 3.6.

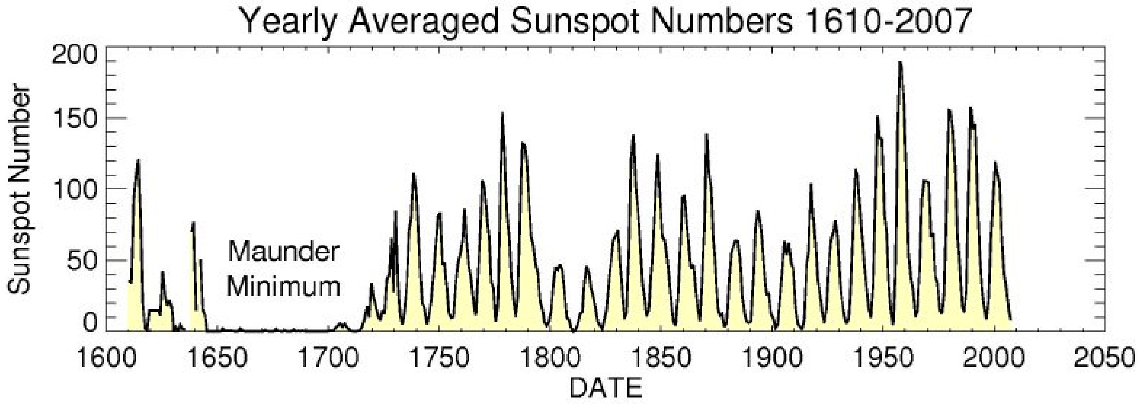

Fig. 3.6 Yearly-Averaged Sunspot Numbers. Image Credit: NASA[3]

There is some discussion as to whether this period actually was a period of minimum activity or just a period when few observations were made or recorded. The argument is sometimes made that an ‘absence of evidence is not evidence of absence’ of activity, however Eddy goes a way to refuting this argument.[81] He concluded that during the period of the Maunder minimum astronomers had the capability and understanding required to keep a record of even small sunspots, therefore the lack of sunspot reports is attributed to the lack of sunspots.

The case is further strengthened by the lack of aurorae reported; aurorae are known to occur more frequently at solar maximum due to the increase in solar material discharged from active regions on the sun’s surface where sunspots also exist. This solar material causes aurorae when it interacts with the Earth’s magnetic field. The more active the region, the more sunspots and the more discharge; this correlation suggests that when few aurorae are seen, few sunspots will be present. Observing aurorae is also sometimes considered preferable to observing sunspots as the identification of active aurorae is much easier to track.[82]

Finally carbon dating, a well-established technique for determining the age of something in archaeology can also be used as a measure of past solar activity. As part of the process carbon dating requires the knowledge of past levels of Carbon-14, ^{14}C; this value is found by analysing the carbon content of a tree of known age ring by ring. Carbon-14, ^{14}C is an isotope constantly produced in the atmosphere by the interaction of galactic cosmic rays, which are in turn dependant on solar activity. The low solar activity at a solar minimum results in an increase in cosmic rays reaching the Earth. Therefore, in turn more than normal ^{14}C is produced during solar minimum periods so more is found in tree-rings formed then.

Taking the variation of ^{14}C levels during the Maunder minimum as a guide it can be seen that there have been two other periods where there was a departure from the nominal solar cycle: a minimum period between 1460 and 1550 and a maximum between 1100 and 1250.

There is some speculation that these minima and maxima could be part of a larger cycle with a period of around 1000 years, and if so that we could be headed towards another maxima in the near future. However, this is pure speculation, as two points alone cannot be used to discern a pattern.

Solar Forecasting

The early demise of Skylab due to unexpectedly high solar activity levels showed the scientific community that accurate solar forecasting is essential to space mission safety and success.[83] Solar forecasting can be completed using many different methods[44], the main groups of which are:

- Even/Odd
- Spectral
- Climatology
- Neural Networks
- Regression
- Precursors

Each method makes certain assumptions about how the solar cycle will vary but essentially they all rely in some way or other on past precedent which, given the limited data available, means they are extremely limited in their accuracy.

The Even/Odd method basically states that the odd numbered cycles generally have greater amplitude than the respective preceding even numbered cycle. This method was later discovered to be somewhat a coincidence rather than a reliable prediction method.[44]

The Spectral method assumes that the main cause of variation in the solar cycle is long-term modulation due to one or more periods. Essentially, spectral methods are a complex form of linear regression. They typically do not perform well, especially when forecasting further than a few months ahead.[44]

Climatology methods are considered fairly inaccurate as they essentially work on the principle that solar activity is unlikely to vary a large amount year to year. These methods rely on consistency in the solar cycle, which, given the chaotic nature of the systems that drive solar activity, is unlikely to produce reliable estimates of solar activity. Climatology is also limited in the length of prediction, being able to predict no more than a year ahead.[44]

Neural Networks or artificial intelligence methods rely heavily on past solar activity to predict future activity, but once again the chaotic nature of the system means that this is not a particularly accurate prediction method.[44]

Regression techniques take past data to extrapolate future solar activity levels. Several techniques are widely used; the McNish-Licoln method, for example, provides the basis for many other regression analysis methods.[84] It predicts the solar activity cycle up to one year in advance using an average cycle constructed by sampling a thirteen-month running mean at twelve month intervals. A more in depth discussion of this method is given by Hathaway, Wilson and Reichmann.[85]

Curve fitting is another method of regression, using equations describing the shape of the cycle to predict solar activity up to the end of the current cycle. This is most effective a few years after a solar minimum. This is also its inherent weakness, it is only truly useful from year 2 to year 9 of a cycle, outside this interval predictions are more estimation than scientific prediction.[85]

Finally, Precursor methods provide the best hope for reliable predictions. They tend to produce consistently better results than other methods. Precursors are observations, other than solar activity, that are used to indicate the magnitude of the next cycle. There are two main types of precursor method: Geomagnetic and Solar. Soviet geophysicists Ohl and Ohl developed precursor methods to make predictions.[86] The strong correlation between the geomagnetic activity at a solar minimum to the amplitude of the next maximum provides the foundation for the Geomagnetic Precursor Method.[44] The most widely used solar precursor is the SODA (SOlar Dynamo Amplitude) index developed by Schatten and Pesnell.[46] It incorporates both the poloidal and toroidal fields of the sun to create an index, which can indicate what happens with the magnetic flux buried beneath the sun's surface. Unfortunately the timing of a cycle predicted by the SODA index has an uncertainty of up to a year. Essentially, the magnitude of the future peak solar flux may be estimated if the current magnetic flux and the position in the cycle are known, however the timing of that peak in flux is more difficult to predict accurately.

Of the prediction methods discussed the SODA index and the various regression techniques are the most viable options for use in solar prediction. While the SODA index could be a useful tool for predicting future solar activity, more research is required to verify that it can produce accurate estimates of the cycle beyond the current one. However, due to the long-term nature of such a verification project, it is currently not a viable option for use in this dissertation. Therefore regression analysis, specifically curve fitting, is found to be the only technique with the maturity and easily malleable nature required for application herein. Curve fitting allows a cycle to be predicted using a known cycle shape, start date and amplitude indicators. The Subsection of Section 3.1.1 titled 'Shape of the Solar Cycle' discusses the shape of a typical solar cycle in more detail, and how this can be used to predict future solar activity as well as to inform density calculations.

Shape of the Solar Cycle

As discussed briefly in the previous section, all solar activity prediction methods have inherent weaknesses. The use of an imprecise solar forecast is, however, still recommended over not including solar activity effects at all.

The solar activity cycle is often over-simplified and represented by a sine function. However, there is an asymmetry to the cycle that the sine function does not properly represent therefore a different form is required. Changes in cycle length (period) and strength (amplitude) mean that data must be sub-divided into individual periods to accurately describe each cycle. The rising and falling portions of each cycle are often of different durations, as can be seen in close examination of Figure 3.7, further complicating the modelling process.

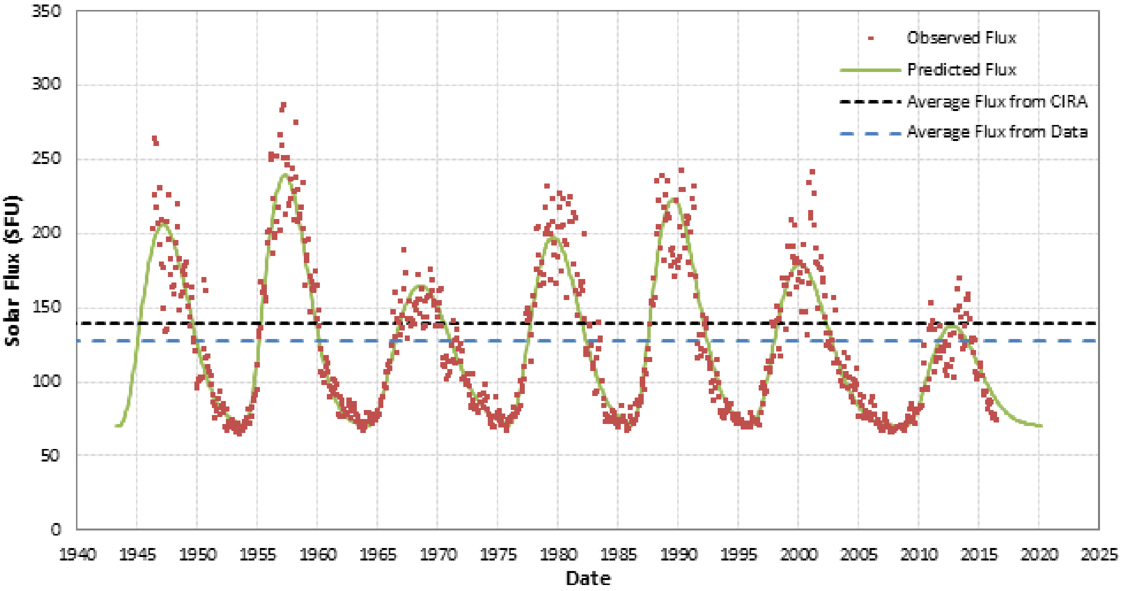

Fig. 3.7 Solar Cycle Data

Several methods utilising regression analysis to predict solar activity have been seen in the past, they are discussed briefly here. Each is based on sunspot number (SSN) data as there is a direct correlation between sunspot number and solar activity. Stewart and Panofsky suggested that the shape of the cycle could be described as

$$SSN(t) = \chi_1(t - t_0)^{\chi_2}\mathbf{e}^{-\chi_3(t-t_0)} \tag{3.3}$$

where t is the time measured from a reference time, and the χ terms are constants derived in the curve fit. Whilst the χ terms and t_0 are constant within each cycle, they vary from cycle to cycle. This method was found to fit some solar cycles relatively well, however others were very poorly represented.[47] Elling and Schwentek proposed another fit, improving accuracy by using 5 parameters instead of 3. They describe the shape of the cycle as

$$SSN(t) = \varphi_4 \frac{\Gamma[(\varphi_2 + \varphi_3)/2]}{\Gamma[\varphi_2/2]\Gamma[\varphi_3/2]} \varphi_2^{\frac{\varphi_2}{2}} \varphi_3^{\frac{\varphi_3}{2}} \frac{(\varphi_1(t + \varphi_5))^{\frac{\varphi_2}{2}-1}}{(\varphi_3 + \varphi_2\varphi_1(t + \varphi_5))^{\frac{\varphi_2+\varphi_3}{2}}} \tag{3.4}$$

where t is the time and $\Gamma[arg]$ is the gamma function and the φ terms are constants derived in the curve fit and are constant within each cycle but vary cycle to cycle. While this method was more accurate, it is not optimal for an engineering application, such as that proposed in this dissertation, due to its complex form and number of variables.[48] However, Hathaway, Wilson, and Reichmann discuss an equation using only 2 independent variables that fits the distribution at least as accurately; both equations typically fit within one standard deviation of the data.[49] Their formulation is

$$SSN(t) = \frac{\alpha\,(t - t_0)^3}{\mathbf{e}^{\frac{(t-t_0)^2}{\gamma^2}} - \kappa}, \tag{3.5}$$

where t is the time (measured relative to a user-selected date) and α, γ, κ, and t_0 whilst constant within each cycle vary from cycle to cycle; α is the amplitude of the cycle, γ is related to the time taken to rise from the initial minimum to maximum, κ provides the asymmetry of the cycle and t_0 is the starting time (in months measured relative to a user-selected date) of the particular cycle being considered. Hathaway et al. found that by setting the starting time for a cycle at the solar minimum κ could be fixed to a constant value of 0.71 for all past cycles for which there was sufficient data. With κ fixed, a relationship between α and γ can be developed. This relationship could be attributed to the Waldmeier effect, which states that larger amplitude cycles take less time to reach their maximum than smaller amplitude cycles.[87] There is, however, an argument that this effect is just a statistical fluke that exists in the Wolf sunspot number data rather than a physical property of the solar cycle.[88] For the purposes of this work this relationship is considered to be a true effect that will exist in future cycles.

There is an inherent correlation between sunspot number and solar activity as previously discussed.[22] This correlation means that the Hathaway et al. formulation can be modified to model solar flux. The major difference between the two data sets is the vertical shift so an independent variable ξ is added to the formulation allowing it to be applied to the solar activity distribution rather than sunspot number distribution. The curve fit constants must then be re-derived using the solar activity data in place of sunspot number data. The solar radio flux, SF, (measured in SFU) is then calculated as

$$SF(t) = \frac{\phi\,(t - t_0)^3}{\mathbf{e}^{\frac{(t-t_0)^2}{\psi^2}} - \upsilon} + \xi, \tag{3.6}$$

where

$$\psi(\phi) = 22.523 + \frac{33.209}{(\phi * 10^3)^{0.385}}. \tag{3.7}$$

With the exception of ξ, parameters are defined as in the Hathaway et al. formulation, ϕ replacing α, ψ replacing γ and υ replacing κ. Equation 3.7 differs from the Hathaway et al. formulation due to the change in the input data set, from sunspot to solar activity data. This new extension of the Hathaway et al. formulation allows a user to bypass the sunspot number and directly calculate the solar activity. It should be noted that, for this and other formulations, the curve fit generated depends on the solar activity data used to generate the curve. Whether the solar activity data is hourly, daily, monthly or yearly averaged will impact the curves parameters; however the formulation itself will remain unchanged. Herein, for ease of processing, monthly averaged solar activity data is used.[2]

Solar cycles 18 through 24 are modelled using equation 3.6, see Figure 3.7. A prediction for solar activity during the remainder of the current cycle, cycle 24, is also shown in Figure 3.7. Details of the start and end dates of each cycle are given in Table 3.1.

A series of values for ϕ, ψ, υ, ξ and t_0 are determined and used to describe each cycle. Note that in the re-derivation υ and ξ were found to vary slightly from cycle to cycle however the curve fit was insensitive to these variations so υ and ξ were set at 0.71 and 70 respectively; meaning only one independent variable, ϕ, is required to model each individual cycle. The values used to generate the curve fit shown in Figure 3.7 are given in Table 3.1.

Density Index

With a model for solar activity in place the atmospheric density is calculated by introducing a new parameter, the density index, which is a measure of the intensity of solar activity. This parameter is introduced to allow interpolation between the solar flux specific atmospheric density curves in Figure 3.2. The density index is described as

$$DI(t) = \frac{SF - SF_{min}}{SF_{max} - SF_{min}} = \frac{SF - 70}{180}, \tag{3.8}$$

where DI is the density index, and SF is the solar radio flux as indicated by the $F_{10.7} index$. Recall that the values for SF_{min} and SF_{max} are taken as 70 and 250 Solar Flux Units, corresponding respectively to low and high solar activity states as given by the CIRA model. The density index is a dimensionless parameter with a value between 0 and 1, this interval is arbitrary. For the purpose of this work values of 0 and 1 are assigned to minimum and maximum solar activity states, corresponding to solar flux values of 70 SFU and 250 SFU respectively. A value of approximately 0.39 would indicate an average solar activity state (solar flux of

140 SFU) due to the unequal nature of the minimum to average, and average to maximum intervals. The density index effectively allows the extrapolation of an infinite number of solar flux specific curves; meaning atmospheric density calculations are unconfined by minimum, average or maximum states of solar activity and can instead be discretised by the suitable solar activity specific curve for the problem.

Directly selecting a density index is problematic due to the implicit nature of the problem; the density index required to describe solar activity for a specific period of time is the average density index calculated over that time period. For example, if the orbit lifetime is 30 days the density index needed is the average density index over those 30 days. Therefore, an iterative method based on the entire time period is used to converge on the averaged density index.

The atmospheric density is calculated by interpolating between minimum and maximum solar conditions using the density index, giving

$$\rho = \rho_l + DI(\rho_h - \rho_l) \tag{3.9}$$

where subscripts l and h indicate low and high solar activity respectively, as defined by the minimum and maximum solar flux values given in the CIRA model.

3.2 Non Spherically Symmetrical Atmosphere

The spherically-symmetrical model, developed in Section 3.1, does not account for the effects of atmospheric oblateness and the diurnal bulge. In order to account for these effects a time-varient data set is required and, unfortunately, the CIRA total density data is not time-variant. Therefore, a new data set is required to build an analytical model for atmospheric density given the local solar time and inclination. In place of the CIRA data, a data set is taken from the NRLMSISE model.[65] The same method of derivation is used to build a new model. The NRLMSISE data was rejected for the spherically-symmetrical atmosphere model as it was shown by Chao et al. that NRLMSISE had large discrepancies from empirical data.[89] However, it is currently the most accurate data available which includes the time-variance required to build the method presented in this section. The method of derivation presented in this chapter could, however, be applied to any data set.

In order to study the influence of atmospheric oblateness and the diurnal bulge they are studied separately. First, however, the spherically-symmetrical analytical model for atmospheric density is re-derived using the NRLMSISE data set in place of the CIRA data. This allows for a fair comparison of the influence of each of the effects against a baseline spherically-symmetrical model. A comparison of the spherically-symmetrical analytical models, derived from the CIRA and NRLMSISE data sets, is also drawn.

As in the previous section, curve fitting is used to find an equation to fit the NRLMSISE data. Also as in the previous section, three solar activity states are taken as the baseline for the model, the density index discussed in Section 3.1.1 can then be used to interpolate between these three states. For the purpose of this section, these three states refer to three specific days on which the atmospheric density is studied, these days are the 1st of January 2008, the 1st of January 2002 and the 1st of January 2015. These dates experienced low, moderate and high solar activity states respectively with mean solar activity levels of 70, 140 and 230 SFU respectively. None of these dates experienced significant solar or geomagnetic storm events as far as historical records detail.

As the model is position and time dependent the latitude, longitude and local mean solar time were averaged out for each date before the curve fitting for the spherically-symmetrical model is carried out. This was done by taking the average of all the data points for time through the day and for all data points through latitude and longitude. This averaging gives the mean atmospheric density for each altitude on each of the three dates studied.

It is found, as with the CIRA data, a power curve fit is the most accurate fit of the data. Therefore, equation 3.2 is again used to build the model. As in the previous section, a set of curve fits using just one equation to fit all the data for each solar activity state is first derived and is shown in Figure 3.8. The coefficients for equation 3.2 used to produce the curve fits displayed in Figure 3.8 are shown in Table C.1 in Appendix C.

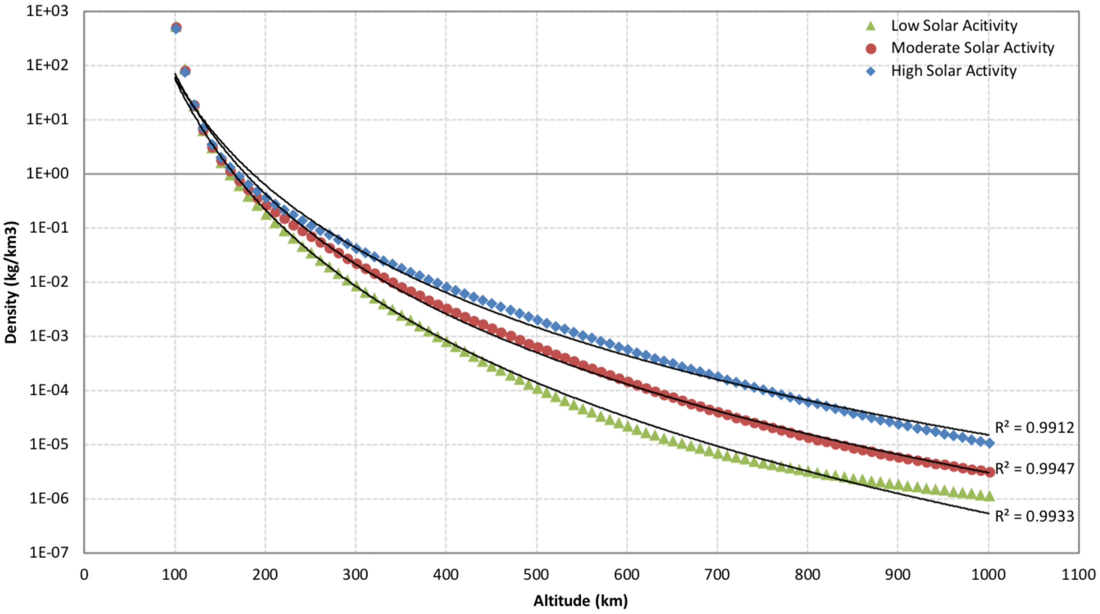

Fig. 3.8 Power curve fit for mean atmospheric density at given solar activity levels using single curves (N.B. logarithmic y-axis)

It is seen in Figure 3.8 that, again, the use of one curve is not sufficient to describe the data over the full range of altitudes. Therefore, the data was broken into small subsets of approximately 100 km each, each set having its own curve fit. Figure 3.9 shows this multi-curve fit. The coefficients for equation 3.2 used to produce the curve fits displayed in Figure 3.9 are shown in Table C.2 in Appendix C.

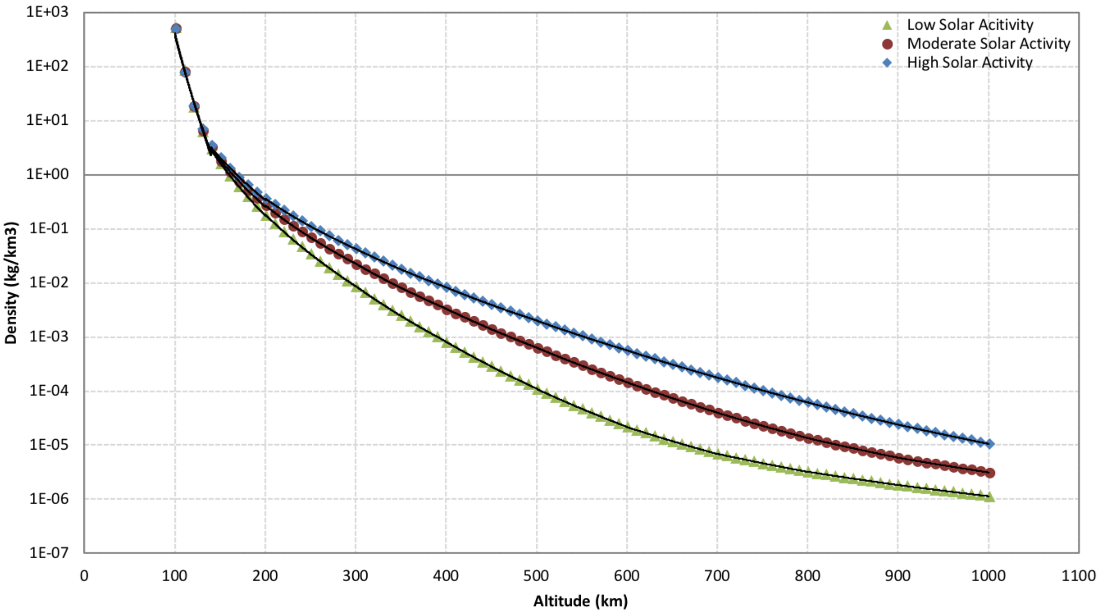

Fig. 3.9 Power curve fit for mean atmospheric density at given solar activity levels using multiple curves (N.B. logarithmic y-axis)

It is seen from Figure 3.9 that, as with the CIRA data, the use of multiple curves to fit the data significantly improves the description of the data. Therefore, the multi-curve fit is used moving forward. However, as in the previous spherically-symmetrical model, the transition between curves at lower altitudes can be problematic. As such the subsets in this region are smaller than those at higher altitudes and the curves are extended to find the points of intersection, which are then used as the transition to avoid discontinuities in the model. In this case, unlike the spherically-symmetrical model derived from the CIRA data, an additional subset was introduced between 100-140 km, to deal with this issue.

3.2.1 Atmospheric Oblateness

Atmospheric oblateness is caused by the Earth's oblateness, the bulge of the Earth around the equator. As a satellite passes over the equatorial bulge the effective altitude of that satellite is less than that of a satellite with the same semi-major axis passing over the North or South

Pole. This differential in true altitude means that the density experienced is greater for the satellite over the equator than the satellite over the Pole.

The data used to study atmospheric oblateness is the data taken from the NRLMSISE model and used to generate the spherically-symmetrical analytical density model discussed in the previous section. However, to study the effects of oblateness the data is averaged over longitude and time to remove the effect of the diurnal variation. This leaves a 3D data set for each solar activity state, for the atmospheric density at a given altitude and latitude. When studied it was found that the effect of oblateness is only evident in the very low altitudes. Figure 3.10 shows the variation caused by atmospheric oblateness for moderate solar activity. This figure has been reproduced for low and high solar activity states, these figures can be seen in Appendix D. It is seen in Figure 3.10 that the effect of atmospheric oblateness is only prevalent below 120 km. Thus, as the orbit lifetime analysis method developed herein is intended for use for much longer lifetimes than would occur at these altitudes, this effect is deemed negligible in terms of this work.

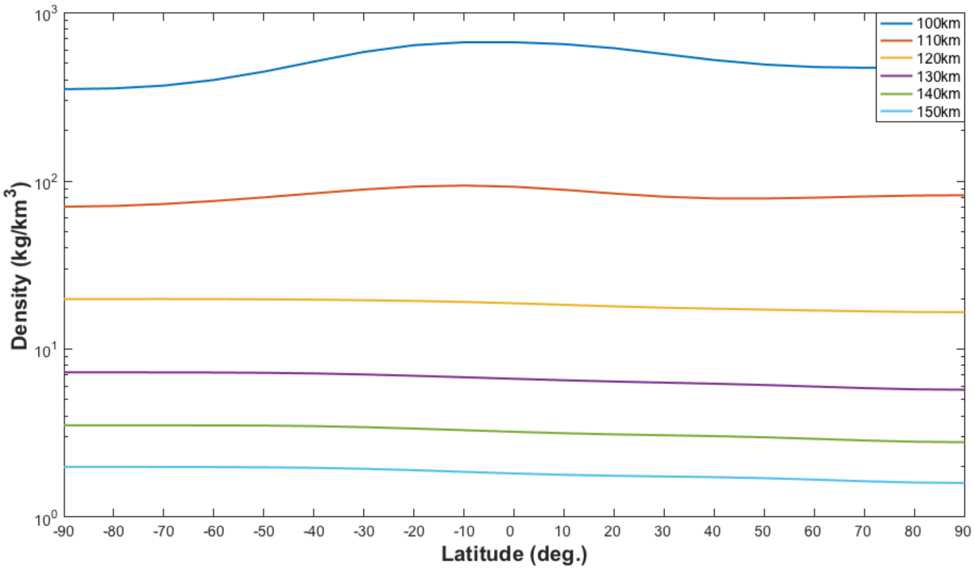

Fig. 3.10 Atmospheric oblateness at moderate solar activity (N.B. logarithmic y-axis)

One interesting result that is seen in Figure 3.10 is that the density in the southern hemisphere is higher than that in the northern hemisphere. This is the result of the dates chosen for this study, as each of the dates is in January, when the position of the Earth is such that the northern hemisphere is tilted away from the sun and the southern hemisphere is tilted towards the sun. This effect could be averaged out by using a larger data set, taken from a full year for example.

3.2.2 Diurnal Variation

The diurnal variation is the bulge in the atmosphere occurring when the sun is overhead. The diurnal variation occurs every day as the Earth rotates, as the sun and Earth move in relation to each other the position of the effect varies, but generally the variation occurs at approximately the same local mean solar time every day. As the sun is overhead the atmosphere directly in line with the sun experiences heating while the atmosphere on the opposite side of the planet experiences cooling, leaving the atmosphere with a pronounced bulge on one side. This effect lags slightly behind the sun, with the maximum density occurring at approximately 2-3 pm local solar time, as can be seen in Figures 3.11 and 3.12.

In order to study the diurnal variation, the NRLMSISE data is averaged over latitude to remove the effect of atmospheric oblateness. This leaves a three dimensional data set for each solar activity state, for the atmospheric density at a given altitude and local mean solar time. For each solar activity condition, the difference from the mean density given by the spherically symmetrical model can be represented by a three dimensional surface, as shown in Figure 3.11. Note, in Figure 3.11 where the difference from mean density is positive the density given by the model including the diurnal variation is greater than that given by the spherically-symmetrical model. A two dimensional contour version is given in Figure 3.12 for clarity.

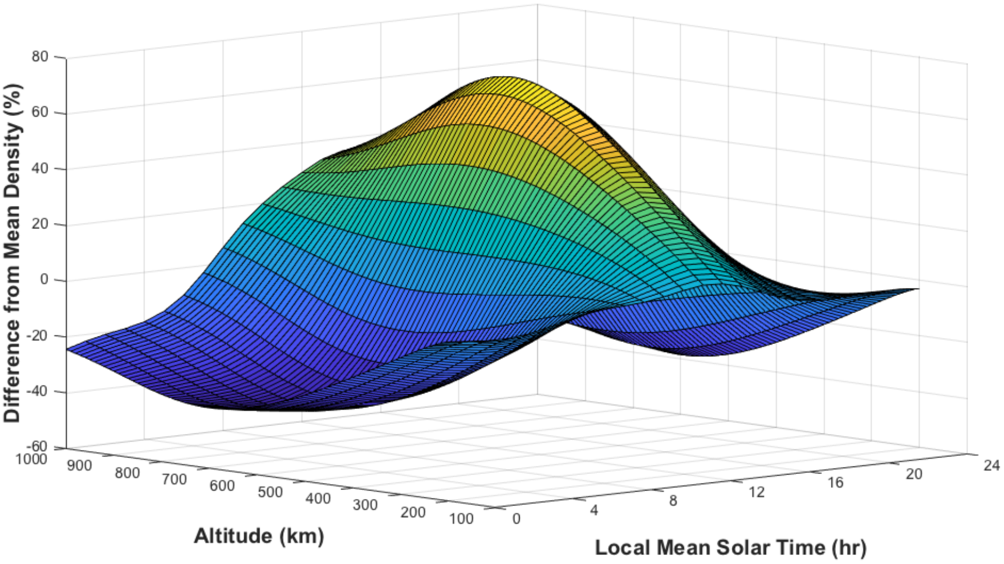

Fig. 3.11 Surface describing density variation at moderate solar activity ($F_{10.7}$ =140 SFU) due to the diurnal variation

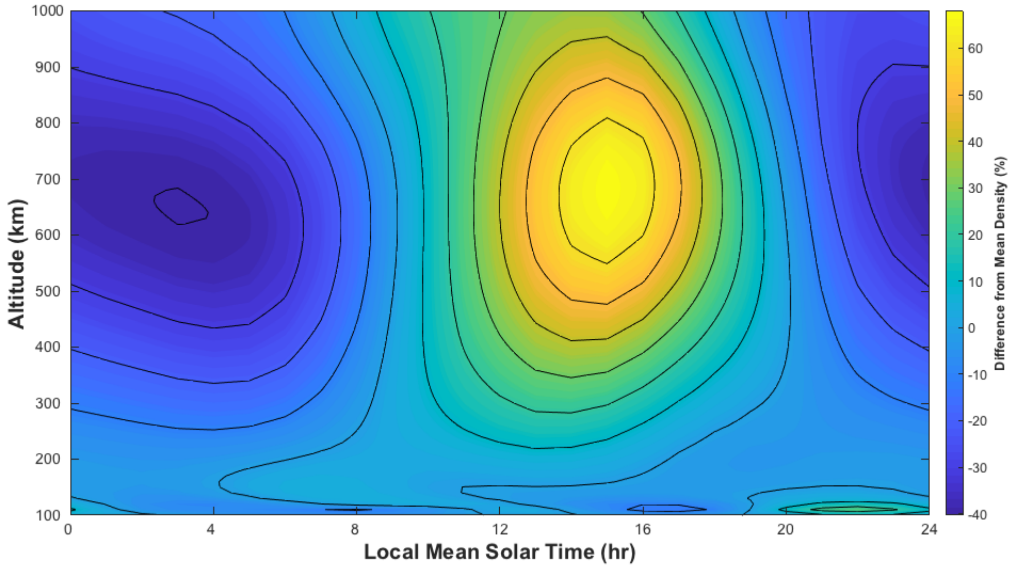

Fig. 3.12 Contours describing density variation at moderate solar activity ($F_{10.7}$ =140 SFU) due to the diurnal variation

As this surface is quite complex to simplify the analysis of the surface can be described by a series of curves for the difference from the mean atmospheric density through a solar day given a specific altitude as can be seen in Figure 3.13.

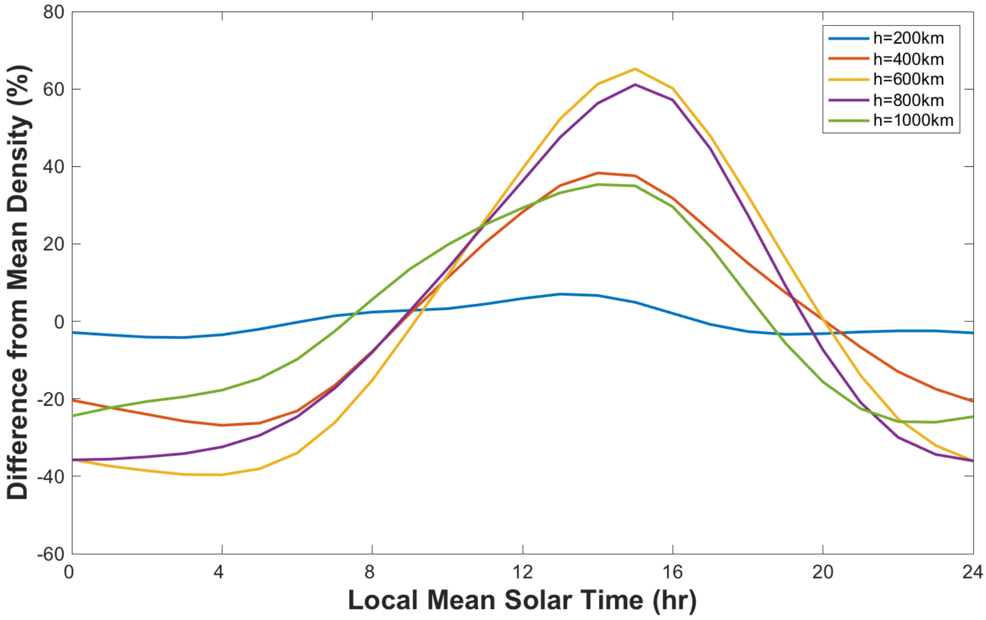

Fig. 3.13 Altitude specific curves describing density variation at moderate solar activity ($F_{10.7}$ =140 SFU) due to the diurnal variation

Each of the discrete curves shown in Figure 3.13 can be described by a single equation of polynomial form. The order of the polynomial is determined by analysing the goodness of fit as determined by the adjusted r-squared value. Table 3.2 shows the mean adjusted r-squared values for all altitude specific curves, for low, moderate and high solar activity states.

Table 3.2 Solar Flux Curve Fit Properties

Polynomial Order	Low Solar Activity	Moderate Solar Activity	High Solar Activity
3	0.790407893	0.813969612	0.816340400
4	0.929429943	0.931703151	0.933561542
5	0.980878380	0.979713625	0.978395272
6	0.989686072	0.989662005	0.991673379
7	0.995163550	0.994913060	0.995408441
8	0.996108640	0.996078730	0.996198301
9	0.997050311	0.997707037	0.998216038

It can be seen in Table 3.2 that from 8th order onward the mean goodness of fit for all solar activity states is greater than 99.5%, and the improvement from 8th to 9th order is less than 0.2%. The 8th order is therefore considered, it is of form

$$\%Diff = P_1 t_s^8 + P_2 t_s^7 + P_3 t_s^6 + P_4 t_s^5 + P_5 t_s^4 + P_6 t_s^3 + P_7 t_s^2 + P_8 t_s + P_9, \tag{3.10}$$

where P_{1-9} are variable coefficients of the curve whose value is dependent on altitude and t_s is the local mean solar time. The relationship between each of these curves can be described by analysing the relationship between the coefficients of the individual altitude curves. It is seen in Figure 3.14 that there is a clear relationship between the coefficients and altitude. Therefore each coefficient can be determined using the equation of the relationship between altitude and coefficient value. These equations were determined using curve fitting.

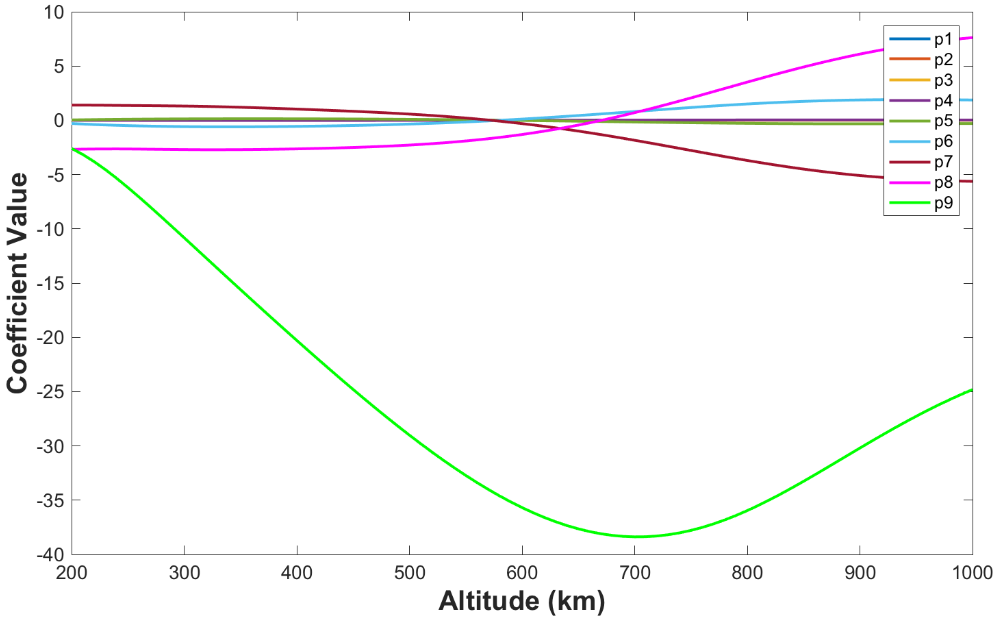

Fig. 3.14 Variation due to altitude of coefficients for altitude specific curves from Figure 3.13

Each coefficient from equation 3.10, shown in Figure 3.14, can be described by another 8th order polynomial of the form

$$P_n = c_1 h^8 + c_2 h^7 + c_3 h^6 + c_4 h^5 + c_5 h^4 + c_6 h^3 + c_7 h^2 + c_8 h + c_9 \tag{3.11}$$

where c_{1-9} are constants derived in the curve fit and h is altitude. A simpler form of equation, for example a smaller order polynomial, could be used in place of equations 3.10 and 3.11 to reduce the number of constants required. However, for the purposes of this work it was decided to use a highly accurate fit and thereby more constants. This process was carried out for each solar activity state and Figures 3.11-3.14 have been reproduced for each state and can be found in Appendix E. A full list of the constants determined and used in this section is shown in Appendix F.

3.2.3 Effect of the Diurnal Variation on Atmospheric Density

In general perturbations methods for orbit lifetime analysis a single density value is used to calculate the orbit lifetime. This density value is typically the total atmospheric density at the orbit periapsis. However, when considering an atmosphere model including the diurnal variation this single value may not be representative of the density over the orbit lifetime. For example, if the density is taken at a local mean solar time of 12 noon, the density will be much greater than if it was taken at 12 midnight. Therefore, it is recommended that when using general perturbations methods the initial density used should be an average taken over the first orbit. The variation of density over an orbit is dependent on the variation in local mean solar time. This variation is not constant but its rate of change can be linked to the inclination. Figure 3.15 demonstrates the relationship between local mean solar time and inclination.

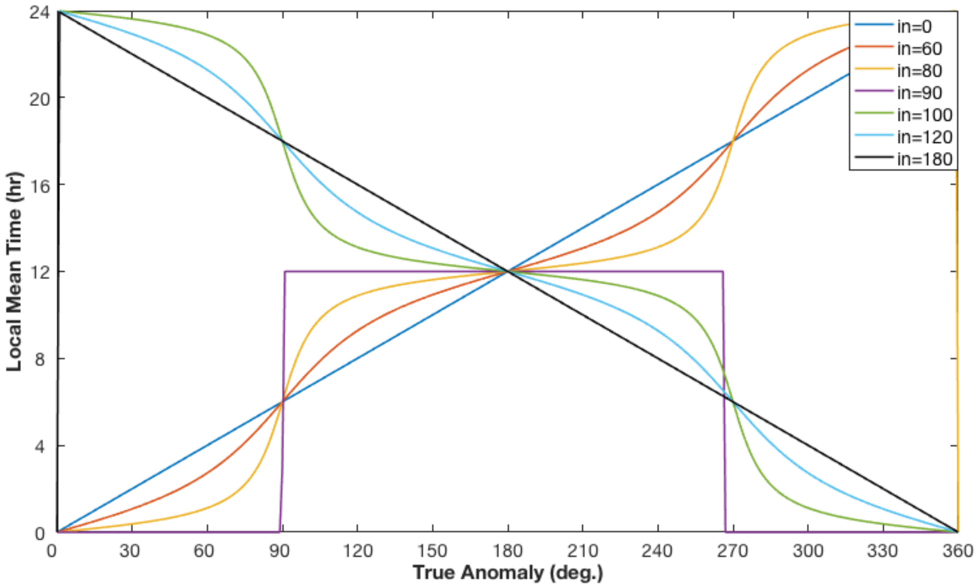

Fig. 3.15 Relationship between inclination and local mean time for a satellite in an orbit of altitude 800 km

It is shown in Figure 3.15 that objects in polar orbits experience an instantaneous shift in solar time between noon and midnight. It should be noted, however, that Figure 3.15 is generated for a particular set of orbits, on a particular date, starting at a particular time. Therefore, this noon-midnight paradigm could be 2am-2pm given a different initial date and time. The pattern visible would remain the same, however it would be shifted in the y-axis. This variation in local solar time can then be mapped to the variation in density, as can be seen in Figure 3.16. Again, it should be noted that Figure 3.16 is accurate only for these particular orbits, date and time. This figure has been reproduced for each solar activity state, these are shown in Appendix G.

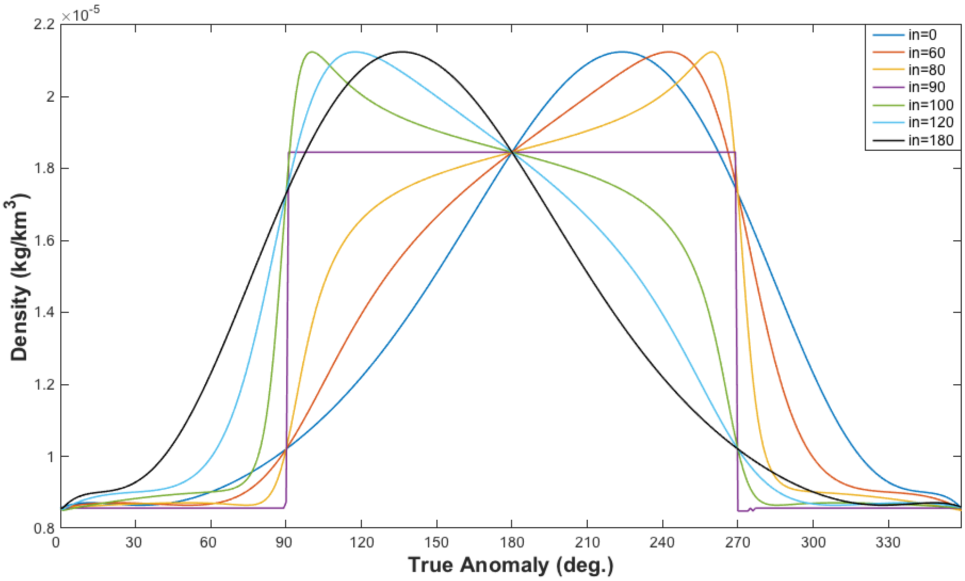

Fig. 3.16 Change in density over 1 orbit revolution due to the diurnal variation for a satellite at 800 km altitude and various inclinations during moderate solar activity ($F_{10.7}$ =140 SFU)

Using the method of averaging for one orbit revolution the difference in the mean density, when using the diurnal model in place of the spherically-symmetrical model, can be calculated. This difference is plotted for various inclinations and orbit altitudes in Figure 3.17.

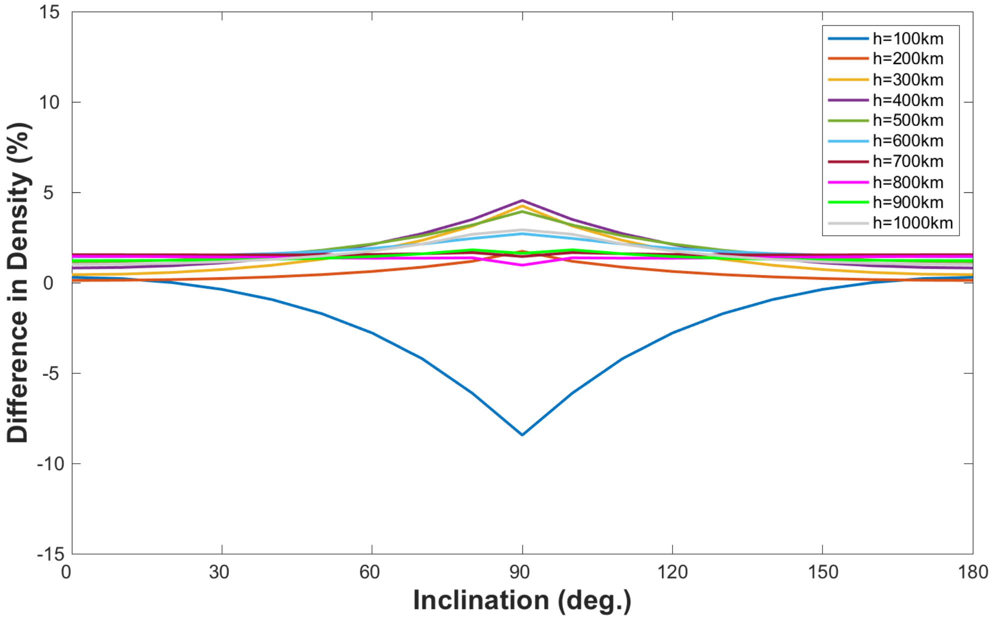

Fig. 3.17 Percentage difference in density when comparing the mean density given by the diurnally varying atmospheric model and the mean density from the spherically-symmetrical atmospheric model for a 12am-12pm orbit during moderate solar activity ($F_{10.7}$ =140 SFU)

Figure 3.17 shows that the peak in density difference occurs for polar orbits where inclination is 90°. This is to be expected as a polar orbit would experience the most extreme variation in density over a single orbit. Figure 3.17 also shows that for the majority of altitudes the spherically-symmetrical atmosphere model is underestimating the density, while at lower altitudes it is overestimating the density. This figure has been reproduced for each solar activity state and is shown in Appendix H. The pattern of over and under-estimating the density is consistent across the solar activity levels, as can be seen in the figures in Appendix H. As with Figure 3.15 and Figure 3.16, it should be noted that Figure 3.17 is only accurate for the particular date and time used to create it. However, it does give an idea of the errors which are carried into the orbit lifetime analysis when the diurnal effect is not considered. It is found that the mean percentage differences in density occur when the satellite is in a noon-midnight or 6am-6pm orbit. The maximum percentage differences in density occur in 9am-9pm and 3am-3pm orbits. For 9am-9pm orbits the spherically-symmetrical atmosphere model underestimates the density for higher altitudes, while for the 3am-3pm orbits the spherically-symmetrical atmosphere model overestimates the density for higher altitudes. Figure 3.18 and Figure 3.19 show the percentage differences in density for the 9am-9pm and 3am-3pm orbits respectively.

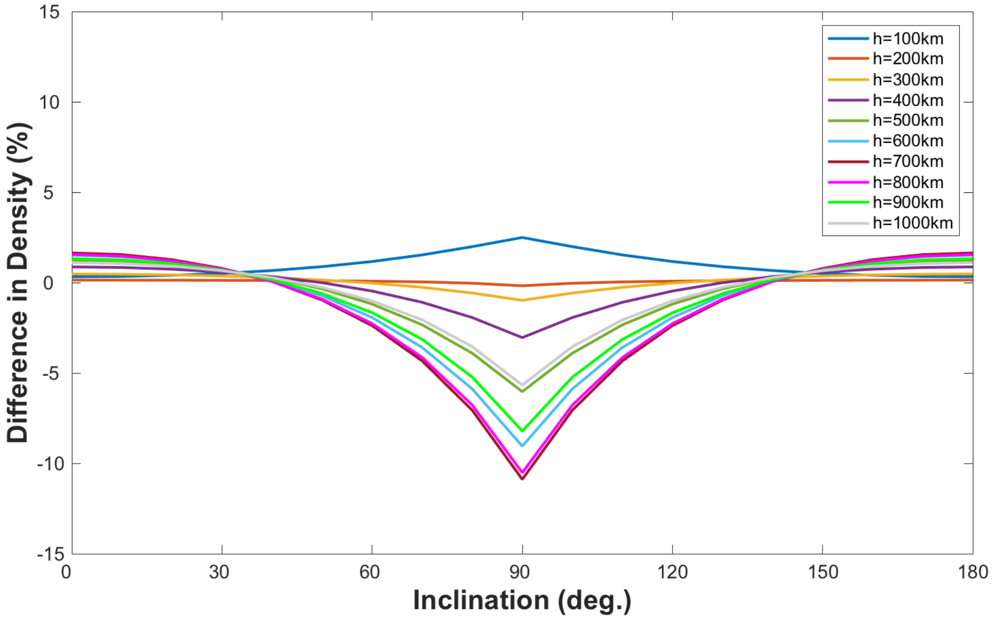

Fig. 3.18 Percentage difference in density when comparing the mean density given by the diurnally varying atmospheric model and the mean density from the spherically-symmetrical atmospheric model for a 9am-9pm orbit during moderate solar activity ($F_{10.7}$ =140 SFU)

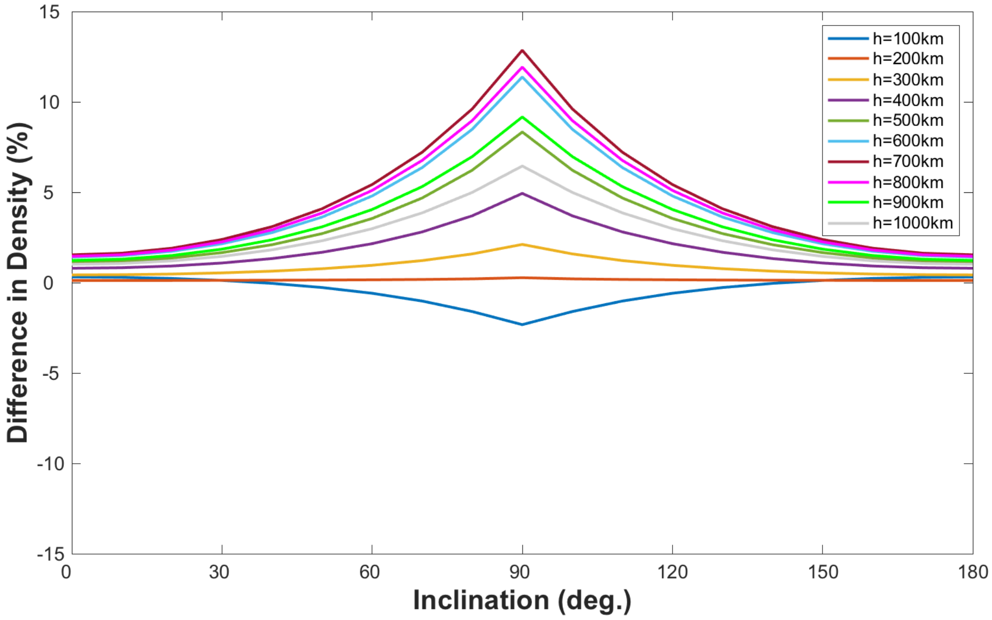

Fig. 3.19 Percentage difference in density when comparing the mean density given by the diurnally varying atmospheric model and the mean density from the spherically-symmetrical atmospheric model for a 3am-3pm orbit during moderate solar activity ($F_{10.7}$ =140 SFU)

The position of the orbit is particularly interesting when considering a sun-synchronous satellite. The right ascension of the ascending node of a sun-synchronous satellite rotates at the same rate as the Earth meaning that it maintains its orbit position relative to the Earth, crossing the equator at the same local mean solar time on each orbit, i.e. if the orbit starts as a noon-midnight orbit it will remain as such until the satellite loses a significant amount of altitude such that its right ascension begins to drift at a different rate to the Earth's surface. Thus, the diurnal effect is expected to have a larger influence on these types of orbits.

As the orbit lifetime of a spacecraft is proportional to the atmospheric density, any error in the density is translated directly into an error in the orbit lifetime analysis. Therefore, the inclusion of the diurnal variation is likely to be important when considering special cases such as sun-synchronous satellites. This will be discussed further in Chapter 5, where a case study is presented to study the effect of including the non-spherically-symmetrical atmosphere in orbit propagation.

Chapter 4

The Ballistic Coefficient

The ballistic coefficient is made up of three of the main input parameters for orbit propagation; mass, projected area and drag coefficient. It is an indicator for how an object is affected by aerodynamic drag; a low ballistic coefficient means an object will be greatly affected, whereas a high ballistic coefficient means the object will be relatively unaffected. Essentially, it measures how streamlined an object is, how efficiently it can travel through a fluid. In terms of spacecraft in orbit, the ballistic coefficient is important when considering the atmospheric drag force in orbit propagation. It determines how quickly a spacecraft's orbit will decay, and in what manner. A spacecraft carrying delicate cargo or humans on board will typically have a low ballistic coefficient, so that it re-enters the lower atmosphere slowing down gradually, reducing the forces experienced on board. Conversely, a ballistic missile launched inter-continentally will typically have a very high ballistic coefficient; meaning it loses very little speed on re-entry, making them very difficult to track or defend against.

The ballistic coefficient typically has the form

$$BC = \frac{m}{SC_D} \tag{4.1}$$

where m is the mass of the object, S is the projected area of the object in the instantaneous direction of travel and C_D is the drag coefficient of the object.

When considering orbit propagation and orbit lifetime analysis, with the exception of space debris, the mass of an object is typically known. However, the drag coefficient and area can vary, sometimes chaotically, in-flight and as such are challenging to determine accurately. This chapter focusses on improving the estimation of the ballistic coefficient for orbit propagation and orbit lifetime analysis. In order to do this, the most logical first step is to examine the terms individually. However, the mass, if unknown, is not a variable that can be estimated without first knowing the values of the other terms, therefore it cannot be considered individually. The drag coefficient cannot be measured; it is a dimensionless term used to measure the resistance of an object to moving through a fluid. It varies with the relative speed of the body to the fluid, and the shape of the body and is therefore very difficult to calculate independently. This leaves the projected area term, this term can be estimated depending on certain factors, such as understanding changes in spacecraft attitude and spacecraft geometry. Therefore, the first section of this chapter will look at ways in which the area term can be estimated. The second section of this chapter will look at estimating the ballistic coefficient from orbit tracking data. While this would negate the need to improve estimation of the individual terms, the use of orbit tracking data means this method is only available for objects already in orbit, meaning it could not be used in any pre-launch capacity, such as mission analysis or space debris mitigation regulatory compliance.

4.1 Estimating the Projected Area

In many cases the area of a spacecraft can be estimated effectively pre-launch, as soon as the geometry is fixed. A spacecraft may be attitude controlled in a specific orientation meaning that the area is fixed, or it may tumble in a controlled or uncontrolled manner in which cases an average area must be calculated for use in general perturbations techniques. An average area may also be required for use in special perturbations techniques if the tumble cannot be accurately modelled and/or if the integration time-step is not sufficiently short enough to deal with the constantly varying area accurately. The average area could also be used in special perturbations techniques for convenience, however this would introduce an unnecessary uncertainty.

Calculating the average area of a tumbling spacecraft can be problematic as many factors can affect the mode of tumble. If the tumble is truly random, however, numerical methods can be used to simulate the average projected area of an object in orbit accurately and can be incorporated easily into special perturbations methods for orbit propagation and orbit lifetime analysis. It should be noted that to incorporate the area calculated during random tumbling into a special perturbations method the time-step must be sufficiently short enough to avoid errors introduced by assuming the area is constant between time-steps. As with the orbit lifetime analysis method, if the solution speed is to be considered, an analytical solution for average project area becomes more useful. Therefore, to accurately simulate a tumbling spacecraft a method of calculating the average projected area of spacecraft during its orbit lifetime is particularly important. To build an analytical expression for the average projected area is impossible as it is dependent on the geometry of the spacecraft, which varies greatly from mission to mission. In special cases such as CubeSats where there are standards of size and geometry building an analytical solution is possible. However, the addition of deployable panels produces more variability in the geometry and poses challenges such as self-shadowing which must be considered.

To calculate the average area of a randomly tumbling spacecraft, the ISO standard 27852 suggests a flat plate model should be used if no other model is available.[17] In the flat plate model the average projected area is calculated as

$$S = \frac{S_1 + S_2 + S_3 + S_4}{2} \tag{4.2}$$

where S_1, S_2 and S_3 are the areas seen in the x, y and z directions and S_4 is the total area of any deployed panels. This method is crude but, as will be shown, is effective for basic cuboid geometry with no deployed panels. However, when considering more complex shapes or deployed panels it introduces significant errors. A correction factor for this solution is proposed in this section to extend this model and make it applicable to CubeSats with deployable panels.

To build this correction factor, it is necessary to start with a numerical solution. Therefore, in order to assess the average projected area of a randomly tumbling spacecraft, it is assumed that the tumble is uniform and every aspect of the spacecraft will be 'seen' equally often throughout the orbit lifetime. A uniform sphere of viewpoints is therefore set up with the spacecraft at the centre and the projected area is calculated from each viewpoint using a method similar to that presented by Ben-Yaacov et al.[50] The average of all of these values is then taken to be the average projected area. This is also the numerical method recommended in ISO standard 27852.[17]

Six different spheres were considered, with an increasing number of viewpoints, in order to find a compromise between computational efficiency and accuracy of the average area calculated. These spheres were constructed using the golden ratio so that viewpoints are equally spaced, as can be seen in Figure 4.1.

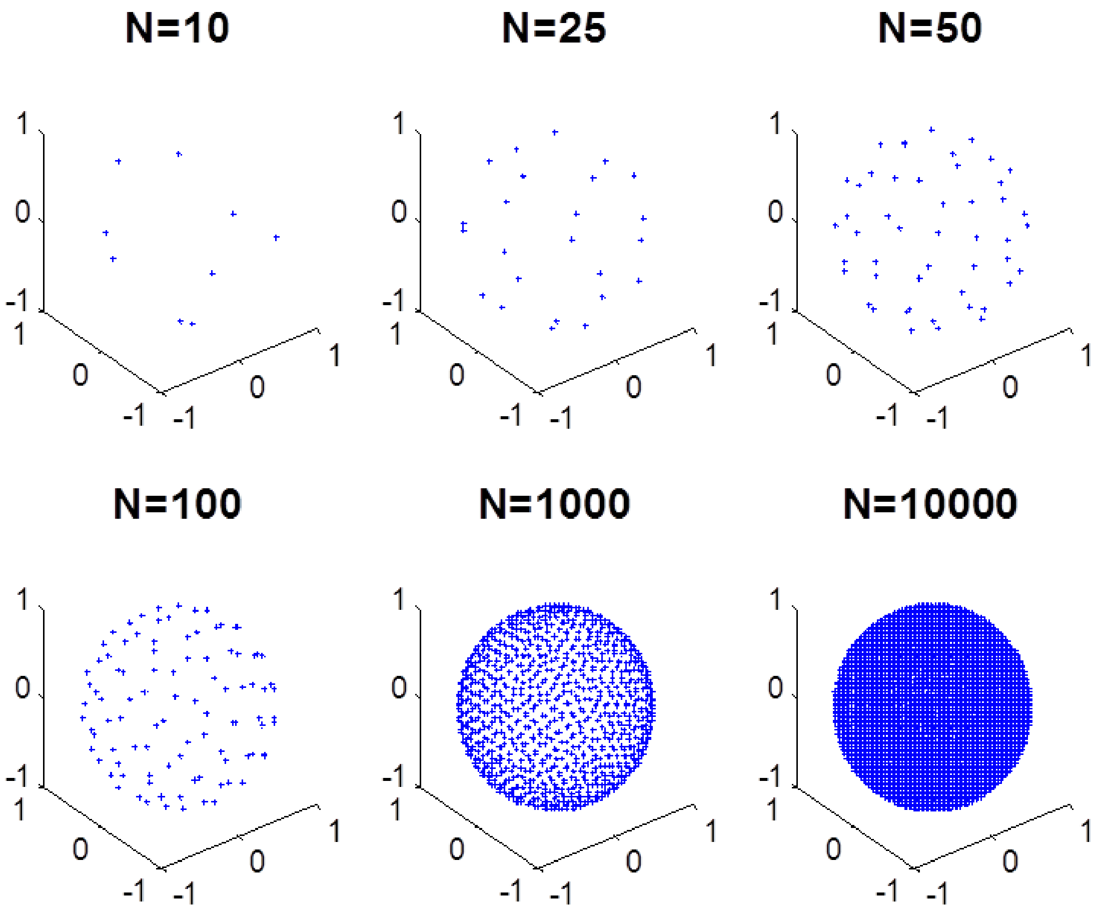

Fig. 4.1 Meshing Options

In order to compare accuracy due to the differing viewpoint spheres, a 3U CubeSat is used as a test case, the minimum area of the 3U is a 10x10 cm face. Besides the basic 3U with no deployable structures, a further 51 scenarios of various deployable panel sizes and positions were considered in this check for accuracy. Eight possible panel positions on the CubeSat are considered as shown in Figure 4.2. The 52 scenarios are created by variously including or excluding these panels.

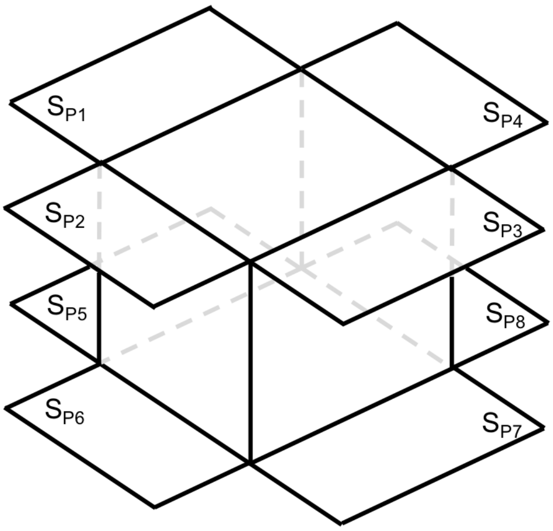

Fig. 4.2 CubeSat Panel Position Options

Table 4.1 shows the accuracy of the various spheres for the initial 52 scenarios considered. Note the average area given in Table 4.1 is the average of all the areas 'seen' from each of the viewpoints.

Table 4.1 Viewpoint Sphere Comparison

N	Minimum Area (m^2)	Average Area (m^2)	Average %Error in Average Area	Standard Deviation of %Error in Area
10	0.025023	0.060498	1.021	0.715
25	0.022211	0.060269	0.398	0.247
50	0.020147	0.060424	0.172	0.148
100	0.016484	0.060334	0.047	0.034
1000	0.012866	0.060327	0.002	0.001
10000	0.010857	0.060327	-	-

From Table 4.1 it is seen that the accuracy in the determining the minimum projected area is greatly improved by increasing the number of viewpoints used. However, it can also be seen that the average projected area is relatively unaffected by the number of viewpoints used. In fact the improvement in accuracy from 10000 down to 10 viewpoints is just over 1%. A comparison of the curve fit generated from this data can be seen in Figure 4.3. It should be noted that along the x-axis, in Figure 4.3, is the ISO standard flat plat model; this allows an easy comparison of the different configurations.

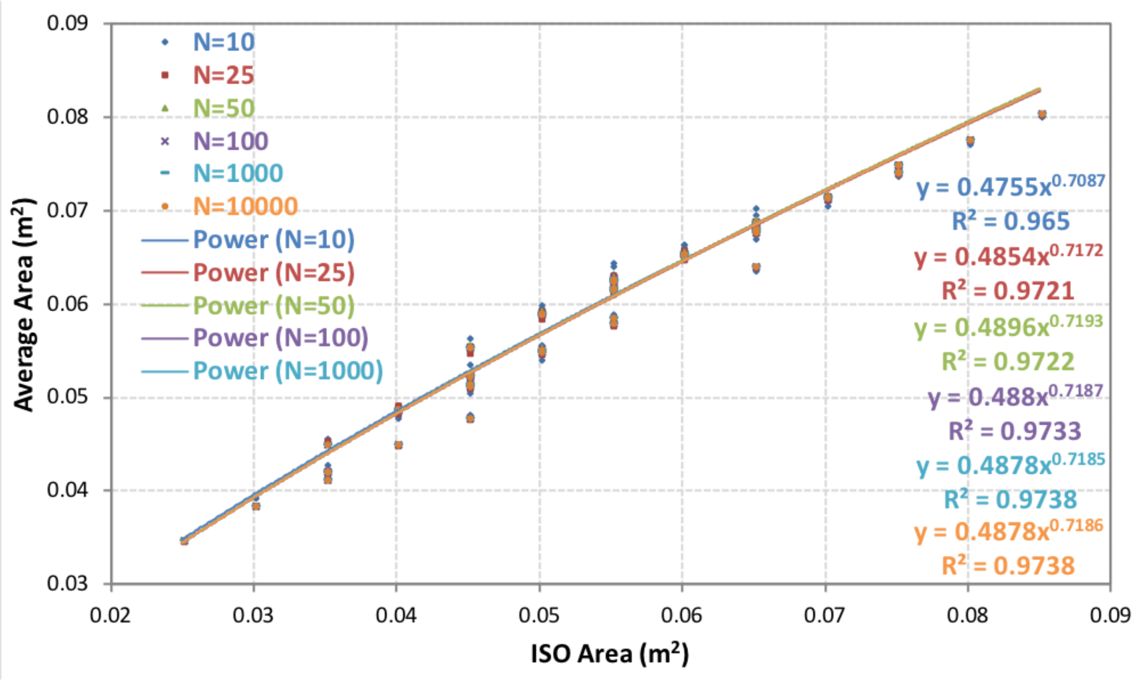

Fig. 4.3 Comparison of Curve Fit

It can be seen in Figure 4.3 that the curve fits for the various spheres are extremely similar; therefore the 50-viewpoint sphere is used herein as it offers a compromise between the improvement in computational efficiency and the loss of accuracy. The following procedure could, however, be repeated using a greater number of viewpoints to improve the accuracy of the end result. This curve fit can now be used as a correction factor for the ISO standard. It should be noted, however, that it would only be applicable for the few configurations used to generate it, therefore it requires expansion to include further configurations before application.

4.1.1 The Correction Factor

The curve fit is expanded to include 325696 unique CubeSat configurations, in order to be a more effective correction factor for most probable configurations of CubeSats. These configurations vary from a basic 1U (i.e. 10 cm cube) to 6U each with between 0 and 8 deployable panels of various lengths, set at various angles (90°, 135° & 180°). This encompasses the majority of configurations of CubeSats already in orbit; this is, however, an incomplete list. Larger CubeSats and larger deployable panels, than those considered herein, have been proposed for future missions, therefore if considering cases out with those considered herein the trend-line used should be adjusted to incorporate those new possibilities.

To demonstrate the accuracy of the new correction factor it is compared to the average projected area calculation using the sphere of viewpoints and the ISO standard average cross-sectional area. Figure 4.4 shows the various configurations considered as different points. It can be seen that the average projected area calculated using the sphere of viewpoints is considerably smaller than the ISO standard area for the majority of configurations. There is one exception to this rule, however, for the few configurations where there are no deployable panels the ISO standard is accurate.

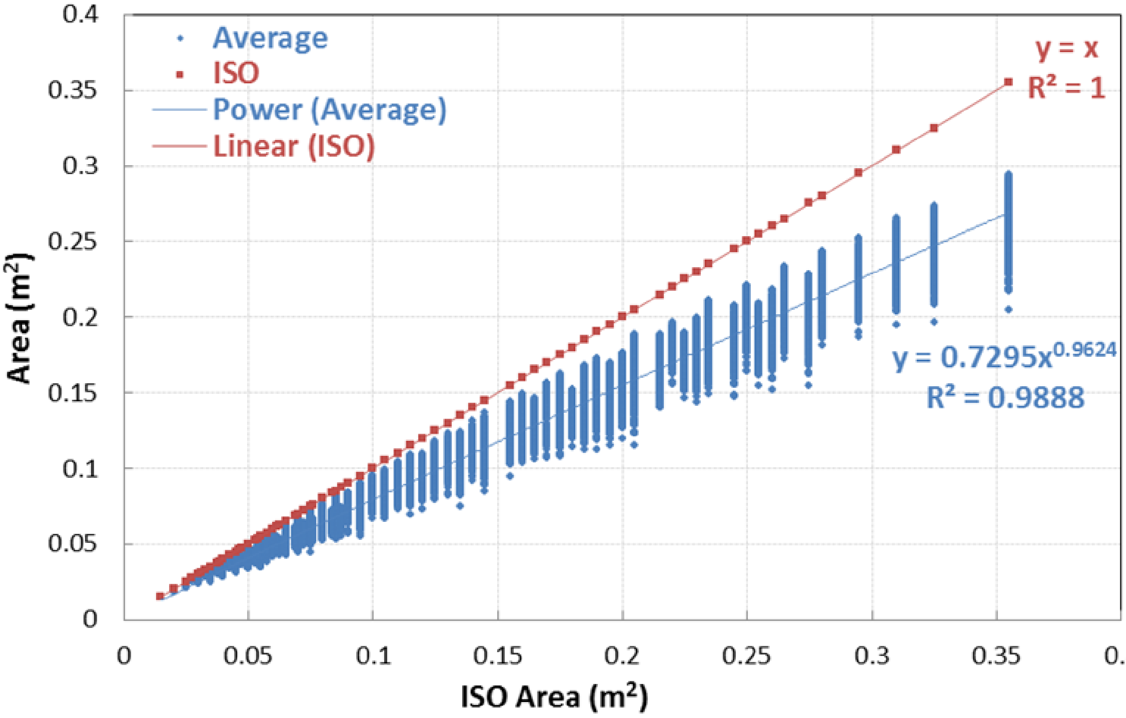

Fig. 4.4 Comparison of Curve Fit and ISO Standard

It is apparent from Figure 4.4 that the curve fit generated using the new data set, including all probable CubeSat configurations, provides a more accurate estimate of the projected area than the ISO standard. Therefore, this curve fit should be used as a correction factor to the ISO standard when considering CubeSats with deployable panels. The projected area of a CubeSat with deployable panels can therefore be calculated as

$$S_C = 0.7295 S_{ISO}^{0.9624} \tag{4.3}$$

where S_{ISO} is the area determined using the ISO standard method. In order to properly quantify difference in accuracy due to including the correction factor, the percentage errors in the ISO standard and the correction factor are compared. In order to calculate the percentage error the average area calculated using the viewpoint sphere is considered to be the truth. The comparison is shown in Figure 4.5 and Table 4.2.

Table 4.2 Accuracy Comparison of Correction Factor and ISO Standard

	Correction Factor	ISO Standard
Average Absolute %Error	4.24	26.79
Average % Error	0.14	26.79
Error Standard Deviation	5.33	7.20
3σ bounds	-15.86,16.15	5.18,48.41

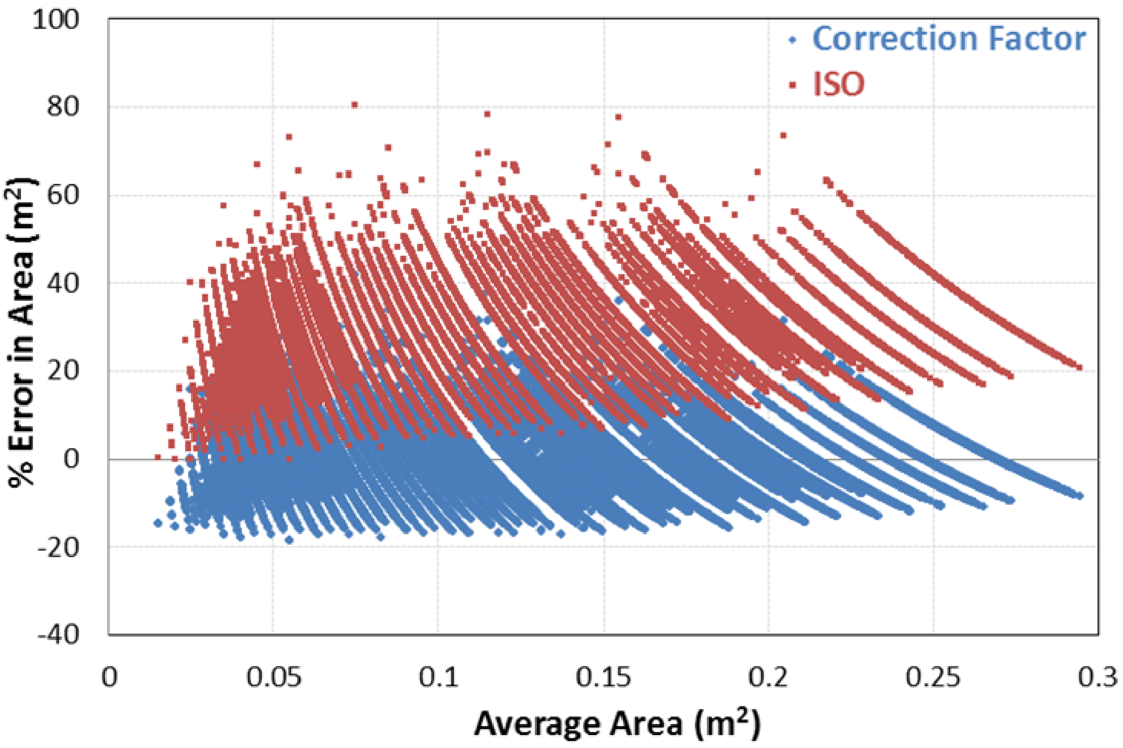

Fig. 4.5 Accuracy Comparison of Correction Factor and ISO Standard

It can be seen from Table 4.2 and Figure 4.5 that the average absolute error in the projected area, calculated using the correction factor, is much smaller than when using the ISO standard. It should be noted that the absolute error is used for this comparison as it provides a better understanding of the accuracy of the method, while the average error for the correction factor is approximately 0% the absolute error is 4.24%, meaning that on average the error in the projected area is ±4.24%. It can also be seen in Table 4.2 that while the ISO standards 3rd standard deviation still excludes 0%, the correction factor is focussed around approximately 0%. The correction factor also produces a much smaller spread of errors as is demonstrated by the standard deviation. It can also be seen that the error in the ISO standard is consistently positive, meaning that the ISO standard always overestimates the area, excepting for the configurations with no-deployable panels. Though this may seem to give a conservative estimate of the projected area, it will give an orbit lifetime prediction that will be considerably shorter than could be expected. Therefore, using the ISO standard to demonstrate space debris mitigation law compliance is not recommended. Given the data it is recommended, provided speed is not an issue, that the average projected area be calculated using the sphere of viewpoints. If, however, speed is an issue the new correction factor should be used, with an uncertainty of ±10.66%.

4.2 Refining Re-entry Date Predictions

The previous section looked at improving the estimation of the average projected area of a randomly tumbling spacecraft. However, if the tumble is not perfectly random this method is unlikely to yield good results, likewise when the drag coefficient and mass are unknown an accurate orbit propagation is impossible. Estimating the ballistic coefficient post-launch from orbit tracking data is one way to circumvent these issues. By taking tracking data and knowing how an orbit should evolve, the ballistic coefficient can be retrieved. In this way the ballistic coefficient can be estimated for objects where it is unknown, or confirmed/corrected for those where it is known to some degree. This effectively decouples the propagation from the ballistic coefficient.

In order to determine the most accurate way of incorporating spacecraft decay data several things must be considered. Firstly, how to use the data to inform the prediction; secondly, how to integrate the data and finally, how many data points are required. The following sections will deal with each of these in turn. Note all orbit lifetime predictions made using this method are made using equations 2.70 and 2.74 from Chapter 2 as appropriate, and the spherically-symmetrical atmospheric model derived in Chapter 3.

4.2.1 Estimating Initial Parameters

One of the main problems with using general perturbations methods in orbit propagation is the dependence on accurate estimation of the input parameters. This section will focus on improving the accuracy of these parameters. In essence all of the methods proposed in this section are the same; they each build a variable that incorporates the uncertain input parameters to be considered in the prediction. These variously include: the mass, drag coefficient, projected area, atmospheric density, and the retarding force created by atmospheric rotation. These parameters can all be considered to some degree uncertain; therefore they will all be considered to determine their relative impact and in order to ascertain the most appropriate formulation of the variable. The variable built will be designated B^* in all cases. Each formulation of B^* will contain the projected area and drag coefficient, as these two variables cannot be measured or modelled accurately, so it is assumed that they will always contribute a relatively large portion of uncertainty. Mass, atmospheric density and atmospheric rotation can all be measured or modelled to some degree of accuracy so they are variously included or not in the formulation of B^*. Combining these 5 parameters, 8 variants of the formulation can be obtained including the traditional form for the ballistic coefficient, BC, as shown in equation 4.1. Alongside the traditional form, the following 7 B^* variants are considered

$$B_1^* = \frac{m}{\rho F S C_D} \tag{4.4}$$

$$B_2^* = \frac{m}{F S C_D} \tag{4.5}$$

$$B_3^* = \frac{m}{\rho S C_D} \tag{4.6}$$

$$B_4^* = \frac{1}{\rho F S C_D} \tag{4.7}$$

$$B_5^* = \frac{1}{\rho S C_D} \tag{4.8}$$

$$B_6^* = \frac{1}{F S C_D} \tag{4.9}$$

$$B_7^* = \frac{1}{S C_D} \tag{4.10}$$

where m, S, C_D, F, and ρ are as previously defined.

4.2.2 Decay Data Integration

Several methods of integrating the decay data can also be considered. Firstly, the previous points may be used individually to calculate multiple B^* values which are then averaged. Secondly, a data point several points before, but ignoring those in between, may be used to calculate B^*. Finally, a trend may be drawn from multiple B^* values. For the first and third methods the B^* value is calculated using multiple short time steps, as seen in Figure 4.6a whilst the second method uses a larger time step encompassing multiple data points to calculate B^* as seen in Figure 4.6b.

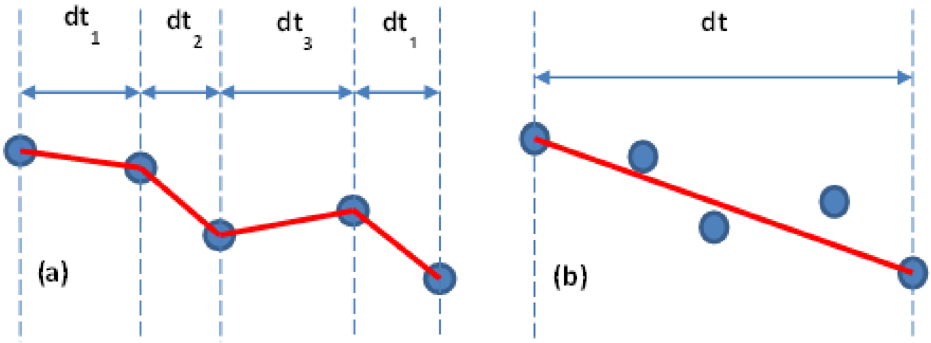

Fig. 4.6 Decay Data Integration Method Comparison

All three methods were considered for each B^*, however, after some initial testing using historical data it was found that only the second method was viable. Therefore, the second method is used from here onwards. This method involves rearranging the orbit lifetime equations 2.70 and 2.74 from Chapter 2 to find the value of the various B^* parameters, using the time and position change between the past and current data points. For example, using decay data the traditional ballistic coefficient is calculated as

$$BC = \frac{HT_0}{2\pi\rho_0 a_0^2 F\Delta t}\left(1 - \mathbf{e}^{\beta a_0\left(\left(\frac{T}{T_0}\right)^{\frac{2}{3}}-1\right)}\right) \tag{4.11}$$

where values with subscript 0 are calculated at the past data point position and Δt denotes the time between the past and current data points. This newly calculated ballistic coefficient is then used to predict the orbital lifetime from the current data point.

4.2.3 Number of decay data points required

In order to determine the number of decay data points required to produce accurate orbit lifetime predictions, historical data of a test case will be used. At each data point new predictions will be made using one previous data points to determine the various B^* values and therefore the lifetime predictions associated with each. Then, two previous data points will be used, and then three and so on until all previous points are used. This method will produce a matrix of orbit lifetime predictions which, when compared to the historical data, will produce a matrix of prediction errors. This error matrix can then be studied to determine the number of previous data points required to produce the most reliable predictions. The full analysis can be found in Chapter 5

Chapter 5

Validation of the Developed Models for Use in Orbit Propagation

Before any of the models developed in Chapters 2, 3 and 4 can been used in any application, they must be validated. The following sections will deal with the validation of each of the developed methods in turn.

5.1 Validation of Orbit Lifetime Analysis Method and Spherically Symmetrical Atmospheric Model

Validation of the orbit lifetime analysis method and spherically-symmetrical atmosphere is conducted using data from historical missions, as detailed in Table 5.1. Attitudes of a decaying spacecraft can be difficult to predict since most will have lost power by re-entry, as such they are unable to maintain a steady attitude and will tumble, altering the drag coefficient and cross-sectional area, and complicating the analysis. Each of the satellites in Table 5.1 were chosen for this validation as they are approximately spherical, removing the uncertainty which would be introduced by the attitude awareness problem. With the mass, cross-sectional area, drag coefficient, initial epoch and orbit of the mission defined from [12,90,91], all the parameters affecting the lifetime calculations are fixed and invariable within this validation. It should be noted that drag coefficient cannot be measured, the values given in Table 5.1 are derived values given in the literature. For further information on how these values are derived please see appropriate references.

Table 5.1 Validation Mission Spacecraft Characteristics

Spacecraft Name	NORAD No.	Mass (kg)	Area (m^2)	Drag Coefficient
ODERACS-A	22990	1.482	0.0081	1.93
ODERACS-B	22991	1.482	0.0081	1.99
ODERACS-E	22994	5	0.0182	1.96
ODERACS-F	22995	5	0.0182	2.01
ODERACS-2A	23471	5	0.0182	1.97
ODERACS-2B	23472	1.482	0.0081	1.96
GFZ-1	23558	20.63	0.0362	2.16
Starshine-1	25769	39.46	0.181	2.16
Starshine-2	26929	38.56	0.181	2.15
Starshine-3	26996	90.04	0.6939	2.01
ANDE-Castor	35694	50	0.183	2.20
ANDE-Pollux	35693	25	0.183	2.20[*]
Calsphere-3	04957	0.73	0.0507	2.03
Calsphere-4	04958	0.73	0.0507	2.03
Calsphere-5	04963	0.73	0.0507	2.03
Cosmos 1427 (Yug-2)	13750	750	3.141593	2.05
Cosmos 1615 (Yug-3)	15446	750	3.141593	2.05
Cosmos 2137 (Yug-4)	21190	750	3.141593	2.05
Cosmos 1450 (T2-1)	13972	750	3.163622	2.18
Cosmos 1534 (T2-2)	14668	750	3.163622	2.18
Cosmos 1631 (T2-3)	15584	750	3.163622	2.18

5.1.1 Orbit Lifetime Calculation using the Single Curve versus Multiple Curve Atmospheric Density Model

The Modified King-Hele Method is applied to the spacecraft detailed in Table 5.1 to test the accuracy of the lifetime predictions produced. Before the method proposed herein is compared to other methods the single curve and multiple curve models for atmospheric density, as displayed in Figure 3.2 and Figure 3.3 respectively, are compared. It should be noted that for all predictions made using the new solar activity model, the solar activity data used is only that which would have been available to each mission prior to launch.

---

[*] As no drag coefficient is cited in the literature for these missions the ISO standard value of 2.2 was used.[17]

Table 5.2 shows that using the multiple curves from Figure 3.3 to model atmospheric density typically produces more accurate results than the single curves from Figure 3.2. Comparing the average errors, which are calculated by averaging the absolute error from all of the lifetime estimates given in Table 5.2, it is seen that in using multiple curves to model atmospheric density the method produces errors much smaller than those produced by the same method incorporating the single atmospheric density curves. This can be attributed to the increase in accuracy of the density model; in some cases the single curve density is an order of magnitude different to the multiple curve density, which introduces a large error in the orbit lifetime calculation.

Table 5.2 Lifetime Analysis Results vs. True Lifetimes of Validation Missions

		Single Density Curves		Multiple Density Curves	
Spacecraft Name	True Lifetime (Days)	Predicted Lifetime (Days)	% Error E_s	Predicted Lifetime (Days)	% Error E_m
ODERACS-A	235.1	240.4	2.2	234.7	-0.2
ODERACS-B	235.4	240.0	1.9	233.8	-0.7
ODERACS-E	384.4	380.1	-1.1	369.1	-4.0
ODERACS-F	378.6	374.2	-1.1	363.1	-4.1
ODERACS-2A	401.4	380.5	-5.2	383.1	-4.6
ODERACS-2B	236.1	236.8	0.3	239.4	1.4
GFZ-1	1523.5	1643.7	7.9	1465.6	-3.8
Starshine-1	258.3	314.6	21.8	261.9	1.4
Starshine-2	130.7	156.5	19.7	146.0	11.7
Starshine-3	477.9	540.0	13.0	447.2	-6.4
ANDE-Castor	383.3	343.4	-10.4	359.7	-6.2
ANDE-Pollux	240.9	198.7	-17.5	212.6	-11.7
Calsphere-3	2479.0	2442.7	-1.5	2419.3	-2.4
Calsphere-4	2451.7	2419.1	-1.3	2377.5	-3.0
Calsphere-5	2191.5	2170.2	-1.0	2162.9	-1.3
Cosmos 1427 (Yug-2)	2469.8	2811.5	13.8	2357.2	-4.6
Cosmos 1615 (Yug-3)	1939.2	2368.6	22.1	1969.5	1.6
Cosmos 2137 (Yug-4)	1474.3	1848.0	25.3	1464.1	-0.7
Cosmos 1450 (T2-1)	2609.2	3122.3	19.7	2543.5	-2.5
Cosmos 1534 (T2-2)	2426.3	3001.4	23.7	2423.1	-0.1
Cosmos 1631 (T2-3)	2109.1	2682.3	27.2	2104.7	-0.2
Average Absolute Error		11.33 %		3.46 %	
Absolute Error Standard Deviation		9.44 %		3.25 %	

When considering the multiple curves method it can be seen that with the exception of two missions, the predictions generally fall within the 10% range, in fact the average error across all of the missions is 3.46% and the standard deviation in error is 3.25%. It should be noted that one of the exceptions is the ANDE-Pollux mission which has an undefined drag coefficient, therefore that result is not necessarily reliable. The other is Starshine-2 which was by far the shortest mission duration considered. Further analysis would be required to confirm, however it can be surmised, that due to short-term spikes in solar activity, short period errors are not well-captured within the input monthly averaged solar activity data, and that using weekly or even daily averaged data could reduce the error for this spacecraft. Table 5.2 is shown in graphical form in Figure 5.1.

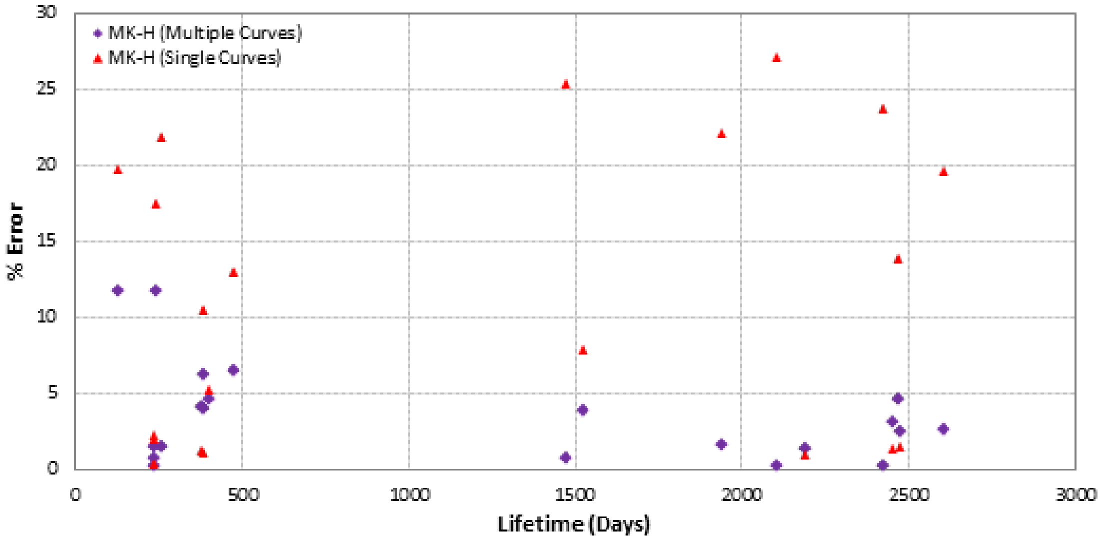

Fig. 5.1 Method validation for historical spacecraft detail in Table 5.2

When considering the validation results graphically it becomes clear that, while the error in the single curve results somewhat mask the trend, the largest errors in the multiple curve method tend to occur in the lowest lifetime missions. This is likely due to short duration spikes in solar activity, which over a longer lifetime would have averaged out but causes a greater uncertainty in the atmospheric density in the short duration. Applying a Monte Carlo analysis with the solar condition input as a variable would address this uncertainty.

If we remove the ANDE spacecraft (the two spacecraft with undefined drag coefficients) from the list the average error from the remaining lifetime estimations decreases to 2.88%. Using this to define upper and lower lifetime boundaries, a range for the drag coefficient of each of these two spacecraft can be derived from the true lifetime: ANDE-Castor likely had a drag coefficient in the range 2.01-2.13, while ANDE-Pollux likely had a coefficient in the range 1.89-2.00.

5.1.2 Orbit Lifetime Analysis using Low Eccentricity Equation versus Circular Equation

The orbit lifetime equations 2.70 and 2.74 are derived based on the eccentricity of the initial orbit; below 0.02 and zero, respectively. The formulation of equation 2.74 is simpler when compared to equation 2.70 which includes a Bessel function, and hence may be preferred for initial analysis. In order to determine the influence of eccentricity on the accuracy of the two lifetime equations the difference in absolute percentage errors in the orbit lifetime estimations given by each equation is examined. This difference is calculated as,

$$Diff = \left(\frac{\tau_{L(e=0)} - \tau_{L(true)}}{\tau_{(true)}} * 100\right) - \left(\frac{\tau_{L(e<0.02)} - \tau_{L(true)}}{\tau_{(true)}} * 100\right) \qquad (5.1)$$

where τ_L is the orbit lifetime estimated using equations 2.70 and 2.74 or the true orbit lifetime from historical record, as appropriate. By considering this difference in the absolute percentage error in the lifetime calculations against the initial orbit eccentricity for the 21 validation missions, see Figure 5.2, it is seen that the difference decreases with decreasing eccentricity. Given the structure of equation 5.1, a positive difference in Fig 5.2 shows that the low eccentricity equation is more accurate, while a negative difference shows that the circular equation is more accurate. Hence, from the general trend shown in Figure 5.2, and from the limited data set used, it could be inferred that when the eccentricity drops below approximately 0.001 the orbit may be assumed to be circular, and hence equation 2.74 could be used without loss of accuracy.

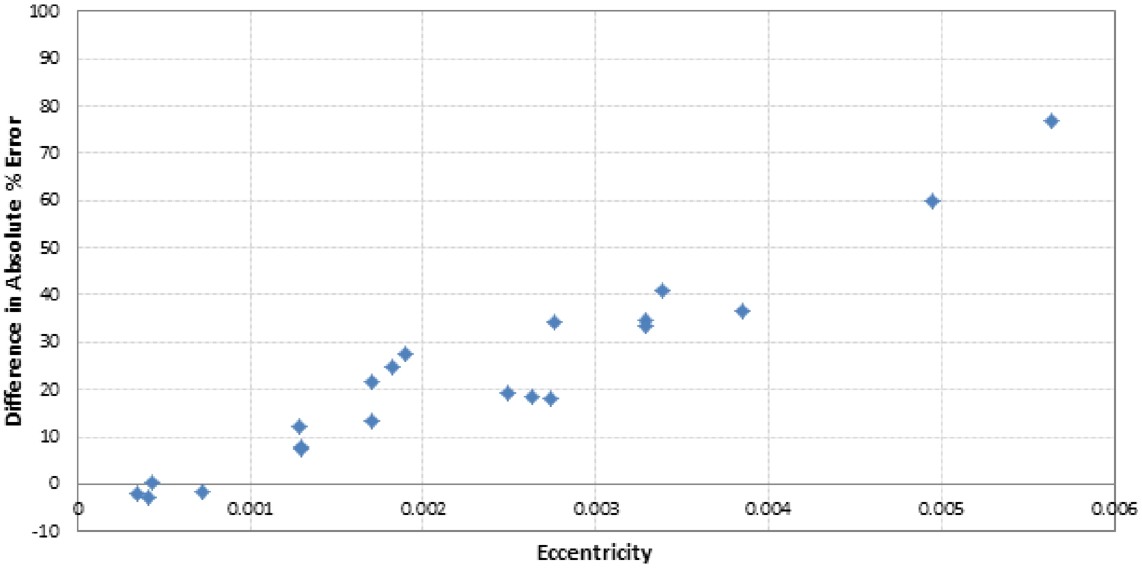

Fig. 5.2 Comparison of Results using Low Eccentricity and Circular Solutions

5.1.3 Comparison to Other Methods

To further verify the proposed method it is tested against other available methods. Two analytical methods are considered: the original King-Hele method, and the Griffin and French method.[23,24,26] It should be noted that neither of the analytical methods directly includes the effects of solar activity; however each of the 3rd party options considered has inbuilt options to include these effects. Third party software is also considered and while many options for orbit propagation and lifetime estimation exist, currently the most notable are: Systems Tool Kit by AGI, General Mission Analysis Tool and Semi-analytical Tool for End of Life Analysis by CNES.

Systems Tool Kit (AGI) Systems Tool Kit from AGI, often referred to as STK, is software that allows users to build and analyze virtual models of complex space systems with time-dynamic constraints. STK has a built in Lifetime Analysis Tool, which uses a special perturbations algorithm to compute the expected lifetime of a satellite based on atmospheric drag.[92] The lifetime analysis tool uses an algorithm which takes into account launch date, initial orbit, mass, cross-sectional area, and drag coefficient. The algorithm then computes the effect of atmospheric drag using the satellite characteristics, and atmospheric density and solar flux models chosen from several options. These options must all be considered to be sure the best available and most appropriate models are chosen.

Cojuangco examined the STK lifetime analysis tool and found that the NRLMSISE-00 density model was best suited to lifetime analysis in order to minimize errors.[93] The accuracy and speed of the analysis can be varied using the advanced options, which allow the time steps and the limit of the propagation to be set. As the speed was increased, the accuracy was decreased therefore a balance must be struck between the two.[93] The propagator used in the analysis can also affect the results. Cojuangco found that the High Precision Orbit Propagator (HPOP) numerical propagator was the most accurate for lifetime analysis. HPOP numerically integrates the differential equations of motion with a full range of perturbations including gravitational models, third-body interactions, solar radiation pressure, and atmospheric drag.[93]

General Mission Analysis Tool (NASA) General Mission Analysis Tool, more commonly known as GMAT, is not specifically an orbit lifetime estimation tool; however it is capable of performing the analysis.[94] It was originally designed as a trajectory optimization and mission analysis tool. GMAT was developed in collaboration with the wider space community and is an open source tool with a huge range of functionality. In terms of orbit lifetime analysis users have the choice of two different atmospheric models; the Jacchia-Roberts model and the MSISE-90 model. There is also a choice of several gravity models and of building in specific point masses.

Much like STK, GMAT is a special perturbations tool, with several available integrators; step size can be varied to provide more accurate solutions at the cost of computational time. After some initial study the authors found that the PrinceDormand78 was the most reliable and one of the more efficient integrators, therefore it was selected for this study. The Jacchia-Roberts atmosphere is generally accepted to be more accurate and up-to-date than the MSISE-90 model so it was used in this study. Ideally the CIRA model would be built in as the software is open source, and can be updated. However, it was decided that the initial comparison of the software and general perturbations methods should be done without altering the software.

Semi-analytical Tool for End of Life Analysis (CNES) Semi-analytical Tool for End of Life Analysis, known simply as STELA, was specifically designed by the French Space Agency to give reliable orbit lifetime estimations for spacecraft in the LEO and GEO protected regions and in GTO.[95] The IADC and ISO guidelines set out these protected regions and a recommendation that spacecraft operating in these regions should be removed within 25 years of decommissioning, in order to prevent a catastrophic build-up of space debris in these regions of interest.[16,15] STELA allows users to quickly estimate the remaining orbit lifetime of a spacecraft in a specific orbit in these regions.

STELA has a number of in-built options including two different atmosphere models, and three methods of estimating the drag coefficient. In this comparison study the drag coefficients are known thus they are included using the first of the three options, a user defined constant. The other options were a variable drag coefficient, taken from an in-built file or Cook's method of estimation. The two atmosphere options are NRLMSISE-00 or US76; the NRLMSISE-00 model is generally considered to be the more up-to-date and accurate of the two. Within the NRLMSISE-00 model the user is given three options of how to include solar activity; as a mean constant value, as a user-defined constant value, or as a value taken from an in-built file. The third option includes historical data of solar flux and geomagnetic indices from present, dating back to 1956. The file also includes future mean predictions of solar flux and geomagnetic indices determined by NOAA and NASA, as stated in the STELA user's manual. This file can be updated or even replaced by a file of the user's choice. Using this file is recommended when completing typical lifetime estimation; however there are cases where the mean options would be more appropriate.

5.1.4 Results of the Method Comparison

GMAT and STK were found to be the most promising numerical methods of the software choices, while STELA is also a promising semi-analytical tool. Therefore, these three tools are selected for comparison.

An orbit lifetime analysis of each of the selected historical missions was completed using each of the analytical and third party software methods. The results tabulated in Table 5.3 and plotted in Figure 5.3, show the comparison of the modified King-Hele method (MK-H(CIRA)) developed in Chapter 2, to the original King-Hele method updated to include the CIRA density multiple curve model and density index (K-H(CIRA)). Comparison is also made to the original King-Hele method updated to include just the CIRA density multiple curve model for average solar conditions, without the density index (K-H (Avg. CIRA)). Also included is the Griffin-French analytical method[26], which is similar to the original King-Hele method, and uses the CIRA density multiple curve model for average solar conditions to calculate lifetime using a standardised equation, however it's derivation limits its appropriate application to initially circular orbits.[26]

Table 5.3 Comparison of Accuracy of Discussed Methods

Method	Average Absolute % Error	% Absolute Error Standard Deviation
MK-H (CIRA)	3.46	3.25
K-H (CIRA)	5.10	3.60
K-H (Avg. CIRA)	50.44	24.96
Griffin-French	50.73	25.88
STK	11.39	10.69
STELA	6.63	7.00
GMAT	149.11	161.18

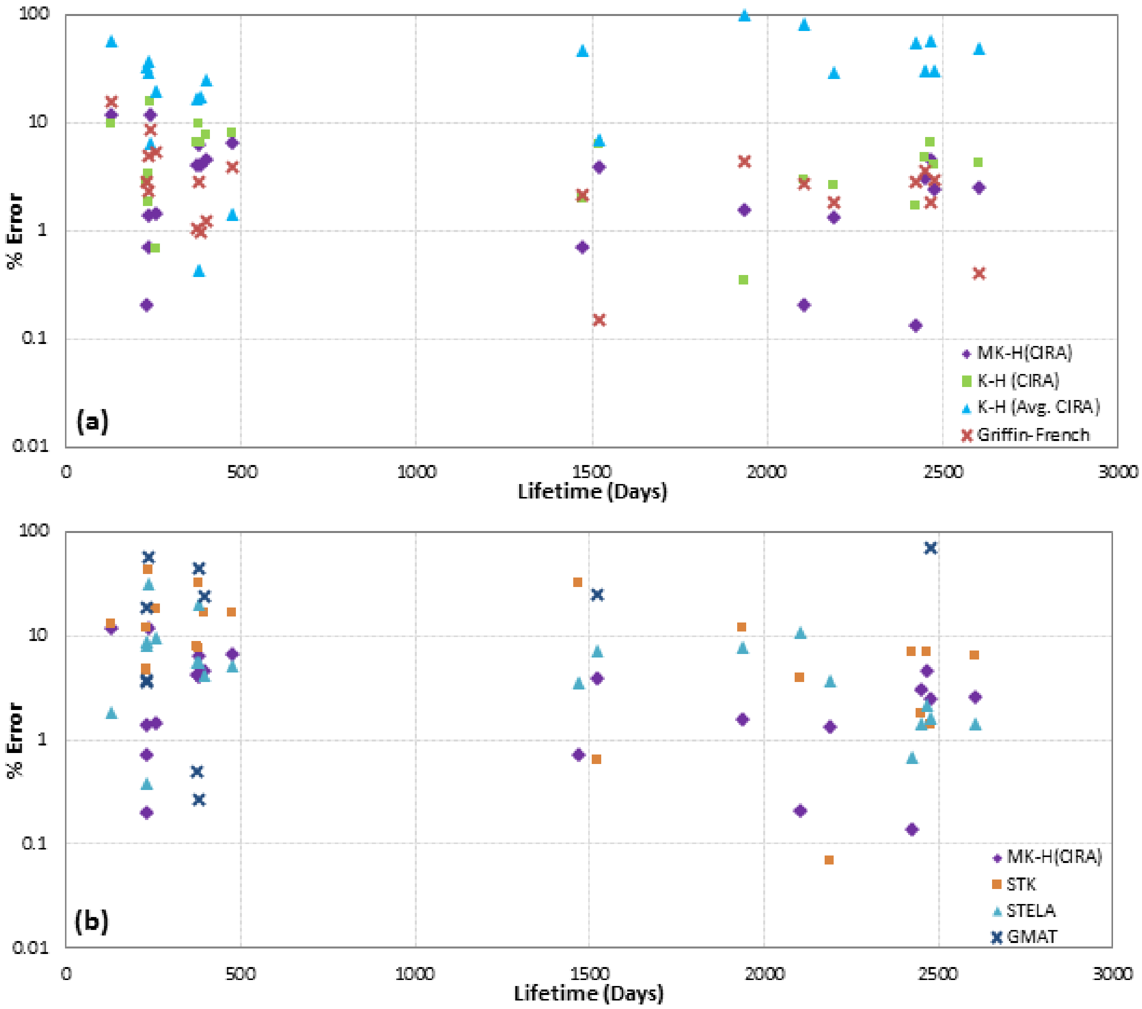

Fig. 5.3 Accuracy Comparison of Discussed Methods (N.B. logarithmic y-axis); (a) general perturbation methods, (b) 3rd party software

Table 5.3 shows that the Modified King-Hele method with the new atmospheric model produces the most accurate results. It is the only method that produces an average error of less than 5%; the next best result coming from the original King-Hele method (including new atmospheric and solar activity models) with an average error of 5.1%. This result shows that the modifications made in the re-derivation of the King-Hele method improve accuracy, on average, by approximately 1.5%. However, perhaps of more importance is the comparison of the original King-Hele method with and without the density index included; the inclusion of the density index gives an improvement of around 45%. Thus it has been shown that the inclusion of solar activity effects on density is vital. The most accurate third party software is STELA, with an average error of 6.63%. GMAT is found, in this limited trial, to be the least accurate of the compared solutions, further analysis is required to discover why it performed so poorly in this study.

Over the lifetime the perigee, apogee and eccentricity can be plotted to determine exactly how the spacecraft de-orbits. However, analytical methods, such as those developed herein, will only provide average solutions. These average solutions do not capture short period oscillations, such as the oscillation in altitude created by the eccentricity of an orbit; an object's altitude will decrease as it moves from apogee to perigee and increase as it moves from perigee to apogee.

5.2 Validation of the Non Spherically Symmetrical Model

In order to demonstrate the variation in orbit lifetime analysis results when including the diurnally varying density model, a case study is carried out using a sun-synchronous satellite. The spacecraft and orbit parameters for this case study are contained in Table 5.4. Note, the right ascension of the ascending node is not given in Table 5.4 as it was allowed to vary between 0 and 360° to show the variation this parameter makes in the orbit lifetime prediction. Figure 5.4 shows the predictions made using the general perturbations method derived in Chapter 2, given the parameters shown in Table 5.4.

Table 5.4 Case Study Spacecraft and Orbit Parameters

Parameter	Value
Epoch	1st January 2016 00:00:00
Mass	1 kg
Projected Area	1m^2
Drag Coefficient	2.2
Altitude	800 km
Eccentricity	0
Inclination	98.6°
Argument of Perigee	0°
Mean Anomaly	0°

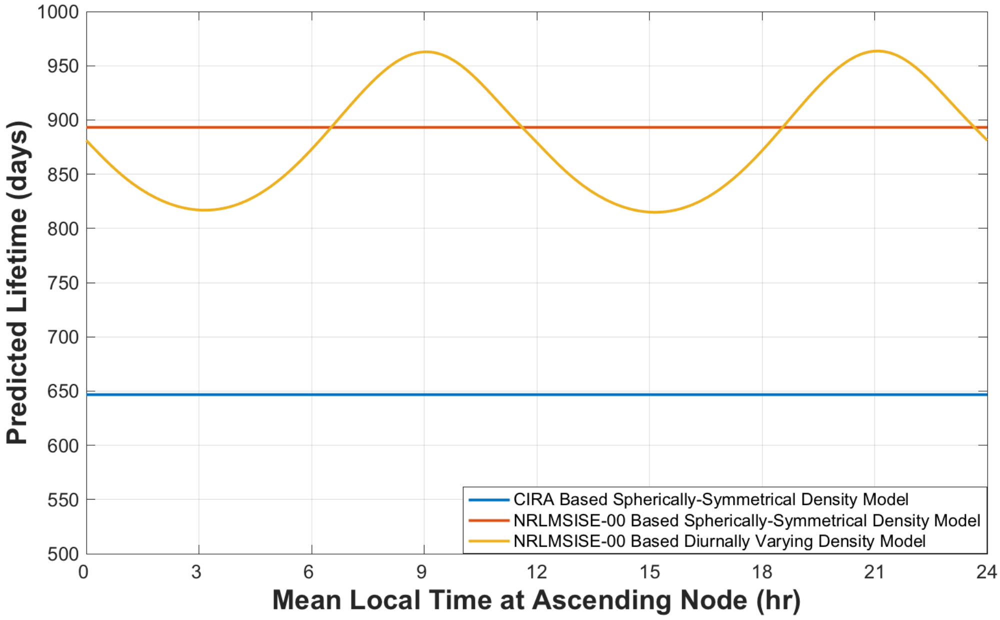

Fig. 5.4 Comparison of lifetime predictions using various density models

It is shown in Figure 5.4 that the orbit lifetime prediction can vary up to approximately 92 days under, and approximately 61 days over the mean lifetime when including the diurnal variation. This equates to approximately -10.3% and +6.8% difference. However, more notable is the difference between the orbit lifetime predictions made using the CIRA based spherically-symmetrical model and the NRLMSISE based spherically-symmetrical model; in this case the difference is approximately 247 days. This accounts for nearly a third of the orbit lifetime.

The CIRA based model is shown in section 3.1 to produce reliable orbit lifetime estimations, therefore it is concluded that the sample data set from NRLMSISE used to build the diurnally varying atmospheric model is not representative and should be expanded. It is expected that when including a larger data set, the effect of the diurnal variation on the mean density will remain as it is shown in this section; however the mean density is expected to shift to be more comparable to the mean density given by the CIRA based model. Therefore, the diurnal effect is still concluded to be an important effect to include in modelling the atmosphere, though not as significant as other effects such as the solar activity, which provides an improvement of approximately 45%, as seen in Table 5.3.

5.3 Validation of the Method for Refining Re-entry Date Predictions

To determine the accuracy improvement made by incorporating spacecraft tracking data into orbit lifetime predictions as discussed in Section 4.2 a test case is required; GOCE (COSPAR spacecraft identification 2009-013A) is considered for this purpose. GOCE (Gravity Field and Steady State Ocean Circulation Explorer) was one of ESA's first Living Planet Programme satellites, which was tasked with mapping the Earth's gravity field.[96] After a successful mission GOCE ran out of fuel and began an uncontrolled decent mid-October 2013, re-entering on November 11th 2013. For the purposes of this section, only this final portion of the spacecraft's orbit lifetime is considered. The aim is to determine the most accurate way of incorporating spacecraft tracking data to inform orbit lifetime predictions; in order to do this several things must be considered.

The matrix of prediction errors, discussed in Section 4.2.3, was built using historical data taken from GOCE's two line element (TLE).[12] The input parameters for GOCE considered were the published estimates: mass approximately 1050 kg, projected area approximately 1 m^2 and the ISO standard assumption of a 2.2 drag coefficient.[17]

As discussed in the Section 4.2.3 all possible numbers of available data points (N) were considered, however, due to the abundance of data it cannot all be displayed herein therefore a representative selection is presented for study. Table 5.5 shows the mean percentage error for each B^* (see Equations 4.1 and 4.4-4.10) with the selection of numbers of available data points used. To determine this mean percentage error, the percentage errors in predictions made at each data point are calculated by comparing the predictions to the real lifetimes taken from the TLE, then averaging all of these errors to produce a mean. The standard deviation of the errors is also considered and presented in Table 5.6.

Table 5.5 Mean Percentage Error Comparison of Variations on B^*

N	BC	B_1^*	B_2^*	B_3^*	B_4^*	B_5^*	B_6^*	B_7^*
2	62.34	66.70	62.34	66.70	66.70	66.70	62.34	62.34
3	14.56	19.27	14.56	19.27	19.27	19.27	14.56	14.56
5	11.93	21.63	11.93	21.64	21.63	21.64	11.93	11.93
10	12.54	41.93	12.54	41.94	41.93	41.94	12.54	12.54
15	12.57	62.91	12.57	62.91	62.91	62.91	12.57	12.57
20	12.51	85.45	12.50	85.46	85.45	85.46	12.50	12.51
50	16.99	291.84	16.99	291.90	291.84	291.90	16.99	16.99
All	68.44	1847.77	68.45	1848.39	1847.77	1848.39	68.45	68.44

Table 5.6 Mean Percentage Error Standard Deviation Comparison of Variations on B^*

N	BC	B_1^*	B_2^*	B_3^*	B_4^*	B_5^*	B_6^*	B_7^*
2	168.15	176.92	168.15	176.92	176.92	176.92	168.15	168.15
3	15.44	19.07	15.44	19.07	19.07	19.07	15.44	15.44
5	11.34	13.47	11.34	13.48	13.47	13.48	11.34	11.34
10	14.73	31.37	14.73	31.38	31.37	31.38	14.73	14.73
15	16.63	46.24	16.63	46.25	46.24	46.25	16.63	16.63
20	17.61	61.44	17.61	61.46	61.44	61.46	17.61	17.61
50	22.53	163.78	22.53	163.82	163.78	163.82	22.53	22.53
All	0.79	132.55	0.79	132.60	132.55	132.60	0.79	0.79

In a cursory examination of Tables 5.5 and 5.6 similarities are immediately obvious between BC, B_2^*, B_6^* and B_7^* and between B_1^*, B_3^*, B_4^* and B_5^*. The chief difference between these two sets is the inclusion or exclusion of atmospheric density in the formulation of B^*, as is shown by Equations 4.1 and 4.4-4.10. The inclusion of density in B^* can be seen to have a significantly negative impact on predictions accuracy; this effect can also be seen to increase as more and more previous data points are incorporated. This may seem, at first, counter-intuitive, as the general assumption in science is that having more data is always better. However, because the atmospheric density varies greatly with altitude the use of more data points actually introduces a large error into the calculation of B^*. It is therefore deemed prudent to exclude atmospheric density from B^*.

It can be seen from comparison of BC, B_2^*, B_6^* and B_7^* that excluding the density increases the accuracy significantly. It can also be seen that the inclusion or exclusion of the mass and atmospheric rotation retarding force make very little impact on accuracy. This was to be expected as these parameters have a much smaller uncertainty than the drag coefficient and area, so much so that they create a negligible difference in this method. However, in order to capture the uncertainty in mass, small as it may be, as well as for simplicity, it is recommended that *BC* be used. Thus, from here onward only *BC* will be discussed.

It can be seen in Table 5.5 that there appears to be a turning point in the number of previous data points required to produce the best results. In order to better determine what this turning point is, the mean percentage errors for *BC* are plotted, see Figure 5.5. This turning point exists due to the variable nature of *BC*; because the drag coefficient varies depending on atmospheric conditions and the area will also vary as the spacecraft tumbles, *BC* is not a constant. Therefore, since data points are taken from spacecraft tracking data and each is at a different point in time, as more data points are used the variation in *BC* is lost in averaging, while using too few data points will fail to capture it accurately.

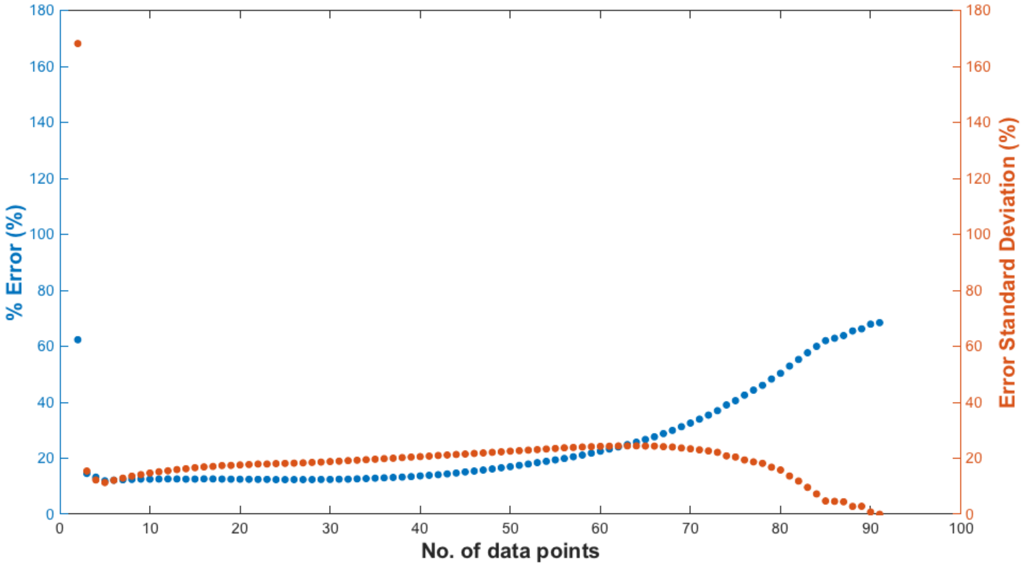

Fig. 5.5 Accuracy comparison for *BC* using various numbers of previously data points

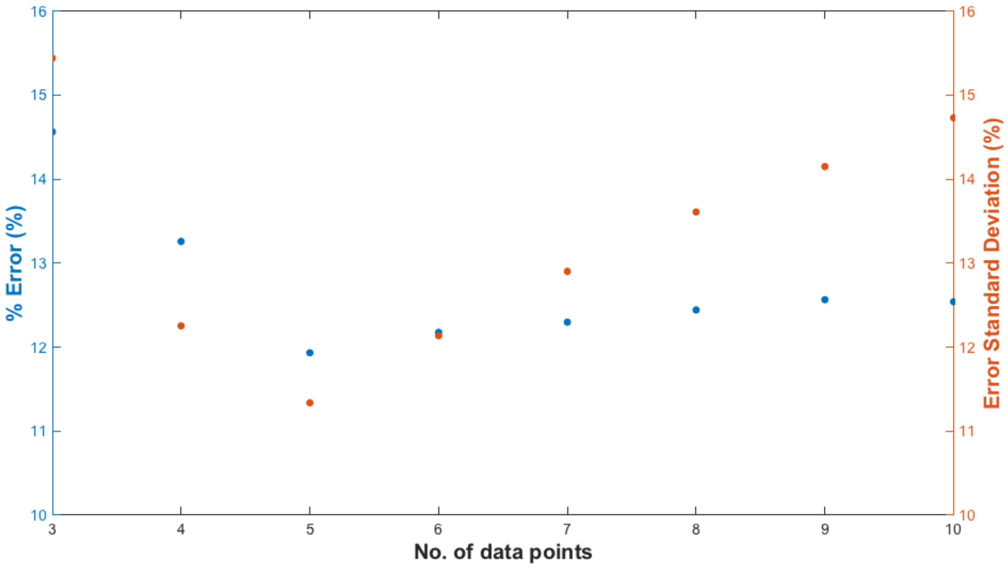

Fig. 5.6 Close Up of Relevant Part of Figure 5.5

It can be seen in Figure 5.5, and more clearly in Figure 5.6, that the turning point is at using 5 previous data points. Therefore, it is recommended that 5 data points be used. A case could be made for using more data as it can be seen that the percentage error remains relatively low between using 3 and 40 points. However when considering the standard deviation a steady rise can be seen, therefore keeping the number of points used to an absolute maximum of 30 is recommended.

Having established the most accurate combination of B^*, data integration method and the number of previous data points required, a comparison can be drawn between the original method previously presented in Chapters 2 and 3 and this updated version incorporating decay data. Propagating over the same period (i.e. with the same start epoch) using the original method and not including any decay data, the mean percentage error was found to be 24.57% (with a standard deviation of 9.77) compared with the 11.93% (standard deviation 11.34) of the refinement method. This demonstrates that the updated method produces a significant improvement in orbit lifetime prediction accuracy. It should be noted here, that while the updated method is now less sensitive to errors in the initial input parameters, the previously presented method is highly dependent on them. The assumed input parameters give a BC value of 0.002 m^2/kg, while using the decay data to calculate BC gives a mean value of 0.00225 m^2/kg from all the predictions. The BC values generated by the new method can be seen in Figure 5.7.

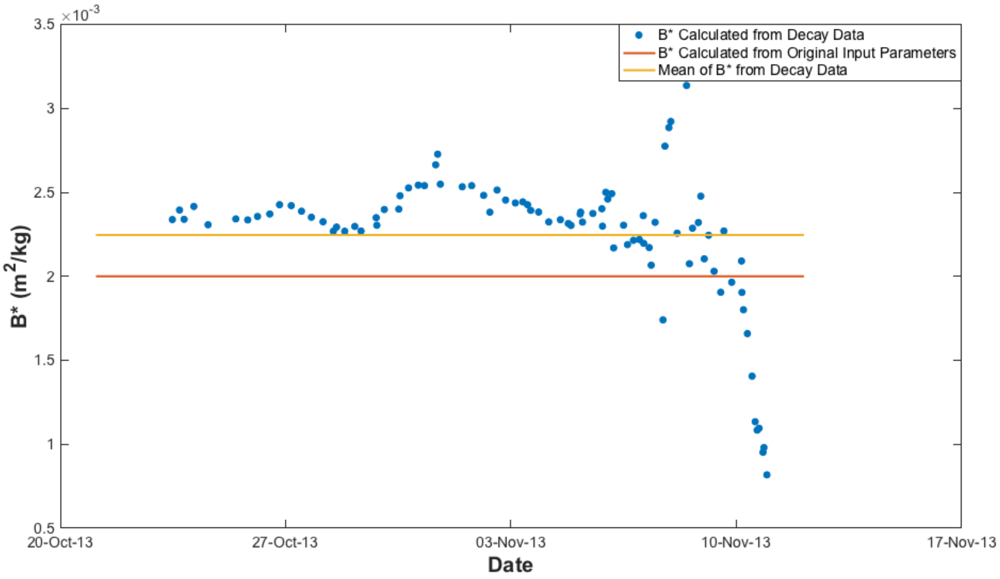

Fig. 5.7 Comparison of *BC* values

The new method is therefore entirely independent from the original estimates of mass, area and drag coefficient. So, taking for example an over estimation of the mass of GOCE to 1100 kg: this produces a mean percentage error in the previous method of 29.1% (standard deviation 9.50) whilst the new method maintains 11.93% error. Predictions at each data point can also be compared, as can be seen in Figure 5.8.

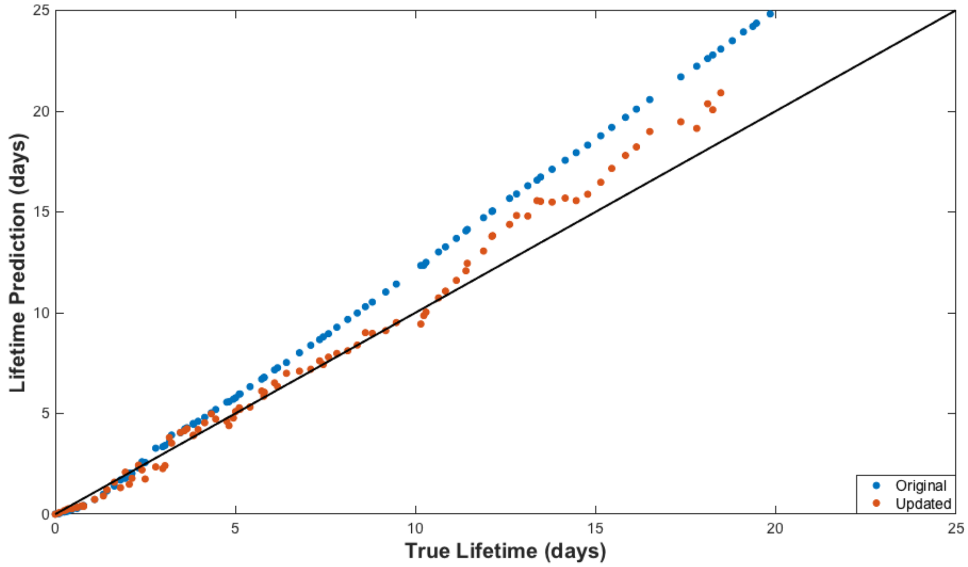

Fig. 5.8 Comparison of Original and Updated Methods Accuracy

In Figure 5.8 the solid black line denotes the 100% accuracy or 0% error. As the updated method follows this line much more closely this shows that the updated method produces significantly better predictions especially when considering the final 10 days. Within 10 days of re-entry, the updated method produces results that are almost exact, coming within a few hours of the true decay time whilst the old method deviates up to approximately 2.5 days.

Chapter 6

Applications

There are many applications for the methods and models developed herein, this chapter discusses some of these, particularly those associated with orbit lifetime analysis.

A major benefit of general perturbations methods including the Modified King-Hele method is the ability to operate in a so-called batch mode, enabling a user to run multiple simulations, or perform a Monte Carlo analysis without drastically increasing the time taken to solve. The Modified King-Hele method took 8.5 seconds to run a Monte Carlo analysis of 10000 simulations on each of the 21 historical missions detailed in Table 2; amounting to a total of 210000 simulations, each averaging just 40.5 microseconds. This test was done using non-optimized scripts within MATLAB R2014a, on a Windows 7 desktop computer with an Intel i7-3770 operating at 3.4 GHz and 16384 MB of RAM.

Adding a Monte Carlo analysis to the Modified King-Hele method offers the chance to see how the variation in parameters such as the initial eccentricity, the spacecraft mass or even the launch date will affect the predicted orbit lifetime. A Monte-Carlo analysis can also be used to provide confidence in the predicted lifetime by accounting for uncertainties introduced by including variations in parameters such as solar activity, thereby producing maximum and minimum orbit lifetime bounds for a mission. The probabilities produced by the Monte Carlo analysis can also be fed into higher levels of analysis, such as estimating mission costs or regulatory compliance checks. Uncertainties in spacecraft and mission specifications can be analysed in the same way to produce estimated orbit lifetime bounds, or a probability distribution can be used to inform the analysis further.

6.1 Dealing with Input Uncertainties

Uncertainties in the mass, projected area, drag coefficient, and launch date cause uncertainty in the orbit lifetime predicted, and a probability distribution can be applied to each variation to account for these uncertainties. Figure 6.1 shows the relationship between the variations in each specific parameter to the predicted lifetime of the ODERACS-A spacecraft, while Figure 6.2 shows the probability distributions generated by the same variations. ODERACS-A, one of the spherical spacecraft discussed in section 5.1 is used here as an example case. The variations in each parameter are produced using a normal distribution, centred on the estimated value of each parameter from Table 5.1. The value for the error in each parameter is selected based on how well the parameter is known, for example the mass is generally measured prior to launch so the uncertainty in it is typically very small.

For ODERACS-A the error in mass was set at ±1%, as was the estimated error in projected area, as these parameters were measured prior to launch and as such are only subject to measurement errors. The estimated errors in drag coefficient and density index were ±5% as they are both inferred parameters and as such are more likely to be subject to greater errors. Many factors affect the estimation of the drag coefficient including, but not limited to, the shape of the object, the surface properties of the object, and the properties of the fluid through which the object travels. The drag coefficient and density index, should be studied further to determine a specific method for determining estimated errors in each.

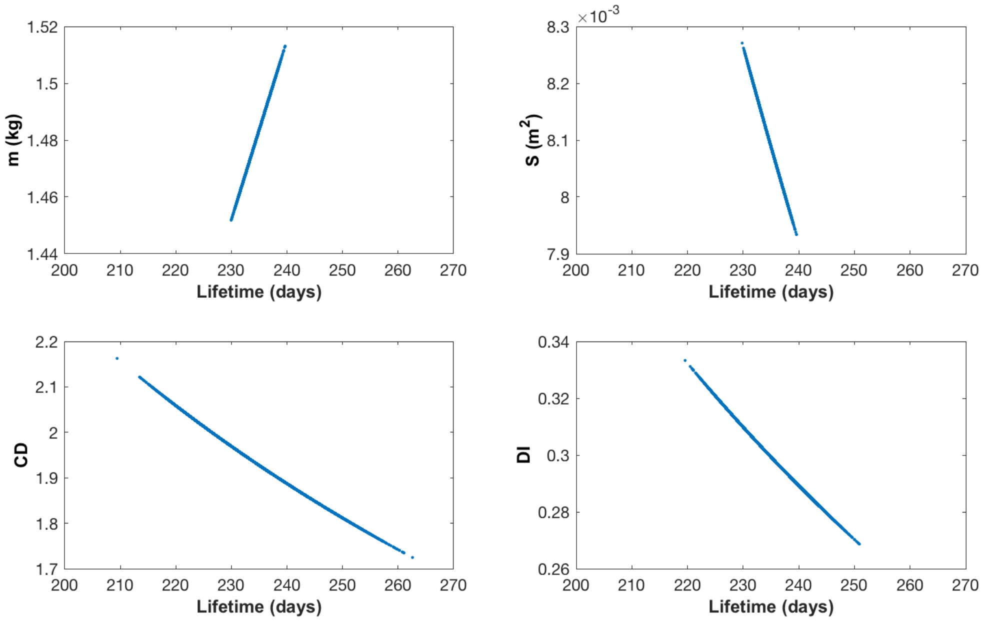

Fig. 6.1 Monte-Carlo Analysis of ODERACS-A Lifetime – Effects of Variations in Individual Parameters

It is seen from Figure 6.1 that while the variation in mass is directly proportional to the orbit lifetime (that is to say increasing the mass while holding the other parameters constant will increase the orbit lifetime), the projected area, and drag coefficient are both indirectly proportional. The relationship between the density index and lifetime is more complex; however there is a strong inverse correlation. It is seen here to have a relatively linear relationship; however this is not always the case. These relationships are as expected: increasing the mass, and/or decreasing the drag coefficient, and or the projected area will increase the potential forward momentum of the spacecraft leading to an increased lifetime. A decrease in the density index implies a decrease in atmospheric density, which would lead to a longer lifetime.

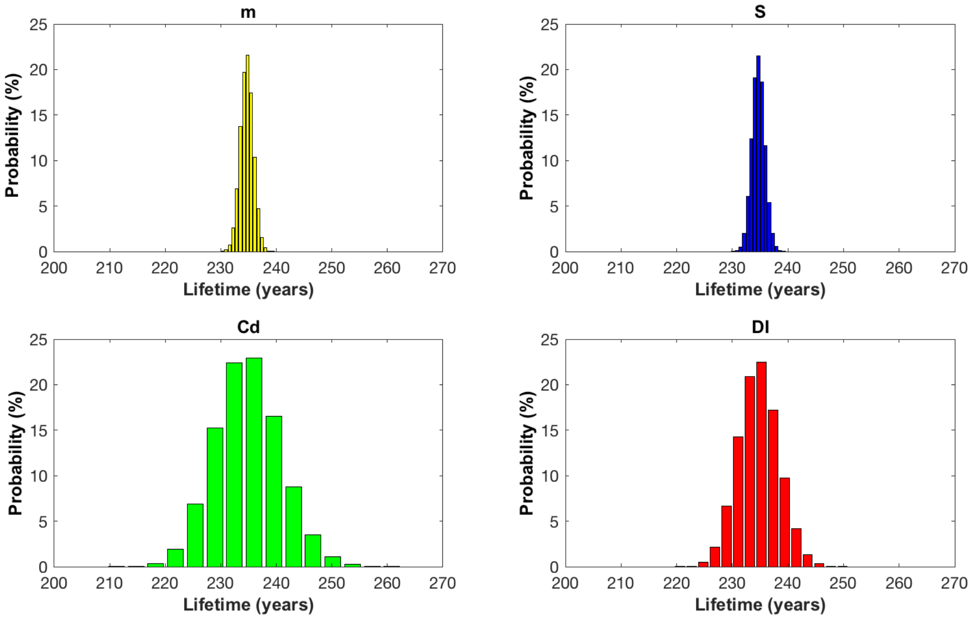

Fig. 6.2 Monte-Carlo Analysis of ODERACS-A Lifetime – Probability Distributions Showing the Effects of Variations in Individual Parameters

It should be noted that the launch date is actually a secondary parameter as it informs the density index, which then directly affects the predicted lifetime. These individual variations are overlaid for easy comparison, as seen in Figure 6.3.

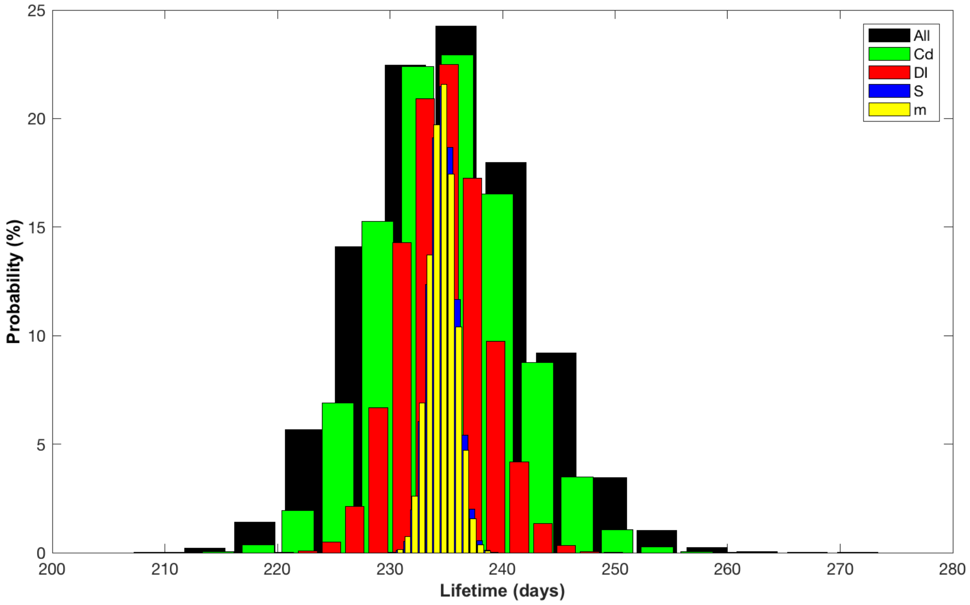

Fig. 6.3 Monte-Carlo Analysis of ODERACS-A Lifetime – Overlay of Individual Parameter Variations Probability Distributions

This overlay highlights that, for this case, the uncertainty in drag coefficient produced the largest uncertainty in the orbit lifetime predicted, while the uncertainty in the mass produced the smallest uncertainty in predicted orbit lifetime. This can be attributed directly to the percentage error applied due to the directly proportional relationship between mass and lifetime. However, upon examination of the spread produced by the density index and drag coefficient, both of which had the same percentage error estimation it becomes clear that variations in the density index has a much smaller effect on the lifetime of this spacecraft due to the complex nature of its relationship to lifetime.

For non-spherical spacecraft the cross-sectional area can be calculated based on the dimensions of the spacecraft and the projected tumbling mode. However, without knowing for certain how the spacecraft will tumble the area can only be determined with a degree of accuracy therefore it is recommended to find a best case scenario and a worst case scenario to provide informed bounds for a Monte-Carlo simulation.

The density index cannot be directly measured, rather it is inferred. It is recommended that in this case a fixed percentage error be applied to account for the largest range of possible errors. In the test cases a standard 5% error in the density index was assumed to produce the bounds for the Monte-Carlo simulation, however in some cases this error could be reduced or increased. For example, at solar minimum a reduction in error is expected as the solar flux measurements tend to be fairly steady, however at times of solar maximum the solar flux is more erratic, meaning the error applied should be increased.

The drag coefficient is even more difficult to calculate, as it is largely dependent on surface properties of the spacecraft and the properties of the fluid through which it travels. Again a fixed percentage error is recommended.

6.2 Providing Confidence in Predictions

The predicted orbit lifetime of ODERACS-A is approximately 235 days, as seen in Figure 6.3 and Table 5.2, with a standard deviation of approximately 4 days. This means that the probability of the actual lifetime being in the range 231-239 days is approximately 68% (1σ), whilst the probability of the actual lifetime being in the range 227-243 days is approximately 95% (2σ) and the probability of the actual lifetime being in the range 223-247 days is approximately 99.7% (3σ); the actual lifetime of ODERACS-A was in fact 235 days. By improving the knowledge behind the estimation of parameters, the standard deviation could be decreased and therefore the lifetime ranges produced can be narrowed, or the deviation can be better justified.

Confidence intervals, such as those discussed previously for ODERACS-A, are applied to the entire set of validation missions from section 5.1 to further demonstrate the accuracy of the Modified King-Hele method. The 95% (2σ) confidence interval can be seen in Figure 6.4, and the 99.7% (3σ) confidence intervals can be seen in Figure 6.5.

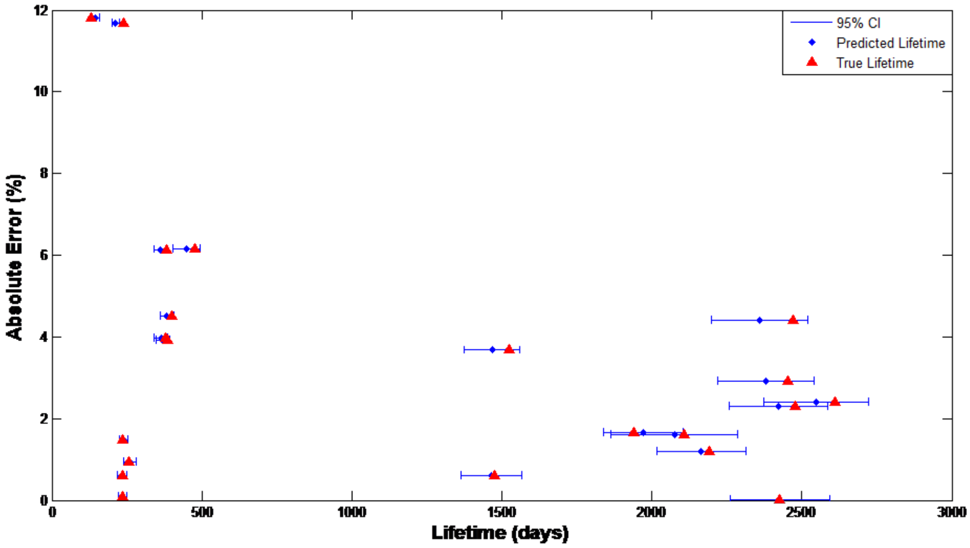

Fig. 6.4 Monte-Carlo Analysis of all Validation Missions (red markers – true lifetime, blue markers – predicted lifetime with attached 95% confidence interval)

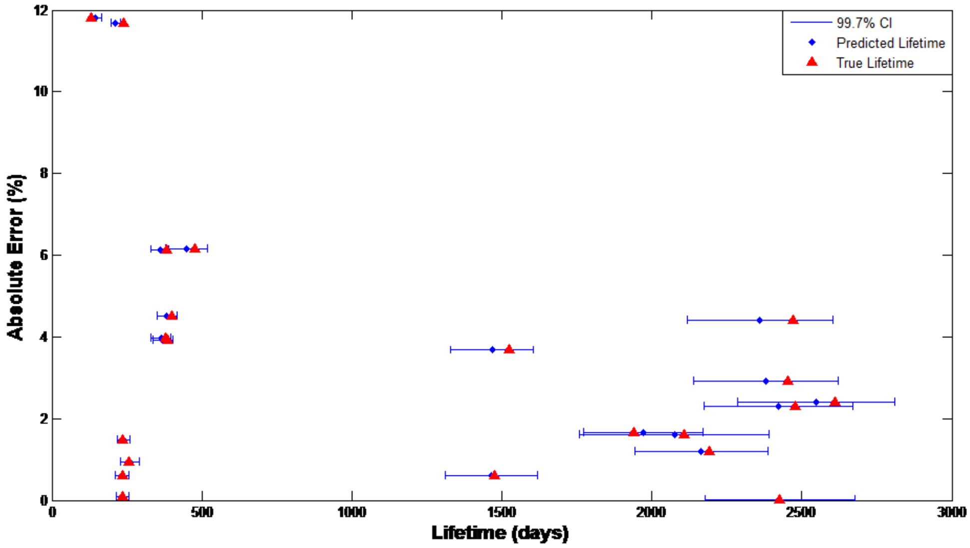

Fig. 6.5 Monte-Carlo Analysis of all Validation Missions (red markers – true lifetime, blue markers – predicted lifetime with attached 99.7% confidence interval)

In Figures 6.4 and 6.5 the blue ranges given are the confidence intervals, with blue markers representing the mean orbit lifetime predictions, whilst the red triangular markers show the true orbit lifetime of the spacecraft. It can be seen that in approximately three-quarters of cases the true lifetime falls within the 95% interval whilst in all but two cases the true lifetime falls within the 99.7% interval. The two cases that exceed the (3σ) interval are the same two missions that have errors above 10% (see Table 5.2), they are both short lifetimes and therefore though they fall outside of the interval the difference between the mean and the true lifetime is within 15 days. Since the confidence intervals are built using percentage variations on the input parameters, it is probable that the shorter the lifetime the more likely that the result will fall outside the confidence interval. And, as previously discussed short term spikes in solar activity activity will be more influential in such missions yet are not well-captured in the monthly average data used as input herein. Better insight into the most appropriate method of building confidence intervals could be generated by further study.

6.3 Maximum Allowable Altitude

To demonstrate the use of the Modified King-Hele method, with the embedded density index, on a non-historical mission the UKube-1 spacecraft (COSPAR spacecraft identification 2014-037F) is taken as a case study. Unlike the spacecraft used in the validation in section 5.1, UKube-1 is a standard 3U CubeSat with 3 deployed solar panels. The method derived in chapter 2 is applied, using the low eccentricity orbit lifetime equation, to provide an estimate of the maximum altitude that the spacecraft could have been launched to whilst still complying with best practice guidelines (that a spacecraft should de-orbit within 25 years of its end of life).[16,15,97]

Using UKube-1's launch date, specifications and the relevant ISO standard, ISO27852, for drag coefficient and averaged projected area with the correction factor developed in chapter 4, as defined in Table 6.1, the maximum allowable altitude can be predicted and a graph of the initial altitude versus the predicted orbital lifetime produced.[17] Note the semi-major axis, eccentricity, and inclination are taken from orbital tracking data, and as such are specified to the level of detail available.[12]

Table 6.1 Parameters used in UKube-1 orbit lifetime analysis

	Launch	Inactive
Date	8th July 2014	9th September 2016
Mass	3.98 kg	3.98 kg
ISO Projected Area with Correction Factor	0.0628 m^2	0.0628 m^2
Drag Coefficient	2.2	2.2
Semi-Major Axis	7006.23 km	6997.31 km
Eccentricity	0.0003369	0.0003628
Inclination	98.4032°	98.3371°

The current solar cycle, number 24, is considered a minimum cycle (explicitly its maximum is low when compared to other cycles); however, the magnitude of future cycles cannot be known. Therefore, three possibilities are considered as shown in Figure 6.6; that cycles 25 and 26 will both be minimum, average, or maximum cycles. Conservatively, the curve for consecutive minimum cycles should be used to decide a maximum altitude as this will ensure that the spacecraft de-orbits within the 25-year guideline. In the case of UKube-1 it can be seen from Figure 6.6 that the maximum allowable altitude would have been approximately 680 km, 54 km above the actual insertion altitude. UKube-1 is therefore concluded to have been inserted into a lower orbit than necessary to comply with the 25 year limit set out by the ISO and IADC guidelines.

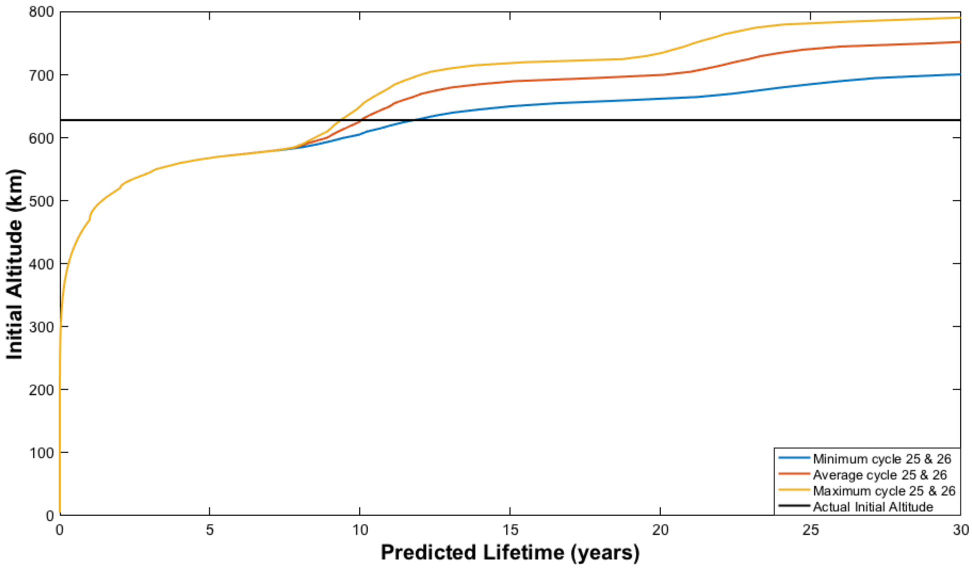

Fig. 6.6 UKube-1 predicted orbital lifetime versus initial altitude

6.4 Launch Window Selection

If the launch date was still undefined it can be set as a variable in, for example, 1 year steps. Figure 6.7 shows the results given three possibilities that the current and future cycles are all minimum, average or maximum cycles. The maximum allowable altitude then becomes a function of the launch date, varying between approximately 670 and 800km depending on the launch date as can be seen in Figure 6.7. However, for the purpose of demonstrating regulatory compliance the consecutive minimum curves should be assumed.

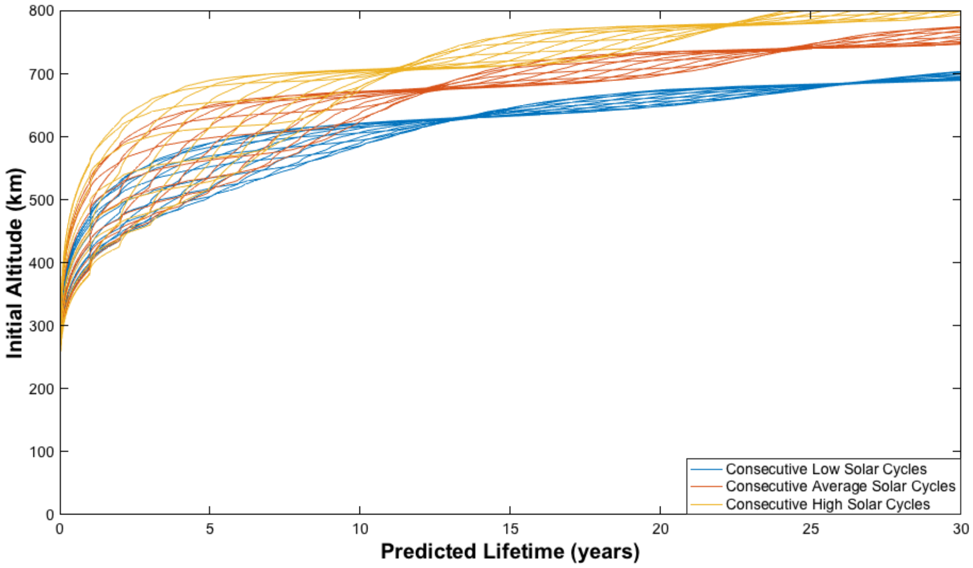

Fig. 6.7 UKube-1 predicted orbital lifetime versus initial altitude with open launch date assuming consecutive low, average and high solar cycles

It is shown in Figure 6.7 that there are points of convergence every 13 years for the group of low cycle curves, and every 12 and 11 years for the average and high cycle groupings, respectively. These points of convergence can be attributed to the cycle period. Thus, when launching to the initial altitudes corresponding to these points of convergence the orbit lifetime predicted will be set regardless of where in the solar cycle the launch occurs. However, the issue with this is that two consecutive solar cycles will never be identical in length and/or strength; this is an idealised case.

6.5 Pre-Launch and Post-Operations Predictions

Two different predictions for the orbit lifetime of UKube-1 can made. Firstly, conservatively, it is assumed the spacecraft is non-operational from the time it is launched, and hence its orbit must decay within 25 years of orbit insertion. Note that UKube-1 did operate following orbit insertion so this analysis is not a true-to-life prediction, however this analysis would have been applicable pre-launch for regulatory assessment purposes. Secondly, since the spacecraft is now inactive and attitude control actions have ceased, it can be assumed that the spacecraft is tumbling randomly.[98] The difference between these predictions will give the benefit to the orbit lifetime from the attitude control.

A maximum allowable altitude prediction is an interesting application of the Modified King-Hele method, and pertinent for documenting compliance with regulatory requirements, however perhaps a more interesting result of the method is the orbit lifetime prediction for UKube-1 given its initial orbit parameters. Given the available data, and the assumptions made herein, it is found that the spacecraft would have de-orbited approximately 13.2 years after orbit insertion.

Once the spacecraft is no longer operational it is assumed that it will begin to tumble randomly, and thus, the ISO standard for average projected area is applied. From Table 6.1 it is known that during the period of operations UKube-1 decreased approximately 9 km in altitude. From orbit tracking data taken when UKube-1 is known to have been inactive, see Table 6.1, a further orbit lifetime prediction is made: with 1σ confidence, UKube-1 will de-orbit in approximately 11.8 years (June 2028). When including the 2.2 years of operations this gives a total lifetime for UKube-1 of 13.9 years; meaning the attitude control gave UKube-1 approximately 8 months of extra time in orbit, this is likely the result of UKube-1 maintaining an attitude with a lower projected area than that given by the ISO standard. The projected decay of UKube-1, from when it is known to be inactive, is shown in Figure 6.8.

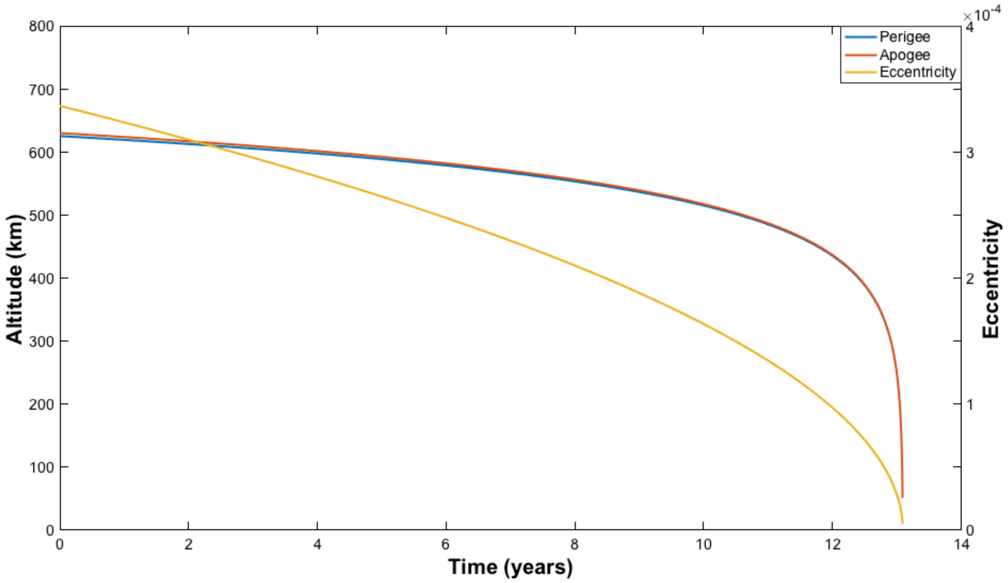

Fig. 6.8 Projected decay of UKube-1

6.6 Applying the Area Averaging Correction Factor

In order to show the effectiveness of the correction factor for the ISO standard developed in chapter 4, the method is demonstrated using the UKube-1 spacecraft as a case study. The new correction factor is applied to the general perturbations solution for low eccentricity orbit lifetime prediction. Conservatively, it is assumed that the spacecraft is non-operational from the time it is launched, and hence its orbit must decay within 25 years of orbit insertion. As previously mentioned, UKube-1 did operate following orbit insertion and hence this analysis is not a true-to-life prediction. However, the prediction here would have been applicable prior to launch for regulatory assessment purposes.

Using UKube-1's launch date, specifications, and the relevant ISO standard[17], as defined in Table 6.1, the average projected area can be calculated and the orbit lifetime can be predicted.

Given the geometry of UKube-1, as seen in Figure 6.9, the average area is calculated using the average projected area method with the viewpoint sphere, the correction factor and the ISO Standard method; the values calculated using of each of these methods are shown in Table 6.2.

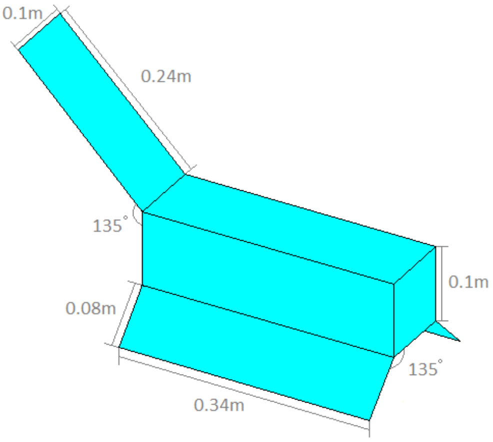

Fig. 6.9 UKube-1 Geometry

Table 6.2 Projected Area of UKube-1

Method	Area (m^2)	% Error
Average Projected Area	0.0683	-
Correction Factor Area	0.0628	-8.09
ISO Standard Area	0.0782	14.48

It can be seen that in this case the correction factor underestimates the projected area while the ISO standard method overestimates it. These areas are then applied to the orbit lifetime prediction and the orbit lifetime predictions attained can be seen in Table 6.3.

Table 6.3 Orbit Lifetime Prediction for UKube-1

Method	Lifetime (years)	% Variation
Average Projected Area	12.2	-
Correction Factor Area	13.2	8.19
ISO Standard Area	10.8	-11.48

It is seen in Table 6.3 that as expected the ISO standard method gives a shorter orbit lifetime than the projected area method. It is also seen that the variation in the orbit lifetime calculation has decreased for the ISO standard method and increased slightly for the curve fit; this is due to the complex nature of the relationship between orbit lifetime and projected area. Therefore, it should be noted that the error in projected area cannot just be assumed to be passed directly through. Instead the standard deviation of the correction factor, as shown in Table 4.2, should be used to inform a Monte Carlo analysis of the orbit lifetime such as that shown in Figure 6.10.

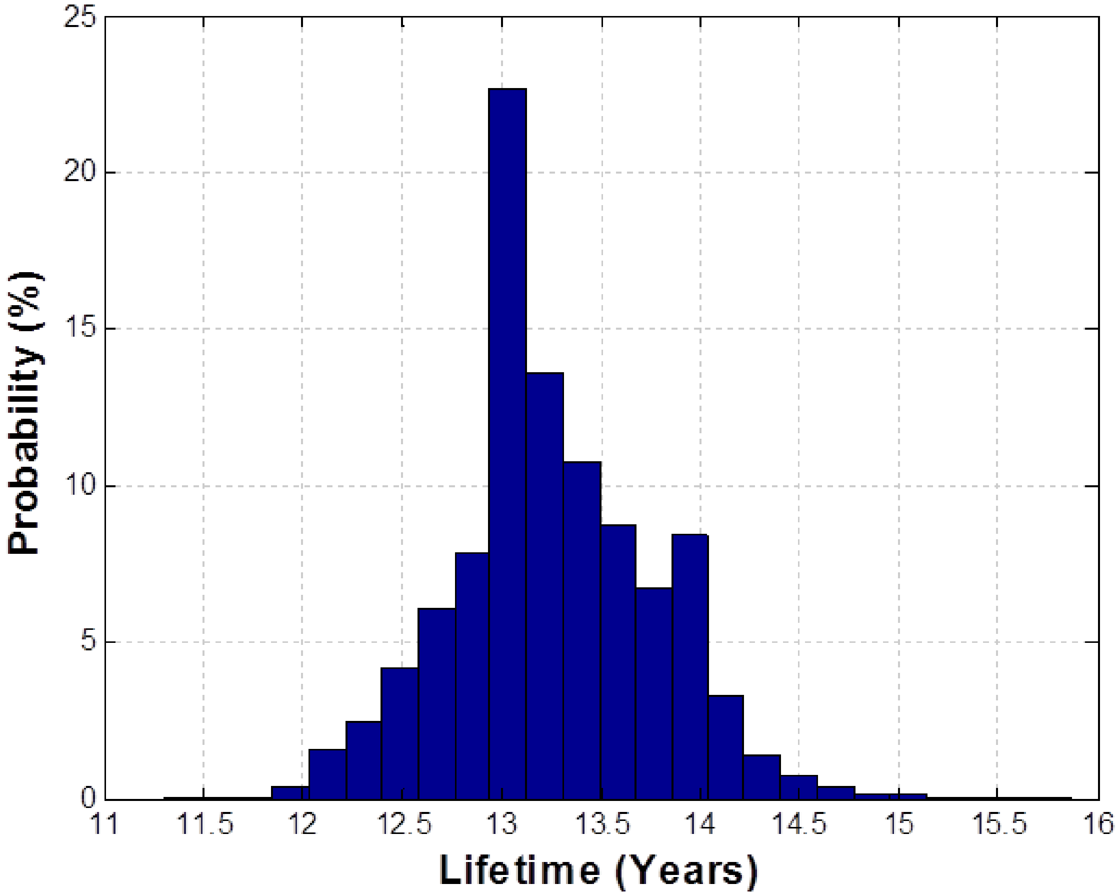

Fig. 6.10 Monte Carlo Analysis of UKube-1 Orbit Lifetime - Probability Distribution Showing Effect of Variation in Projected Area

Figure 6.10 was generated by using a normal distribution, with the mean set as the average projected area calculated for UKube-1 using the correction factor with a variation of approximately ±16% as indicated by the 3 sigma bounds in Table 4.2. The use of the 3 sigma bound means that approximately 99.7% of possible projected areas are captured; therefore there is a 99.7% probability that the actual orbit lifetime will also be captured. The predicted orbit lifetime range produced in this analysis was 11.3-15.9 years, with an average of 13.2 years; the orbit lifetime predicted using the sphere of viewpoints to calculate the average projected area was 12.2 years which falls within this range. Using the 2 sigma (approximately

95% of possible projected areas captured) bound this range becomes 12.0-14.9 years, which also includes the expected lifetime, 12.2 years. However, the use of the more conservative 3 sigma interval is recommended, especially when considering regulatory compliance.

6.7 Refining Re-entry Date Predictions

In order to demonstrate that the method for refining orbit lifetime predictions presented in Chapter 4 and validated in Chapter 5 can be applied with success to other spacecraft, three further missions are used to demonstrate the method's improvement on predictions made by the method prior to refinement. All of the missions discussed here completed an uncontrolled re-entry.

GFZ-1 (COSPAR spacecraft identification 1986-017JE) was a spherical satellite launched in 1995 by GFZ Potsdam to study the Earth's gravity field. After a successful mission it completed an uncontrolled re-entry in June 1999. The spacecraft's initial parameters were: mass approximately 20.63 kg, area approximately 0.0363m^2.[99] As with GOCE the final portion of the spacecraft's re-entry will be studied.

Firstly, the number of data points used is studied. In this case it is clear from Figure 6.11 that using 5 data points would be less advisable; instead using 10 would be more appropriate. The mean percentage error when using 5 data points was 6.97%, while using 10 points this error drops to 5.23%. This suggests that a greater sample of spacecraft is required to make a better recommendation on the number of data points that should be used. It can be seen that as before the percentage error begins a steady rise and therefore it could be recommended again that no more than 30 previous data points should be used.

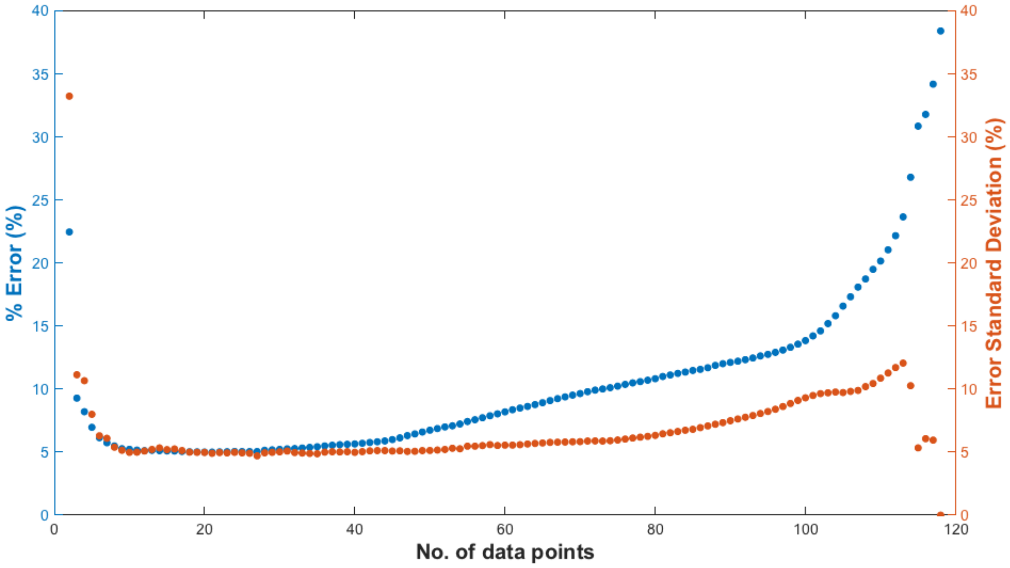

Fig. 6.11 Accuracy comparison when using various numbers of previous decay data points for the GFZ-1 satellite

The accuracy of the updated and original methods can be compared, in this case using the 10 previous data points method. It is seen in Figure 6.12 that the updated method is clearly more accurate than the original method. The mean percentage error in the original method was 20.63% (standard deviation 10.24) compared to 5.23% (standard deviation 4.98) of the updated method.

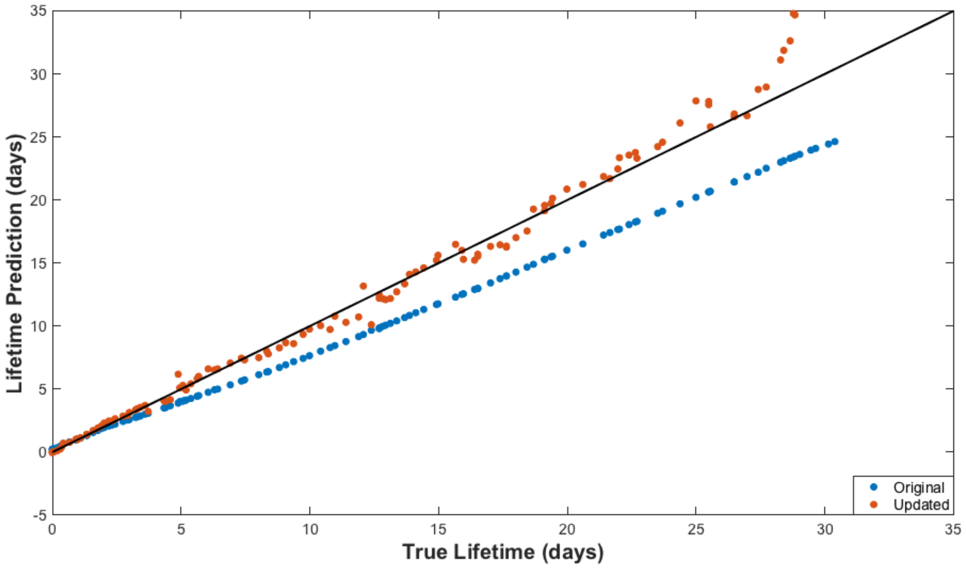

Fig. 6.12 Comparison of Original and Updated Methods Accuracy for the GFZ-1 satellite

Cosmos 1939 (COSPAR spacecraft identification 1988-032A) was the first operational satellite of the Russian/CIS (Commonwealth of Independent States) Resurs-O1 programme. The satellite was launched in 1988 to provide geologic applications including fire detection and ice monitoring. The satellite re-entered at the end of October 2014. The spacecraft's parameters were: mass approximately 1900 kg, area approximately 11m^2. As with GOCE and GFZ-1 the final portion of the spacecraft's re-entry will be studied.

Again the number of data points used is studied. In this case it is clear from Figure 6.13 that using 5 data points would be acceptable, however, using 10 would also be appropriate as with the GFZ-1. The mean percentage error when using 5 data points was 12.98%; using 10 points this error drops slightly to 11.78%. In this case the steady rise in error when using more data points present in the other cases is absent until very late in this spacecraft's lifetime. However, using more data points would bring no material benefit, in fact due to the fact that data points are taken from tracking information, using more data points means the user must wait until these data points become available. Depending on the priorities of the agencies providing tracking data some spacecraft may only be tracked once per day, meaning if a large number of data points is required, it could be months before accurate lifetime estimates can be given. However, as is shown here this is not the case.

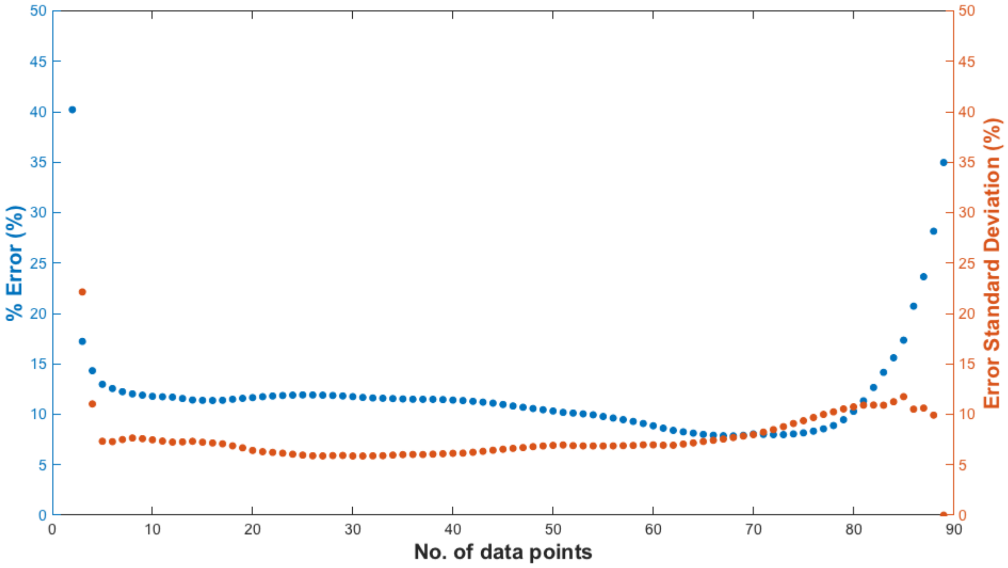

Fig. 6.13 Accuracy comparison when using various numbers of previous decay data points for Cosmos 1939

The accuracy of the updated and original methods can be compared, in this case using the 10 previous data points method. It can be seen in Figure 6.14 that again the updated method is clearly more accurate than the original method. The mean percentage error in the original method was 27.69% (standard deviation 5.53) compared to 11.78% (standard deviation 4.74) of the updated method. Note that the mean percentage error would have been 8.05% using 70 previous data points in the updated method.

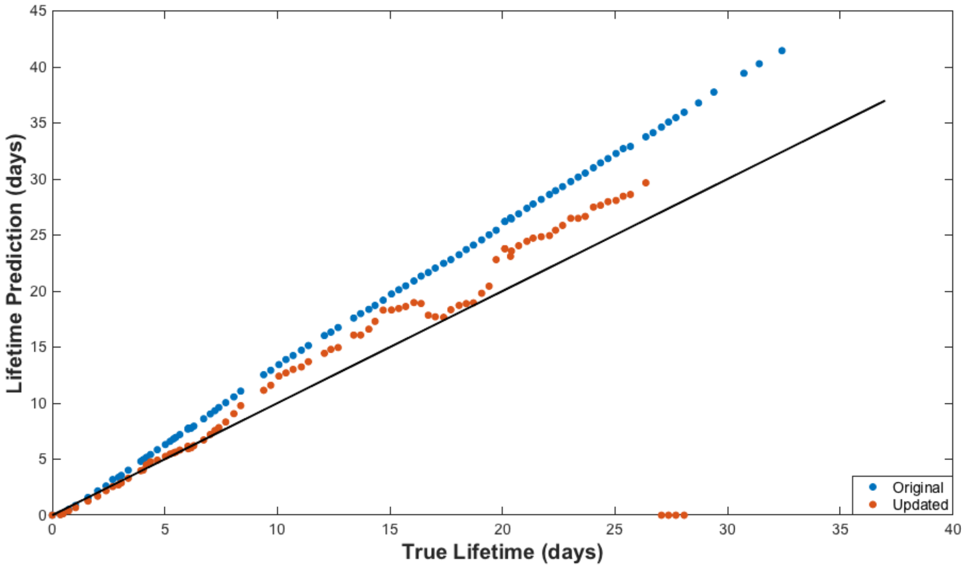

Fig. 6.14 Comparison of Original and Updated Methods Accuracy for Cosmos 1939

UARS , Upper Atmosphere Research Satellite (COSPAR spacecraft identification 1991-063B) was a NASA Earth observation satellite which was officially decommissioned on December 14th 2005, finally re-entering at the end of June 2011. The spacecraft initial parameters were: mass approximately 5668 kg, area approximately 16.6 m^2.[100,101] Again only the final portion of the spacecraft's re-entry will be studied.

As before, the number of data points used is studied. In this case it is clear from Figure 6.15 that again using 5 data points would be advisable. However, using 10 points would also be appropriate as with GFZ-1. The mean percentage error when using 5 data points was 24.59%, while using 10 points this error increases slightly to 25.35%. In this case the steady rise in error when using more data points is present, therefore, again it is recommended that no more than 30 data points be used.

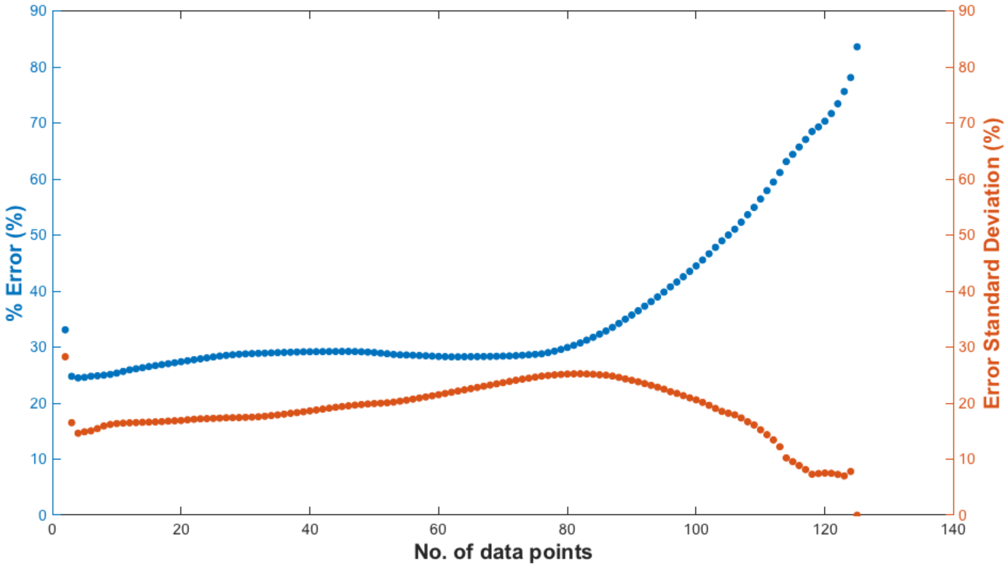

Fig. 6.15 Accuracy comparison when using various numbers of previous decay data points for UARS

The accuracy of the updated and original methods can also be compared, in this case using the 10 previous data points method. It can be seen in Figure 6.16 that again the updated method is clearly more accurate than the original method. The mean percentage error in the original method was 95.40% (standard deviation 35.98) compared to 25.35% (standard deviation 16.35) of the updated method.

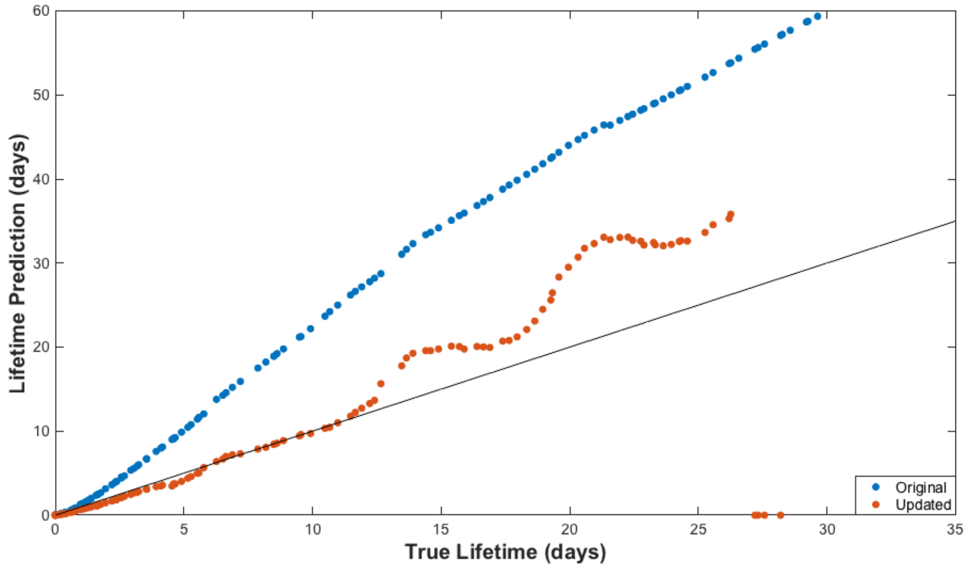

Fig. 6.16 Comparison of Original and Updated Methods Accuracy for UARS

Through these three case studies it is shown that, though further validation is required, the method for refining predictions produces consistently more accurate results than the original method alone. As discussed in Section 4.2 this refinement method decouples the propagation from the mass, drag coefficient and projected area inputs. Therefore, pending further validation, this method is recommended to deal with cases where spacecraft characteristics are uncertain. It is recommended that operators determine the appropriate number of previous data points using 20 previous points, the optimal number found can then be used to predict forward.

6.8 Total Volume Swept over Orbit Lifetime

The simplest metrics available to quantify the risk of a collision occurring are the amount of time an object spends in-orbit, and how large a volume it sweeps through in that time. Note, the term collision risk herein describes the risk of a collision occurring only. The risk that a collision poses to the space environment cannot be modelled without taking into account the circumstances of the collision, this is not considered herein. It is typically assumed that the less time an object is in orbit the lower the collision risk, and as such increasing the area of a spacecraft, by deploying a drag sail for example, will always be beneficial, however as will be shown this assumption is mistaken. In-fact by increasing the area of a spacecraft at the end of its life an operator could be argued at fault, and hence liable for any subsequent in-orbit collision.

The volume swept and orbit lifetime are dependant on the mass and projected area of the spacecraft. Therefore, in order to demonstrate the effect of the variation in mass and projected area, these parameters were allowed to vary between 1 and 1000 kg and 0.01 and 50 m^2 respectively. The resultant volumes swept are shown in Figure 6.17. Note that this analysis was carried out using the spherically-symmetrical, time-invariant atmosphere model with average solar activity developed in Chapter 3, so the effects of solar activity and the diurnal effect are not captured.

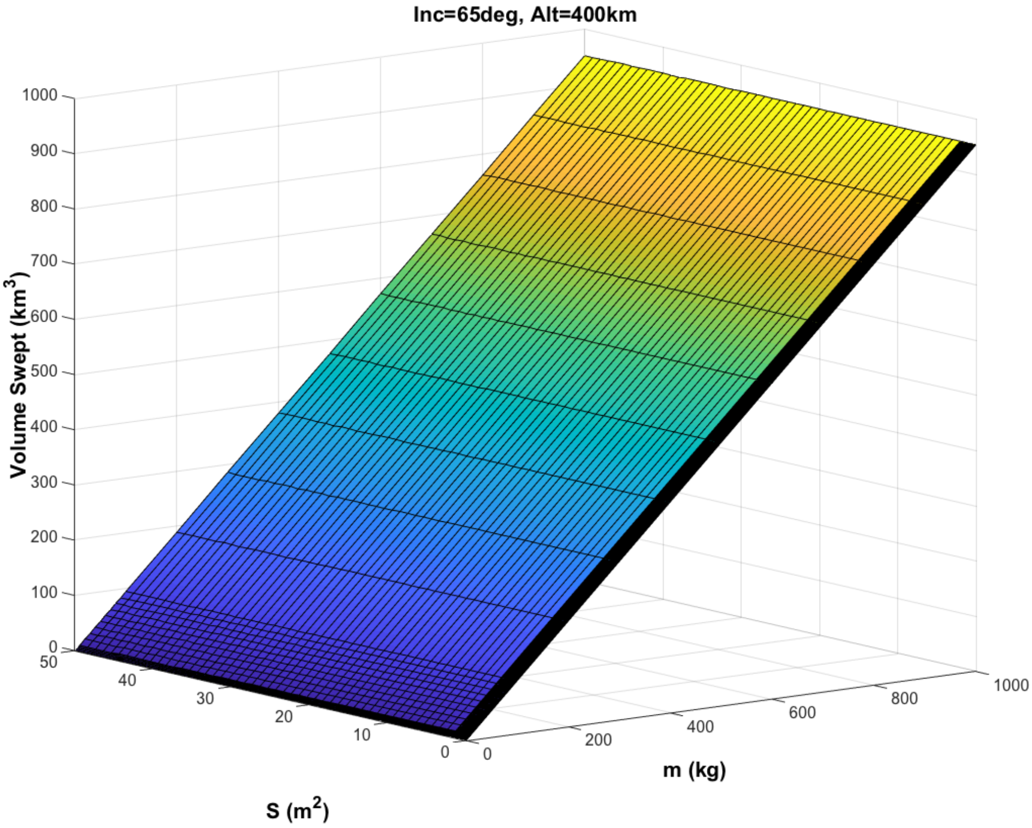

Fig. 6.17 Effect of mass and projected area on total volume swept by a spacecraft over its orbit lifetime

It can be seen from Figure 6.17 that, for a particular orbit, varying the mass for a constant projected area causes a linear increase in the volume swept, however varying the projected area for a constant mass has no effect on the volume swept. This suggests that, as is widely held, if the volume swept and orbit lifetime are used as the measure of collision risk, then any drag augmentation concept would be beneficial in terms of debris mitigation measures as it has zero net impact on the volume swept. However, the Earth's atmosphere is highly dynamic and time-variant, and the effect of time-dependant variations must not be neglected.

Atmospheric density at 100-1000 km altitudes during solar activity maximum can vary by up to two orders of magnitude from the minimum solar activity conditions as was demonstrated in Chapter 3. Including this variation in atmospheric density means that spacecraft orbit lifetime, and hence volume swept become dependent on the date at which de-orbit begins.

To demonstrate the effect of a time varying atmosphere the UKube-1 spacecraft is used as a case study. As of 9 September 2016 UKube-1 has been inactive and thought to be tumbling randomly[98], and hence at end-of-mission. Full parameters as shown in Table 6.1. Two hypothetical cases are also considered, both assuming that UKube-1 has a drag augmentation device of projected area 10 m^2 on-board. The first case assumes this device is deployed immediately at end-of-mission, the second considers what happens when the deployment is delayed in order to coincide with the subsequent period of high solar activity. Note that the analysis is based on an average solar cycle for UKube-1, and thus is independent of its true end-of-mission date.

Table 6.4 details the algorithm followed in order to calculate the volume swept with the 'Delayed Deployment' of a drag augmentation device.

Table 6.4 Algorithm used to calculate the Volume Swept by a drag augmentation device

Step	Algorithm
1	Calculate the orbital lifetime using Equation 2.70 or 2.74 from Chapter 2, as appropriate.
2	Calculate semi-major axis after one revolution using equation 2.55 or 2.60 from Chapter 2, as appropriate.
3	Calculate the distance travelled along the orbital path in that single revolution by approximating it as a closed elliptical orbit, with an average semi-major axis, $a = (a_0 - a_1)/2$.
4	Repeat steps 1-3 until de-orbit is complete, defined herein as an altitude of 65 km.
5	Calculate the sum of the distances calculated in step 3 prior to deployment of drag augmentation device, and multiply that sum by the projected area of the spacecraft alone to attain the total volume swept prior to deployment.
6	Calculate the sum of the distances calculated in step 3 after deployment of drag augmentation device, and multiply that sum by the projected area of the spacecraft with the device deployed to attain the volume swept after deployment.
7	Calculate the total volume swept over the orbit lifetime by summing the volumes swept prior-to and after deployment of drag augmentation device as calculated in steps 5 and 6.

This algorithm can be logically modified for other scenarios discussed in this section. Each of the discussed cases are shown in Figure 6.18, for orbit lifetime, and Figure 6.19, for volume swept during de-orbit. Note the delayed deployment case included here gives the case of the optimal delay time for each time through the solar activity cycle at which de-orbit begins. These optimal delay times are calculated using Monte Carlo analysis, allowing delay time to vary between no delay and one full solar activity cycle.

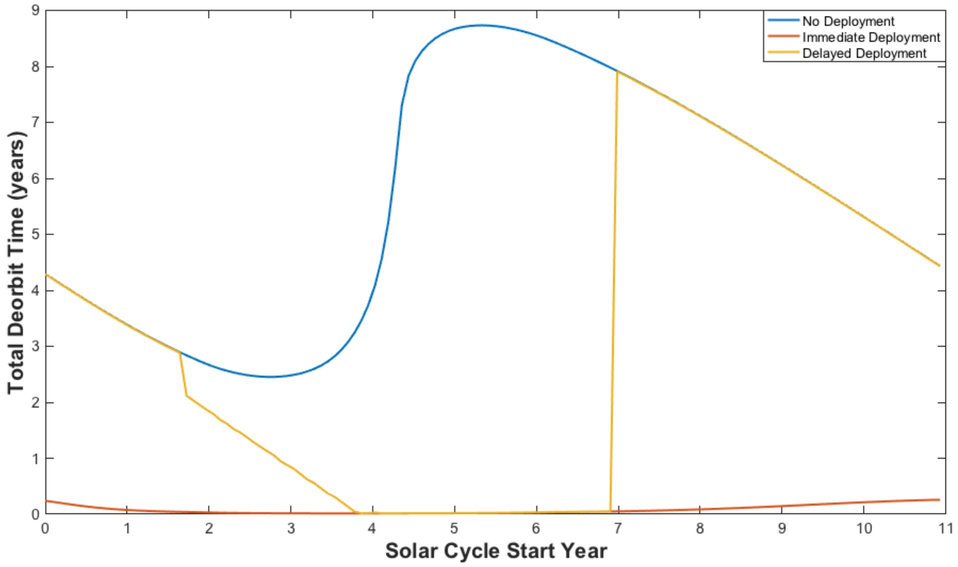

Fig. 6.18 UKube-1 de-orbit lifetime as affected by de-orbit start epoch through solar cycle. Note solar activity cycle start years of 0 and 5 correspond to the solar activity cycle minimum and maximum respectively.

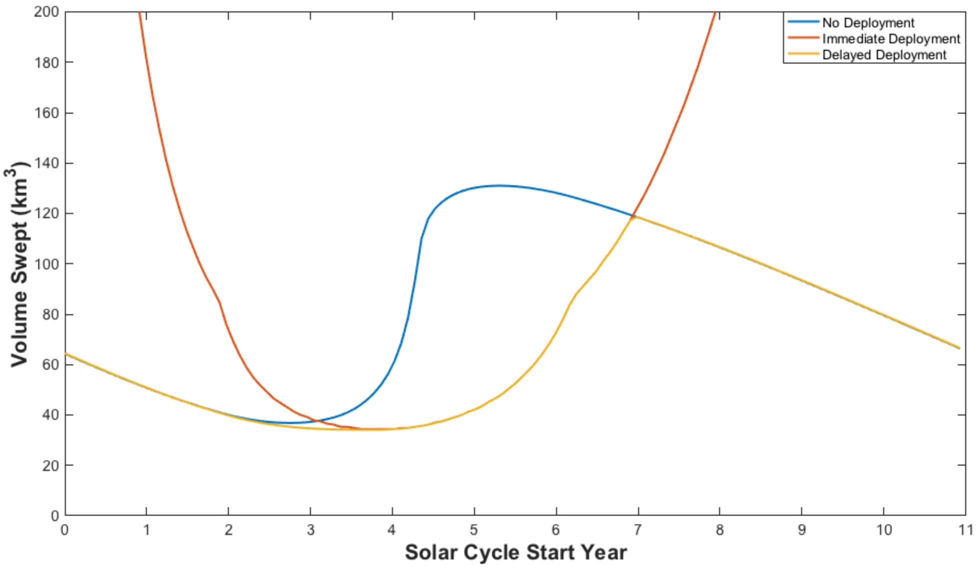

Fig. 6.19 UKube-1 de-orbit volume swept as affected by de-orbit start epoch through solar cycle. Note solar activity cycle start years of 0 and 5 correspond to the solar activity cycle minimum and maximum respectively.

Figures 6.18 and 6.19 show that the date during the solar activity cycle at which de-orbit begins has a large effect on both the de-orbit lifetime and the volume swept during de-orbit. A minimum in both the volume swept and de-orbit lifetime can be seen around 3 - 5 years into the solar activity cycle, just prior to the maximum of the cycle. Figure 6.19 has been truncated in order to highlight the detail; however, in the full figure it could be seen that if deployment occurs at around year 4, the volume swept is an order of magnitude lower than if deployment occurred at the solar activity cycle minimum (year 0). This implies that while orbit lifetime is always reduced, often drastically, by introducing a drag augmentation device, the volume swept is often increased. Drag augmentation should therefore only be used during, or just prior to, the maximum of solar activity cycle. However, end-of-mission cannot always be predicted or guaranteed to coincide with this period. Therefore, when using a drag augmentation device it should be capable of delaying deployment from the end-of-mission and spacecraft decommissioning, to ensure de-orbit coincides with the solar activity cycle maximum. Hence the third case considered, where the spacecraft decays naturally due to atmospheric friction on the spacecraft's projected area alone until the appropriate deployment date, at which time the drag augmentation device is deployed. In comparison to the 'Immediate Deployment' case, except for the period around solar maximum the de-orbit time increases but the volume swept is considerably reduced. It is seen from Figure 6.18 that the de-orbit lifetime of both the immediately deployed and delayed deployed drag augmentation devices decrease or maintain the de-orbit lifetime in comparison to the 'No deployment' case. Thus, it is concluded that delayed deployment is a satisfactory compromise.

There are several major consequences of delayed deployment which must be considered. The first is that by increasing the time to de-orbit the risk of an unplanned break-up is increased. The increased complexity of a system that must remain idle for up to 8 years then assuredly activate and deploy a drag augmentation device will also increase the failure risk rate and/or system complexity, and hence cost, the lack of which are the current attractors of the concept. However, in not implementing the delayed deployment method operators tacitly accept the increase in volume swept and hence the increased collision risk.

In 1947 the United States of America Court of Appeals for the Second Circuit proposed a test to determine the standard of care for the tort of negligence, the first time calculus was used to determine liability. The judgment was written by Judge Learned Hand wherein he described what is now termed the calculus of negligence, or Learned Hand formula, an algebraic formula (B = PL). From this, liability is based on the relation between investment in precaution (B) and the product of the probability (P) and magnitude (L) of resulting harm. Where PL exceeds B, the defendant should be liable, where B is equal to or greater than PL, the defendant should not be held liable. The application of the Learned Hand formula in outer space has not been much discussed, however by increasing the probability of a collision the Learned Hand formula implies a reckless act, in which case spacecraft operators who inappropriately deploy drag augmentation device could be argued liable for any subsequent on-orbit collision.

Of note, the technology demonstration mission CanX-7 is currently in-orbit and deployed a drag sail in May 2017[102], just ahead of a solar minimum, after the end of its operational life. In doing so the operators of CanX-7 have, perhaps unwittingly, increased the in-orbit collision risk of the spacecraft. CanX-7 (COSPAR identification 2016-059F) is a 3U CubeSat (34x10x10 cm) of mass 3.5 kg, with a drag sail of effective area 2 m^2 deployed on 3 May 2017.[102] The initial epoch of the CanX-7 case study is 4 May 2017, when the spacecraft had a semi-major axis of 7059.3238 km, eccentricity of 0.0030913, and inclination of 98.1796°.[102] Once again, the semi-major axis, eccentricity and inclination are taken from orbit tracking data, and as such are specified to the level of detail available. If CanX-7 were randomly tumbling, without the drag sail deployed, its projected area is calculated to be 0.039 m^2.[17] The drag coefficient of the spacecraft is based on the ISO standard for orbit lifetime estimation, giving an assumed drag coefficient of 2.2.[17] Note that the analysis is based on subsequent average solar cycles for CanX-7. Figures 6.20 and 6.21 recreate the analysis completed on UKube-1 for CanX-7, and show the effects of varying the epoch during the solar activity cycle at which de-orbit begins on the de-orbit lifetime and the volume swept during de-orbit.

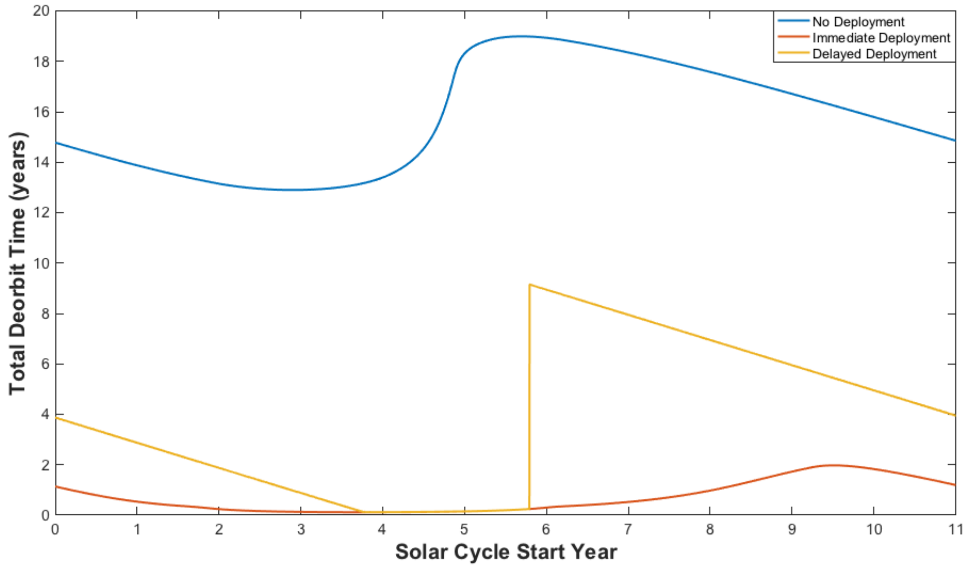

Fig. 6.20 CanX-7 de-orbit lifetime as affected by de-orbit start epoch through solar cycle. Note solar activity cycle start years of 0 and 5 correspond to the solar activity cycle minimum and maximum respectively.

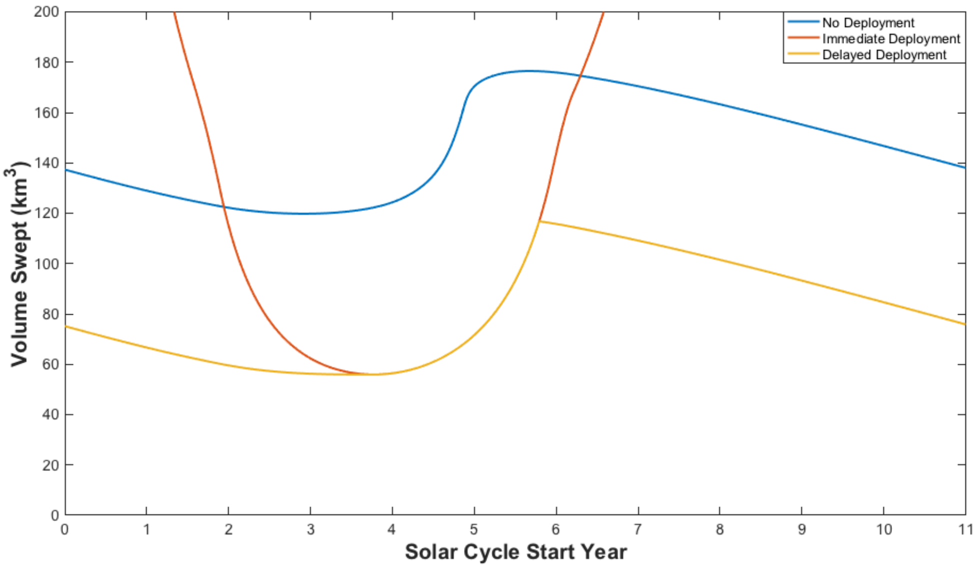

Fig. 6.21 CanX-7 volume swept as affected by de-orbit start epoch through solar cycle. Note solar activity cycle start years of 0 and 5 correspond to the solar activity cycle minimum and maximum respectively.

In comparison to the UKube-1 case study, delayed deployment now shows a marked improvement over the no deployment cases as its duration exceeds a single solar cycle and therefore the delayed deployment provides a much shorter lifetime, and as such a resultant smaller volume swept. CanX-7 deployed its drag sail at an inopportune moment, in a non-truncated version of Figure 6.21 it could be seen that deployment on 3 May 2017 produces an estimated volume swept of approximately 605 km^3 in comparison to the approximately 160 km^3 or 98 km^3 produced in the no deployment and delayed deployment cases respectively for that date. Ideally, the operators of CanX-7 would have delayed its deployment for around 6.5 years, deploying during November 2023.

It is important to note that the strategy of delayed deployment is only effective if the drag augmentation device is of sufficient size to cause the spacecraft to de-orbit over one solar activity maximum period, the device may therefore have to be larger than would be required to de-orbit over the minimum required period of 25 years given by the debris mitigation guidelines. Finally, one unquantifiable risk is that by delaying deployment, and therefore increasing time in-orbit, an increased in-orbit population could be encountered at the time of deployment. Thus, the collision risk would also be increased. However, there is no way to accurately predict future populations and therefore it is prudent to base decisions on current data. Taking these conclusions into account employing drag augmentation becomes a less attractive concept than previously thought.

Chapter 7

Summary, Conclusions and Future Work

This thesis has addressed the development of accurate general perturbations methods for orbit propagation. In Chapter 1 an introduction to orbit propagation and in particular general perturbations mehods was given. Chapter 2 re-derived a well-known general perturbations method using modern mathematical toolsets, removing some of the assumptions made in the original derivation. Chapter 3 and 4 then addressed the atmospheric density and ballistic coefficient inputs to the orbit propagation method. Chapter 5 dealt with the validation of the methods developed in Chapters 2-4. Finally, Chapter 6 introduced some of the possible applications of the developed methods.

7.1 Conclusions

A single independent variable per solar cycle can be used to relate solar activity levels across a solar cycle. It is thereafter possible to incorporate solar activity into general perturbations solutions using a newly introduced parameter termed the density index, as shown in Chapter 3. Doing so significantly improves the accuracy of the established solution. Furthermore, it is shown that simplifications, for example removing high-order eccentricity terms, made in the derivation of a well-known method for orbit lifetime prediction can be removed and the accuracy of the analysis improved. The method presented in Chapter 2 including the spherically-symmetrical atmospheric density and solar activity models presented in Chapter 3 compares favourably against other analytical methods and third party tools, producing a significantly lower average error. Notably, the leading software packages examined, STK and STELA, produced predictions with higher average errors of 11.39% and 6.63% respectively, compared to 3.46% with the method presented in Chapter 2.

The inclusion of a non-spherically-symmetrical atmosphere model developed in Chapter 3 is shown in Chapter 5 to produce up to approximately 10% variations in the orbit lifetime predictions made for a sun-synchronous satellite. Therefore, when dealing with sun-synchronous satellites it is important that the diurnal variation be considered. However, the approximately 45% improvement made by including the solar activity model is more critical to generating accurate results.

The ISO standard has been shown in Chapter 4 to consistently overestimate the average projected area when considering non-cuboid spacecraft configurations. This means that when applied to an orbit propagation model it will consistently underestimate the orbit lifetime. However, it has also been shown in Chapter 6 that by the addition of a correction factor the ISO standard method can be used to produce a reliable estimate of the average projected area of a tumbling CubeSat.

Increased accuracy can be achieved by using spacecraft decay tracking data to inform the input parameters used in orbit lifetime predictions. The method presented herein is not affected by errors in the input parameters, as it derives these from the spacecraft decay tracking data.

The improvement in accuracy made through the application of the methods developed in Chapters 2-4 enables the use of general perturbations methods in areas such as initial mission design and regulatory compliance with confidence. However, the individual components may themselves have more wide ranging applications, in areas such as atmospheric or solar radiation modelling.

7.2 Future Work

Chapter 5 contains the initial validation study for the methods developed, however, it is by no means an exhaustive study, further validation could be completed using a larger range of spacecraft or missions for example.

The general perturbations method developed in Chapter 2 focusses on low eccentricity and circular orbits. By extending the method to higher eccentricities it could be used to propagate the orbits of spacecraft in a much wider range of orbits, such as geostationary transfer orbits. The extension to higher eccentricities was considered for inclusion herein. However, after the derivation of the method was completed, the initial results produced were so poor that the assumptions made in derivation of the method were found to be flawed. As such, the method derived was found to be inapplicable to higher eccentricity orbits and was, therefore, abandoned. In order to apply general perturbation methods to higher eccentricity orbits a new derivation method is required.

The solar activity model derived in Chapter 3 was shown in Chapter 5 to produce good results in the context of orbit lifetime analysis. The model was built using monthly averaged solar activity data. The monthly data was chosen due to convenience and ease of access to the data set. A study could be completed to demonstrate the effect of deriving the model from daily or yearly data on the final curve fit for each solar cycle. Furthermore, the geomagnetic index could be modelled in a similar manner in order to capture the effects of geomagnetic storms on atmospheric density. The addition of geomagnetic storm data would be particularly important when considering short-term orbit propagation where short-term spikes in solar and geomagnetic indices do not average out as they do in long-term propagations.

In Chapter 3 the diurnal effect is used to build the non-spherically-symmetrical atmospheric density model, future work could extend this work by including effects such as the semi-annual variation. Furthermore, and perhaps more significantly, it was shown in Chapter 5 that the difference in orbit lifetime predictions made using the spherically-symmetrical model derived from the CIRA density data as opposed to the spherically-symmetrical model derived from the NRLMSISE density data accounts for a difference of approximately 247 days, which is nearly a third of the orbit lifetime. The CIRA based model has been shown in Chapter 5 to produce reliable orbit lifetime estimations, therefore it is concluded that the sample data set from NRLMSISE used to build the diurnally varying atmospheric model is not representative and should be expanded. It is expected that when including a larger data set, the effect of the diurnal variation on the mean density will remain as it is shown in this dissertation; however the mean density is expected to shift to be more comparable to the mean density given by the CIRA based model.

The area averaging method derived in Chapter 4 could be further extended to consider larger and more complex spacecraft. It would, however, require the development of a large database of satellite structures. Furthermore, the ISO standard correction factor for CubeSats derived in Chapter 4 should be validated fully using historical data.

The one orbit propagation input parameter not considered independently is the drag coefficient. Further study could produce a model of it to replace the 2.2 ISO standard assumption. This would be of particular interest to atmospheric scientists who study the decay of satellite orbits as indicators of the composition of the atmosphere. An independent drag coefficient model allows separation of uncertainties in the input parameters when deriving atmospheric density from the evolution of spacecraft orbits. Many factors affect the drag coefficient including, but not limited to, the shape of the object, the surface properties of the object, and the properties of the fluid through which the object travels. Problems with drag coefficient estimation arise from each of these. The objects shape, being convex or concave affects the way the fluid travels over or is reflected off of the object, in the case of concave objects the affect of secondary reflections must also be considered. The surface properties will also play a part in these interactions, some surfaces will absorb particles, some reflect, the degree of absorption or reflection will alter the surface and consequently the drag coefficient.

Four case studies were presented in Chapters 5 and 6 demonstrating the use of decay data to inform re-entry predictions. This does not constitute a full validation study, it is therefore recommended that a more complete study should be conducted.

References

[1] University Corporation for Atmospheric Research. Next solar max: Doozy or dud?, 2006.

[2] Space Weather Canada. Monthly averages of Solar 10.7 cm flux, 2017.

[3] NASA. Yearly Averaged Sunspot Numbers 1610-2007, 2008.

[4] United Nations Committee on the Peaceful Uses of Outer Space Legal Subcommittee. Treaty on principles governing the activities of states in the exploration and use of outer space, including the moon and other celestial bodies, 1967. http://www.unoosa.org/oosa/en/ourwork/spacelaw/treaties/introouterspacetreaty.html.

[5] United Nations Committee on the Peaceful Uses of Outer Space Legal Subcommittee. Status of International Agreements relating to activities in outer space as at 1 January 2013, 2013.

[6] United Nations Committee on the Peaceful Uses of Outer Space Legal Subcommittee. Agreement on the rescue of astronauts, the return of astronauts and the return of objects launched into outer space, 1967. http://www.unoosa.org/oosa/en/ourwork/spacelaw/treaties/introrescueagreement.html.

[7] United Nations Committee on the Peaceful Uses of Outer Space Legal Subcommittee. Convention on international liability for damage caused by space objects, 1971. http://www.unoosa.org/oosa/en/ourwork/spacelaw/treaties/introliability-convention.html.

[8] United Nations Committee on the Peaceful Uses of Outer Space Legal Subcommittee. Convention on registration of objects launched into outer space, 1974. http://www.unoosa.org/oosa/en/ourwork/spacelaw/treaties/introregistration-convention.html.

[9] United Nations Committee on the Peaceful Uses of Outer Space Legal Subcommittee. Agreement governing the activities of states on the moon and other celestial bodies, 1979. http://www.unoosa.org/oosa/en/ourwork/spacelaw/treaties/intromoon-agreement.html.

[10] Gravity.

[11] T.H. Karakoç, C.O. Colpan, and Y. Şöhret. *Advances in Sustainable Aviation*. Springer International Publishing, 2017.

[12] T. S. Kelso. CelesTrak NORAD Two-Line Element Sets Historical Archives, 1985.

[13] United States Congress. U.s. commercial space launch competitiveness act, 2015. https://www.congress.gov/bill/114th-congress/house-bill/2262.

[14] Lucien Rapp, Denis Lacoste, V. Dos Santos Paulino, and Maria Rhimbassen. Space LegalTech, 2017.

[15] Inter-Agency Space Debris Coordination Committee. IADC-02-01 Space Debris Mitigation Guidelines (Revision 1), 2007.

[16] International Organization for Standardization. ISO 24113:2011 Space systems - Space debris mitigation requirements. Technical report, 2011.

[17] International Organization for Standardization. ISO 27852:2010(E): Space systems - Estimation of orbit lifetime. Technical Report 60, 2010.

[18] Daniel L Oltrogge and Chia-chun Chao. Standardized Approaches for Estimating Orbit Lifetime after End-of-Life. In *AAS/AIAA Astrodynamics Conference*, Mackinac Island, MI, 2007.

[19] David A. Vallado and Wayne D. McClain. *Fundamentals of Astrodynamics and Applications*. McGraw-Hill Inc., space tech edition, 1997.

[20] Malcolm Macdonald and Viorel Badescu, editors. *The International Handbook of Space Technology*. Springer-Verlag Berlin Heidelberg, 2014.

[21] Bo J. Naasz, Kevin Berry, and Kenneth Schatten. Orbit Decay Prediction Sensitivity to Solar Flux Variations. In *2007 AIAA/AAS Astrodynamics Specialist Conference*, number 301, Mackinac Island, MI, 2007.

[22] David A. Vallado and David Finkleman. A critical assessment of satellite drag and atmospheric density modeling. *Acta Astronautica*, 95(1):141–165, 2014.

[23] D.G. King-Hele. *Satellite Orbits in an Atmosphere: Theory and Application*. Blackie and Son Ltd, Glasgow, 1987.

[24] G. E. Cook, D. G. King-Hele, and Doreen M. C. Walker. The Contraction of Satellite Orbits under the influence of Air Drag I. With Sphericallly Symmetical Atmosphere. *Proceedings of the Royal Society A: Mathematical, Physical and Engineering Sciences*, 257(1289):224–249, 1960.

[25] G. G. Swinerd and W. J. Boulton. Contraction of Satellite Orbits in an Oblate Atmosphere with a Diurnal Density Variation. *Proceedings of the Royal Society A: Mathematical, Physical and Engineering Sciences*, 383(1784):127–145, September 1982.

[26] Michael D. Griffin and James R. French. *Space Vehicle Design*. American Institute of Aeronautics and Astronautics, Inc., Reston, VA, 2nd edition, 2004.

[27] R. K. Sharma. Analytical approach using KS elements to near-Earth orbit predictions including drag. *Proceedings of the Royal Society A: Mathematical, Physical and Engineering Sciences*, 433(1887):121–130, 1991.

[28] R. K. Sharma. A third-order theory for the effect of drag on Earth satellite orbits. *Proceedings of the Royal Society A: Mathematical, Physical and Engineering Sciences*, 438(1904):467–475, 1992.

[29] R. K. Sharma. Contraction of satellite orbits using KS elements in an oblate diurnally varying atmosphere. *Proceedings of the Royal Society A: Mathematical, Physical and Engineering Sciences*, 453(1966):2353–2368, November 1997.

[30] R. K. Sharma. Contraction of high eccentricity satellite orbits using K-S elements with air drag. *Proceedings of the Royal Society A: Mathematical, Physical and Engineering Sciences*, 454(1974):1681–1689, 1998.

[31] Vladimir Martinusi, Lamberto Dell'Elce, and Gaëtan Kerschen. Analytic propagation of near-circular satellite orbits in the atmosphere of an oblate planet. *Celestial Mechanics and Dynamical Astronomy*, 123(1):85–103, 2015.

[32] Vladimir Martinusi, Lamberto Dell'Elce, and Gaëtan Kerschen. First-order analytic propagation of satellites in the exponential atmosphere of an oblate planet. *Celestial Mechanics and Dynamical Astronomy*, 127(4):451–476, 2017.

[33] G. E. Cook, D. G. King-Hele, and Doreen M. C Walker. The Contraction of Satellite Orbits Under the Influence of Air Drag II. With Oblate Atmosphere. *Proceedings of the Royal Society A: Mathematical, Physical and Engineering Sciences*, 264(1316):88–121, 1961.

[34] D. G. King-Hele. The Contraction of Satellite Orbits Under the Influence of Air Drag III. High-Eccentricity Orbits. *Proceedings of the Royal Society A: Mathematical, Physical and Engineering Sciences*, 267(1331):541–557, 1962.

[35] G. E. Cook and D. G. King-Hele. The Contraction of Satellite Orbits Under the Influence of Air Drag IV. With scale height dependant on altitude. *Proceedings of the Royal Society A: Mathematical, Physical and Engineering Sciences*, 275(1362):357–390, 1963.

[36] G E Cook and D G King-Hele. The Contraction of Satellite Orbits under the Influence of Air Drag V. with Day-To-Night Variation in Air Density. *Philosophical Transactions of the Royal Society of London A: Mathematical, Physical and Engineering Sciences*, 259(1096):33–67, December 1965.

[37] G. E. Cook and D. G. King-Hele. The Contraction of Satellite Orbits Under the Influence of Air Drag VI. Near-Circular Orbits with Day-to-Night Variation in Air Density. *Proceedings of the Royal Society A: Mathematical, Physical and Engineering Sciences*, 303(1472):17–35, 1968.

[38] D. G. King-Hele and Doreen M. C. Walker. The Contraction of Satellite Orbits under the Influence of Air Drag VII. Orbits of high eccentricity, with scale height dependent on altitude. *Proceedings of the Royal Society A: Mathematical, Physical and Engineering Sciences*, 411(1840):1–17, 1987.

[39] D. G. King-Hele and Doreen M. C. Walker. The Contraction of Satellite Orbits Under the Influence of Air Drag VIII. Orbital lifetime in an oblate atmosphere, when perigee distance is perturbed by odd zonal harmonics in the geopotential. *Proceedings of the Royal Society A: Mathematical, Physical and Engineering Sciences*, 414(1847):271–295, 1987.

[40] High-order averaging of eccentric artificial satellites perturbed by the Earth's potential and air-drag terms. *Proceedings of the Royal Society A: Mathematical, Physical and Engineering Sciences*, 459(2034):1517–1534, June 2003.

[41] E. Titov, J. Burt, and E. Josyula. Satellite Drag Uncertainties Associated with Atmospheric Parameter Variations at Low Earth Orbits. *Journal of Spacecraft and Rockets*, 51(3):884–892, May 2014.

[42] D. G. King-Hele and D. M. C. Walker. Technical Report 87030: The Prediction of Satellite Lifetimes. Technical report, Royal Aircraft Establishment, Ministry of Defence, Farnborough, 1987.

[43] Kenneth Schatten. Solar activity and the solar cycle. *Advances in Space Research*, 32(4):451–460, August 2003.

[44] Kenneth Schatten. Long-Range Solar Activity Predictions: A Reprieve From Cycle #24's Activity. In *Flight Mechanics Symposium*, Greenbelt, MD, USA, 2003. NASA Goddard Space Flight Center.

[45] Kenneth Schatten. Fair space weather for solar cycle 24. *Geophysical Research Letters*, 32(21), 2005.

[46] Kenneth Schatten and W Dean Pesnell. Solar cycle #24 and The Solar Dynamo. In *20th International Symposium on Space Dynamics*, Annapolis, MD, USA, 2007. NASA Goddard Space Flight Center, NASA Goddard Space Flight Center.

[47] John Q. Stewart and H. A. A. Panofsky. The Mathematical Characteristics of Sunspot Variations. *The Astrophysical Journal*, 88(4):385–407, 1938.

[48] W. Elling and H. Schwentek. Fitting the sunspot cycles 10-21 by a modified f-distribution density function. *Solar Physics*, 137(1):155–165, 1992.

[49] David H Hathaway, Robert M Wilson, and Edwin J Reichmann. The Shape of The Sunspot Cycle. *Solar Physics*, 151(1):177–190, 1994.

[50] Ohad Ben-Yaacov, Eviatar Edlerman, and Pini Gurfil. Analytical technique for satellite projected cross-sectional area calculation. *Advances in Space Research*, 56(2):205–217, July 2015.

[51] Martin Langer and Jasper Bouwmeester. Reliability of cubesats–statistical data, developers' beliefs and the way forward. In *Proceedings of the 30th Annual AIAA/USU Conference on Small Satellites*, 2016.

[52] Emma Kerr and Malcolm Macdonald. Incorporating Solar Activity into General Perturbation Analysis of Atmospheric Friction. *Journal of Guidance, Control, and Dynamics*, 41(6):1320–1336, jun 2018.

[53] Daniel KL Oi, Alex Ling, Giuseppe Vallone, Paolo Villoresi, Steve Greenland, Emma Kerr, Malcolm Macdonald, Harald Weinfurter, Hans Kuiper, Edoardo Charbon, and Rupert Ursin. Cubesat quantum communications mission. *EPJ Quantum Technology*, 4(1):6, 2017.

[54] Emma Kerr, Malcolm Macdonald, and Philipp Voigt. Taxonomy and Analysis of Issues Facing Post Mission Disposal Concept. In *68th International Astronautical Congress*, Adelaide, Australia, 2017.

[55] Emma Kerr and Malcolm Macdonald. General Perturbations Method for Orbit Lifetime Analysis Incorporating Non-Spherically-Symmetrical Atmospheres. In *AIAA/AAS Astrodynamics Specialist Conference*, Long Beach, CA, USA, 2016. American Institute of Aeronautics and Astronautics.

[56] Emma Kerr and Malcolm Macdonald. Improving the Accuracy of Orbit Lifetime Analysis using Enhanced General Perturbation Methods. In *26th AAS/AIAA Space Flight Mechanics Meeting*, Napa, CA, USA, 2016.

[57] Ciara McGrath, Emma Kerr, and Malcolm Macdonald. An analytical low-cost deployment strategy for satellite constellations. 2015.

[58] Emma Kerr and Malcolm Macdonald. Improving the Accuracy of General Perturbations Methods for Spacecraft Lifetime Analysis. In *66th International Astronautical Congress*, Jerusalem, Isreal, 2015.

[59] Emma Kerr and Malcolm Macdonald. A General Perturbations Method For Spacecraft Lifetime Analysis. In *25th AAS/AIAA Space Flight Mechanics Meeting*, Wiliamsburg, VA, USA, 2015.

[60] A.E. Roy. *Orbital Motion, Fourth Edition*. CRC Press, 2004.

[61] R.R. Bate, D.D. Mueller, and J.E. White. *Fundamentals of Astrodynamics*. Dover Books on Aeronautical Engineering Series. Dover Publications, 1971.

[62] NASA, NOAA, and US Air Force. U.S. Standard Atmosphere, 1976. Technical report, Washington, D.C., 1976.

[63] L. G. Jacchia. Thermospheric Temperature, Density, and Composition: New Models. *SAO Special Report #375*, 1977.

[64] MSISE-90 Model of Earth's Upper Atmosphere.

[65] Naval Research Laboratory. NRLMSISE-00 Atmosphere Model [online database].

[66] J. M. Picone, A. E. Hedin, D. P. Drob, and A. C. Aikin. NRLMSISE-00 empirical model of the atmosphere: Statistical comparisons and scientific issues. *Journal of Geophysical Research: Space Physics*, 107(A12):SIA 15–1–SIA 15–16, dec 2002.

[67] C. G. Justus and F. W. Leslie. The NASA MSFC Earth Global Reference Atmospheric Model—2007 Version. Technical report, 2008.

[68] Fred W. Leslie and C. G. Justus. Earth Global Reference Atmosperic Model 2007 (EARTH-GRAM07) Applications for the NASA Constellation Program. Technical Report 1983, NASA Marshall Flight Center, 2007.

[69] Bruce R. Bowman and W. Kent Tobiska. JB2008: The Jacchia-Bowman 2008 Empirical Thermospheric Density Model.

[70] Bruce R Bowman, W Kent Tobiska, Frank A Marcos, Cheryl Y Huang, Chin S Lin, and William J Burke. A New Empirical Thermospheric Density Model JB2008 Using New Solar and Geomagnetic Indices.

[71] S. Bruinsma, G. Thuillier, and F. Barlier. The DTM-2000 empirical thermosphere model with new data assimilation and constraints at lower boundary: accuracy and properties. *Journal of Atmospheric and Solar-Terrestrial Physics*, 65(9):1053–1070, 2003.

[72] Commitee on Space Research. COSPAR International Reference Atmosphere - 2012. Technical report, 2012.

[73] Malcolm Macdonald, Colin McInnes, Charlotte Bewick, Lourens Visagie, Vaios Lappas, and Sven Erb. Needs Assessment of Gossamer Structures in Communications Platform End-of-Life Disposal. In *AIAA Guidance, Navigation and Control Conference*, Boston, Massachusettes, USA, 2013.

[74] H. W. Babcock. The Topology of the Sun's Magnetic Field and the 22-year Cycle. *Astrophysical Journal*, 133, 1961.

[75] Mausumi Dikpati and Peter A. Gilman. Simulating and Predicting Solar Cycles Using a Flux Transport Dynamo. *The Astrophysical Journal*, 649(1):498–514, September 2006.

[76] K. F. Tapping and D. P. Charrois. Limits to the accuracy of the 10.7 cm flux. *Solar Physics*, 150(1-2):305–315, mar 1994.

[77] E. W. Maunder. Note on the sun-spots of 1889. *Monthly Notices of the Royal Astronomical Society*, 50(6):361–372, 1890.

[78] E. W. Maunder. Note on the sun-spots of 1888. *Monthly Notices of the Royal Astronomical Society*, 51(1):23–27, 1890.

[79] E. W. Maunder. Note on the spot-group of 1890 august 25–september 5. *Monthly Notices of the Royal Astronomical Society*, 51(1):27–31, 1890.

[80] E. W. Maunder. A prolonged sunspot minimum. *Knowledge: An Illustrated Magazine of Science*, 17:173–176, August 1894.

[81] John A. Eddy. The Maunder Minimum. *Science*, 192(4245):1189–1202, 1976.

[82] W. Schröder. On the Existence of the 11-Year Cycle in Solar and Auroral Activity before and during the So-Called Maunder Minimum. *Journal of Geomagnetism and Geoelectricity*, 44:119–128, 1992.

[83] W. D. Compton and C. D. Benson. *Living and working in space. A history of Skylab*. United States Government, Washington D.C., 1983.

[84] K.O. Niehuss, H.C. Euler Jr., and W.W. Vaughan. Statistical Technique for Intermediate and Long-Range Estimation of 13-Month Smoothed Solar Flux and Geomagnetic Index. Technical report, NASA - Technical Memorandum 4759, 1996.

[85] David H Hathaway, Robert M Wilson, and Edwin J Reichmann. A synthesis of solar cycle prediction techniques. *Journal of Geophysical Research*, 104(A10):22375–22388, 1999.

[86] A. I. Ohl and G. I. Ohl. A mew method of very long-term prediction of solar activity. In Richard F. Donnelly, editor, *Solar-Terrestrial Predictions Proceedings*, volume 2, pages 258–263, Boulder, Colorado, USA, 1979. Space Environment Laboratory.

[87] Max Waldmeier. Neue Eigenschaften der Sonnenfleckenkruve. *Astronomische Mitteilungen der Eidgenossischen Sternwarte Zurich*, 14(133):105–136, 1935.

[88] Mausumi Dikpati, Peter A. Gilman, and Giuliana De Toma. Tha Waldmeier Effect: An Artifact of the Definition of Wolf Sunspot Number. *The Astrophysical Journal*, 673(1):99–101, 2008.

[89] C C Chao, J R Wilson, J P Mcvey, and R L Walterscheid. Helium Discrepancy in the NRLMSISE-2000 Density Model Detected Via CHAMP/GRACE Data and Decaying Sphere. In *25th AAS/AIAA Space Flight Mechanics Meeting*, pages 1–18, Wiliamsburg, VA, USA, 2015.

[90] Bruce R Bowman and Kenneth Moe. Drag Coefficient Variability at 175-500 km from the Orbit Decay Analyses of Spheres. In *AAS/AIAA Astrodynamics Conference*, pages 117–136, South Lake Tahoe, California, 2005.

[91] Yalong Qi, Huijun Li, Jie Xiang, and Haijun Man. Periodic Variations of Drag Coefficient for the ANDE Spherical Satellites During its Lifetime. *Chinese Journal of Space Science*, 33(5):525–531, 2013.

[92] AGI. Systems Tool Kit, 2014.

[93] A-A L C. Cojuangco. *Orbital Lifetime Analyses of Pico- and Nano-Satellites*. Mechanical engineering, University of Florida, 2007.

[94] NASA. General Mission Analysis Tool, 2016.

[95] CNES. Semi-analytic Tool for End of Life Analysis, 2016.

[96] Mark R. Drinkwater, R. Haagmans, D. Muzi, A. Popescu, R. Floberghagen, M. Kern, and M. Fehringer. The GOCE Gravity Mission: ESA's First Core Earth Explorer. In *Proceedings of the 3rd International GOCE User Workshop*, Frascati, Italy, 2007.

[97] ECSS Requirements & Standards Devision. Space Product Assurance: Safety 3.1.9. Technical Report April, ESA-ESTEC, Noordwijk, 1996.

[98] Helen Walker. Ukube-1: operations and lessons learned. In *8th European CubeSat Symposium*, London, 2016.

[99] Rolf König, Peter Schwintzer, Albert Bode, and Christoph Reigber. GFZ-1: A small laser satellite mission for gravity field model improvement. *Geophysical Research Letters*, 23(22):3143–3146, November 1996.

[100] Carmen Pardini and Luciano Anselmo. Reentry Predictions of Three Massive Uncontrolled Spacecraft. In *Proceedings of the 23rd International Symposium of Space Flight Dynamics*, Pasadena, CA, USA, 2012.

[101] Carl A. Reber. The upper atmosphere research satellite (UARS). *Geophysical Research Letters*, 20(12):1215–1218, June 1993.

[102] Brad Cotten, Ian Bennett, and Robert E Zee. On-Orbit Results from the CanX-7 Drag Sail Deorbit Mission. 1(416):1–8, 2016.

Appendix A

CIRA Derived Density Model Coefficients

Table A.1 Coefficients for equation 3.2 derived using CIRA data

Altitude Range	Low Solar Activity $F_{10.7} = 70$ SFU		Moderate Solar Activity $F_{10.7} = 140$ SFU		High Solar Activity $F_{10.7} = 230$ SFU	
	A	B	A	B	A	B
100-900 km	4.8108354387E+18	-8.4316024345	4.0353801836E+16	-7.3287675685	1.6560406874E+14	-6.2297870621

Table A.2 Coefficients for equation 3.2 derived using CIRA data

Altitude Range	Low Solar Activity $F_{10.7} = 70$ SFU		Moderate Solar Activity $F_{10.7} = 140$ SFU		High Solar Activity $F_{10.7} = 230$ SFU	
	A	B	A	B	A	B
100-180 km	3.1401475314E+25	-11.532387366	2.1302781218E+23	-10.459869753	3.6572435859E+22	-10.084078484
180-300 km	3.5702302808E+17	-7.9870178011	3.6883393449E+13	-6.1111045267	4.4836934931E+11	-5.2304377430
300-400 km	3.4883419067E+19	-8.7900136027	2.3760454376E+14	-6.4367101996	6.4653842042E+11	-5.2927120099
400-500 km	3.4193579110E+21	-9.5577441366	1.3376579171E+16	-7.1098789385	8.0238678743E+12	-5.7133843080
500-600 km	6.8121896048E+18	-8.5595105119	1.2599509491E+18	-7.8417840857	1.5746908534E+14	-6.1926697178
600-700 km	9.0620295449E+11	-6.0836670624	5.1432928294E+19	-8.4221015808	5.2597040585E+15	-6.741253304
700-800 km	1.0934691244E+7	-4.3533902868	2.0822606336E+19	-8.2850698109	1.2783834984E+17	-7.2286463032
800-900 km	1.1437831846E+5	-3.6702885332	2.1877054342E+16	-7.2588177982	4.9403188705E+17	-7.4310970797

Appendix B

CIRA Curve Fits

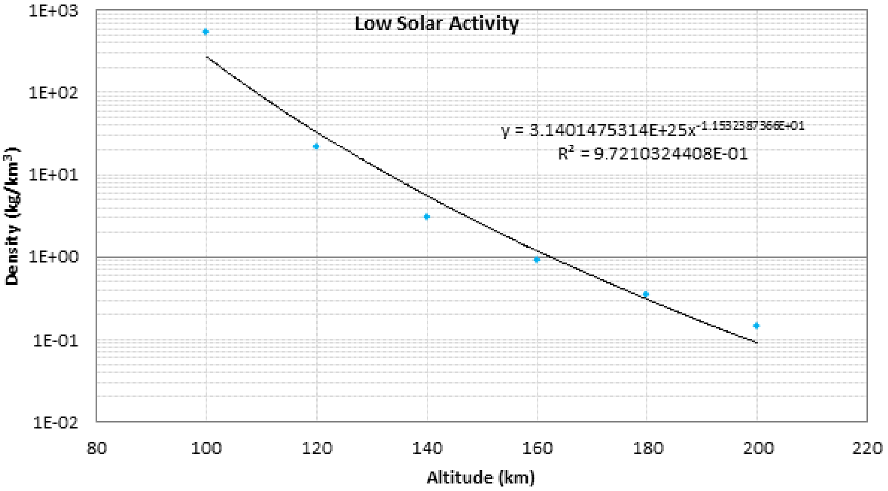

Fig. B.1 Power Curve Segmented Fit for CIRA Atmospheric Density in range 100-180 km at Low Solar Activity Level (N.B. logarithmic y-axis)

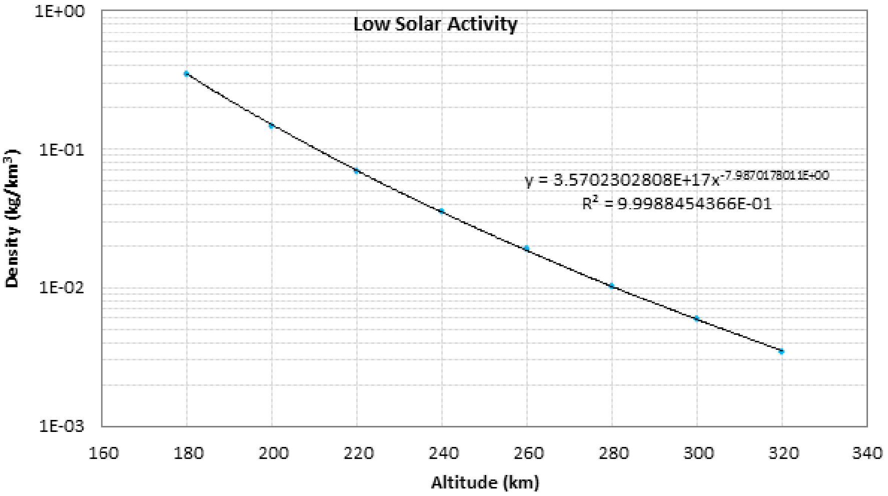

Fig. B.2 Power Curve Segmented Fit for CIRA Atmospheric Density in range 180-300 km at Low Solar Activity Level (N.B. logarithmic y-axis)

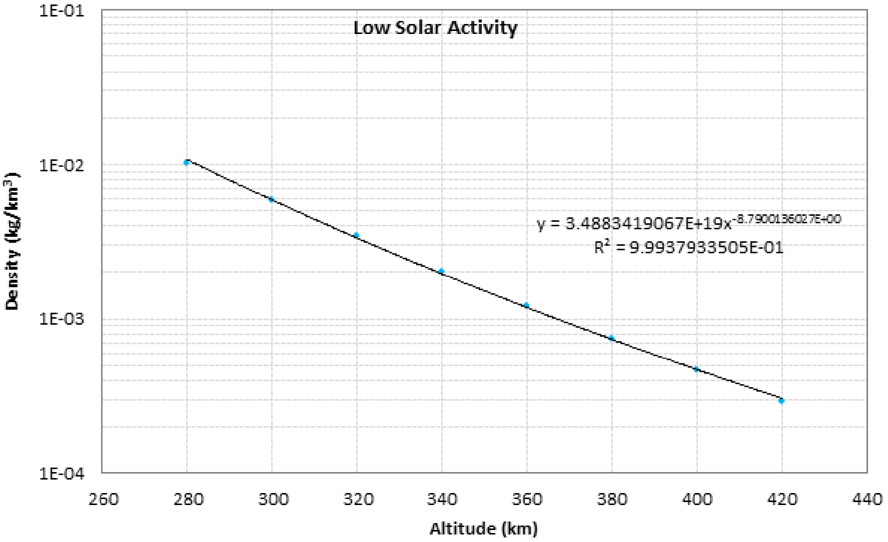

Fig. B.3 Power Curve Segmented Fit for CIRA Atmospheric Density in range 300-400 km at Low Solar Activity Level (N.B. logarithmic y-axis)

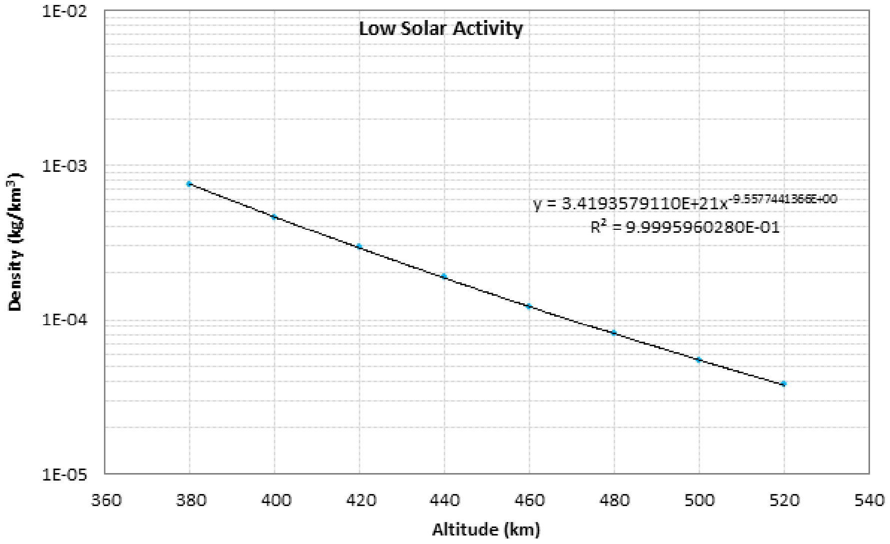

Fig. B.4 Power Curve Segmented Fit for CIRA Atmospheric Density in range 400-500 km at Low Solar Activity Level (N.B. logarithmic y-axis)

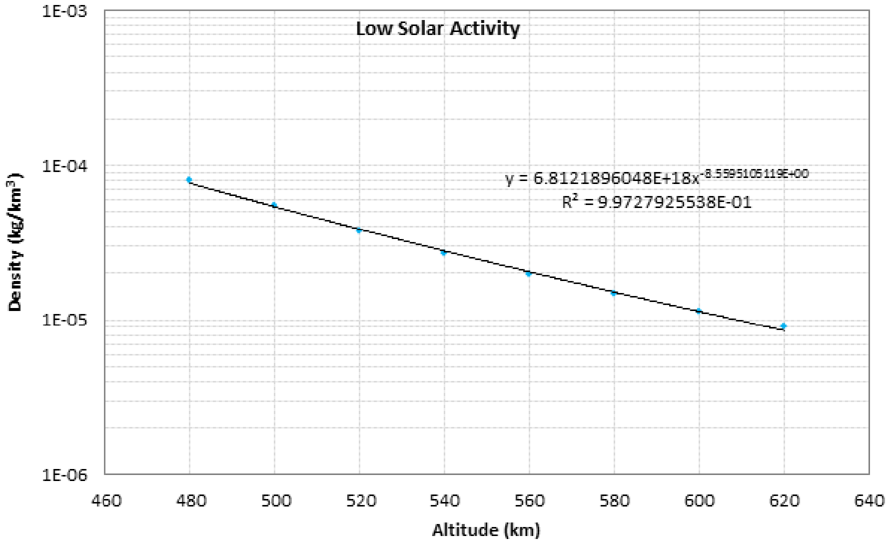

Fig. B.5 Power Curve Segmented Fit for CIRA Atmospheric Density in range 500-600 km at Low Solar Activity Level (N.B. logarithmic y-axis)

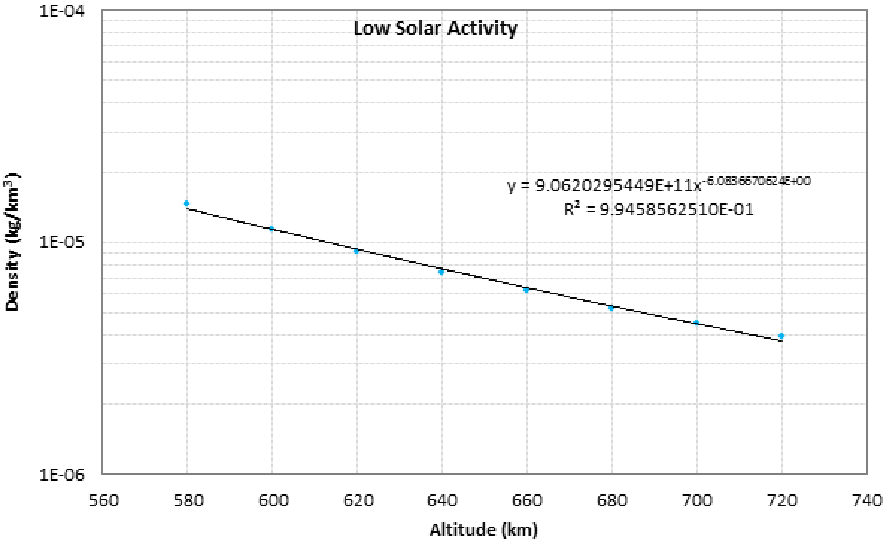

Fig. B.6 Power Curve Segmented Fit for CIRA Atmospheric Density in range 600-700 km at Low Solar Activity Level (N.B. logarithmic y-axis)

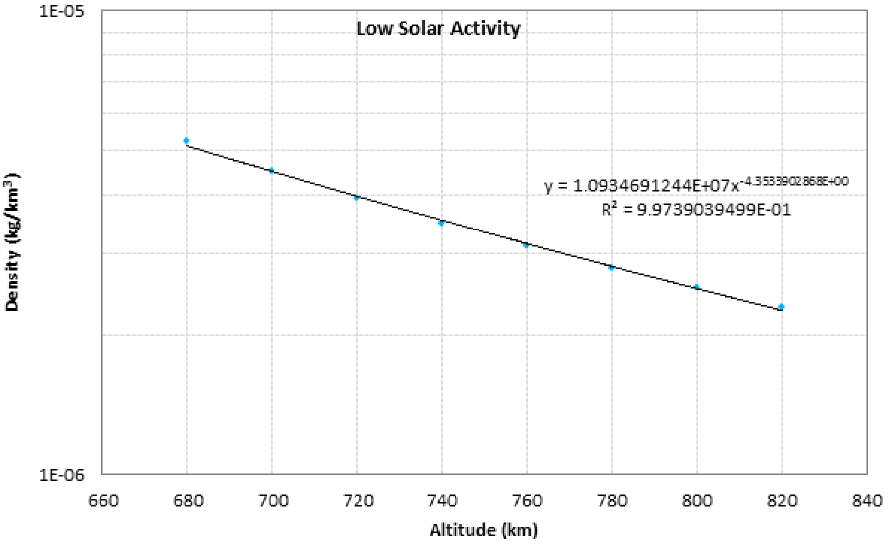

Fig. B.7 Power Curve Segmented Fit for CIRA Atmospheric Density in range 700-800 km at Low Solar Activity Level (N.B. logarithmic y-axis)

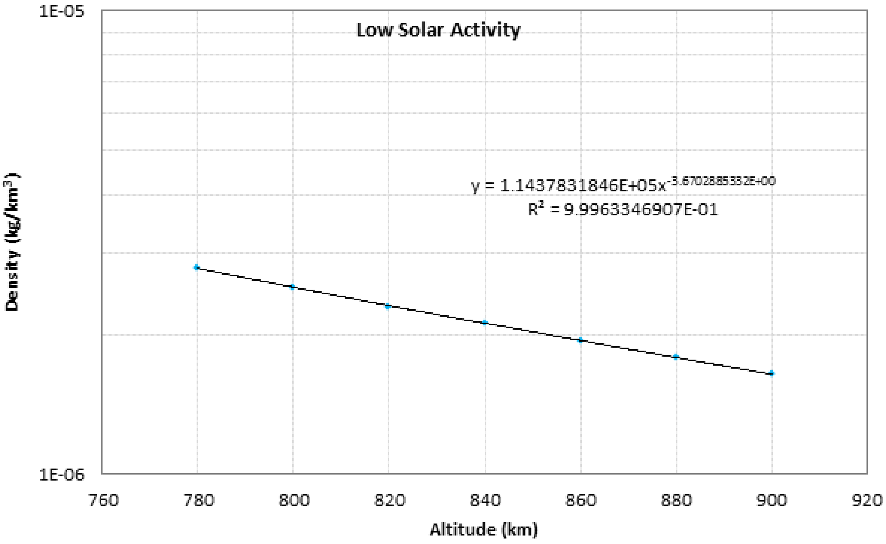

Fig. B.8 Power Curve Segmented Fit for CIRA Atmospheric Density in range 800-900 km at Low Solar Activity Level (N.B. logarithmic y-axis)

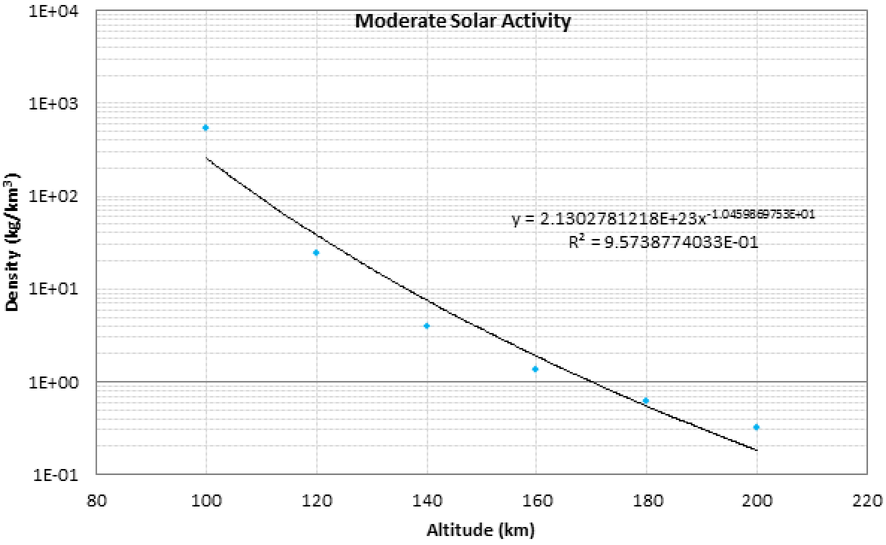

Fig. B.9 Power Curve Segmented Fit for CIRA Atmospheric Density in range 100-180 km at Moderate Solar Activity Level (N.B. logarithmic y-axis)

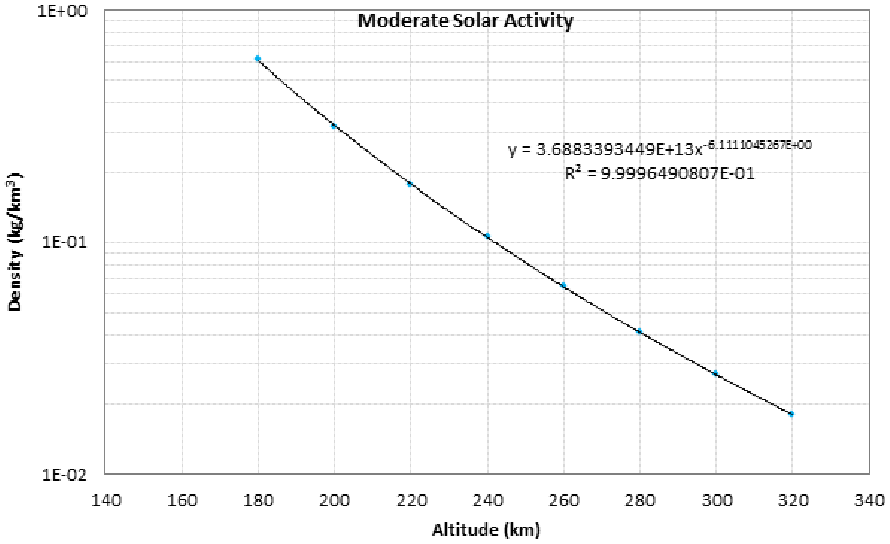

Fig. B.10 Power Curve Segmented Fit for CIRA Atmospheric Density in range 180-300 km at Moderate Solar Activity Level (N.B. logarithmic y-axis)

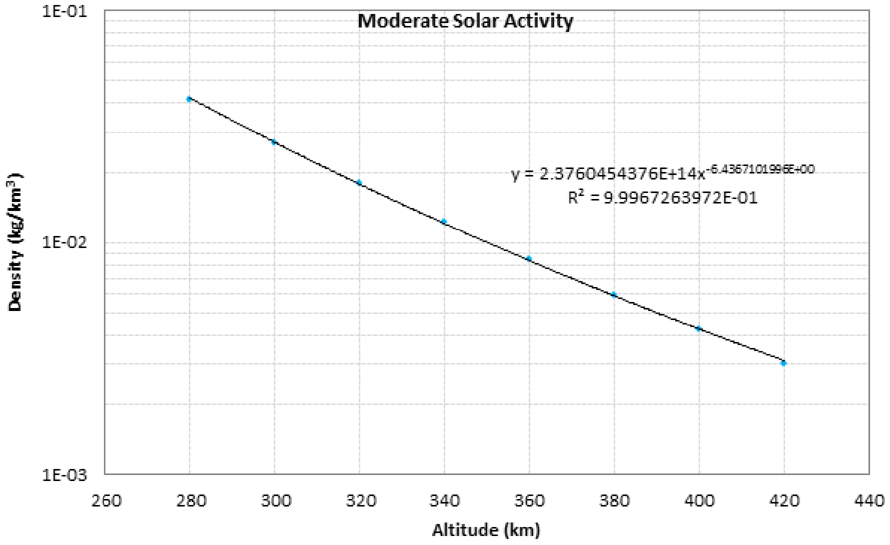

Fig. B.11 Power Curve Segmented Fit for CIRA Atmospheric Density in range 300-400 km at Moderate Solar Activity Level (N.B. logarithmic y-axis)

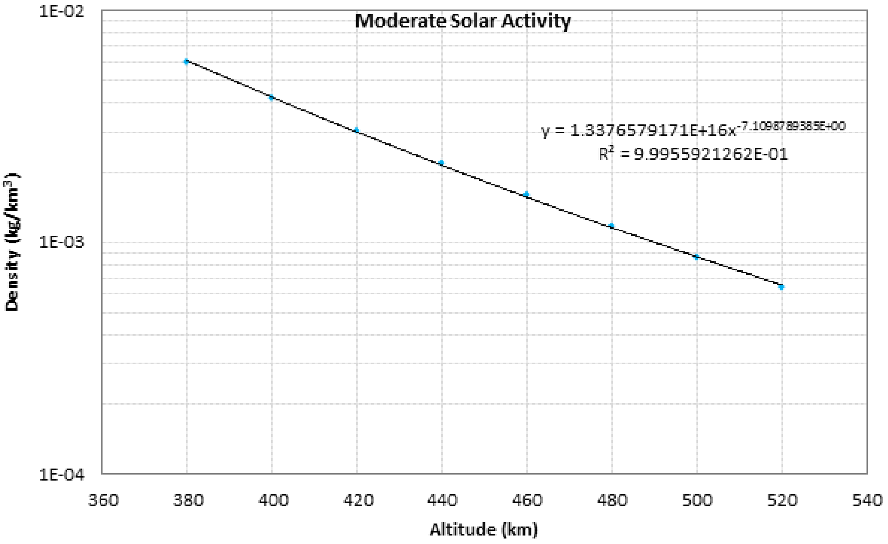

Fig. B.12 Power Curve Segmented Fit for CIRA Atmospheric Density in range 400-500 km at Moderate Solar Activity Level (N.B. logarithmic y-axis)

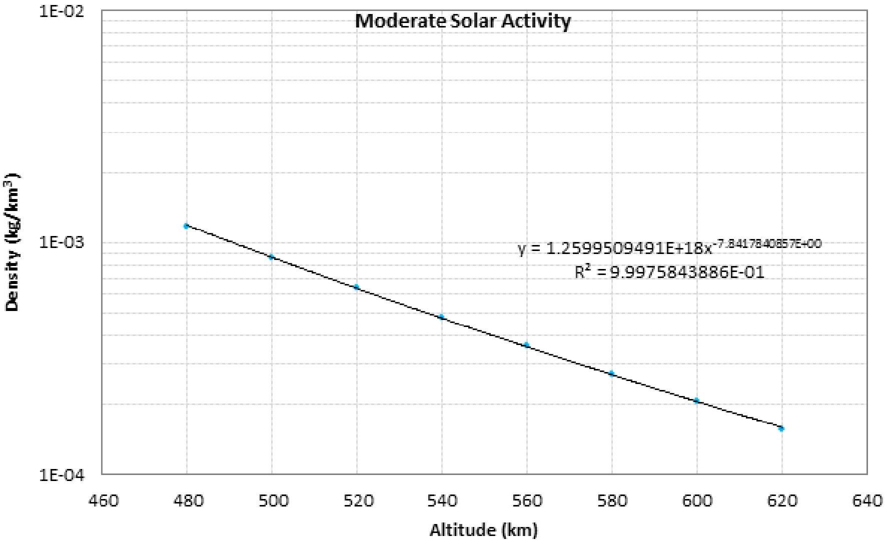

Fig. B.13 Power Curve Segmented Fit for CIRA Atmospheric Density in range 500-600 km at Moderate Solar Activity Level (N.B. logarithmic y-axis)

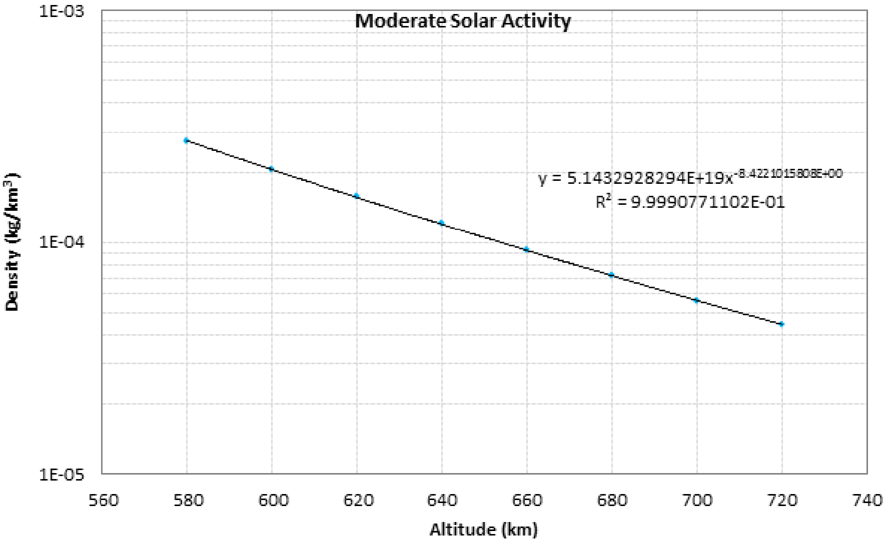

Fig. B.14 Power Curve Segmented Fit for CIRA Atmospheric Density in range 600-700 km at Moderate Solar Activity Level (N.B. logarithmic y-axis)

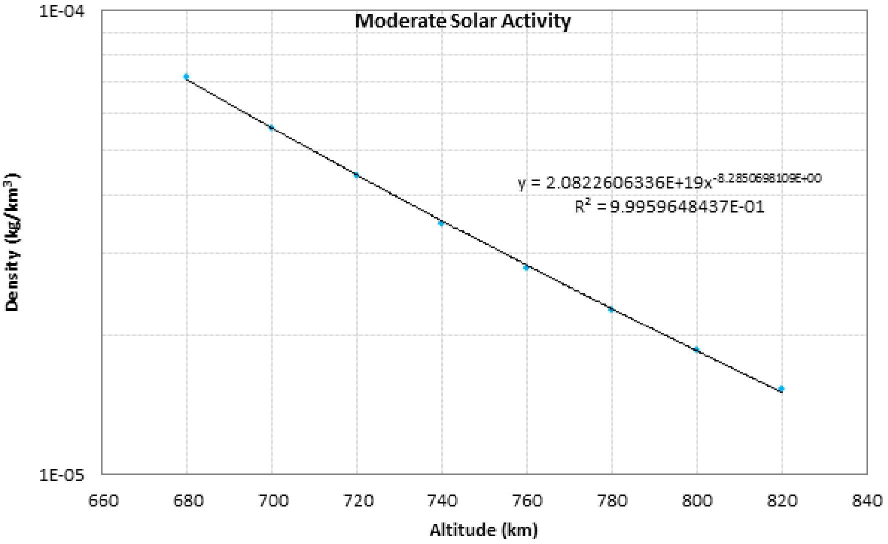

Fig. B.15 Power Curve Segmented Fit for CIRA Atmospheric Density in range 700-800 km at Moderate Solar Activity Level (N.B. logarithmic y-axis)

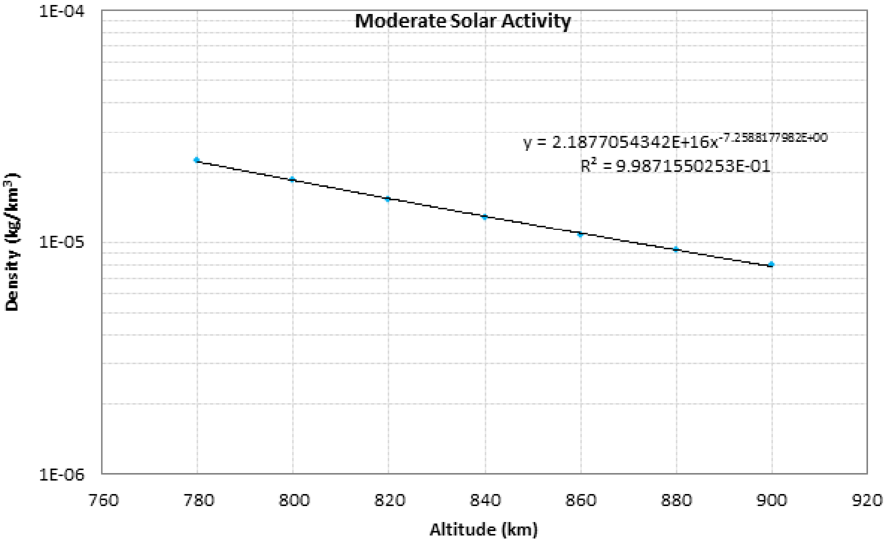

Fig. B.16 Power Curve Segmented Fit for CIRA Atmospheric Density in range 800-900 km at Moderate Solar Activity Level (N.B. logarithmic y-axis)

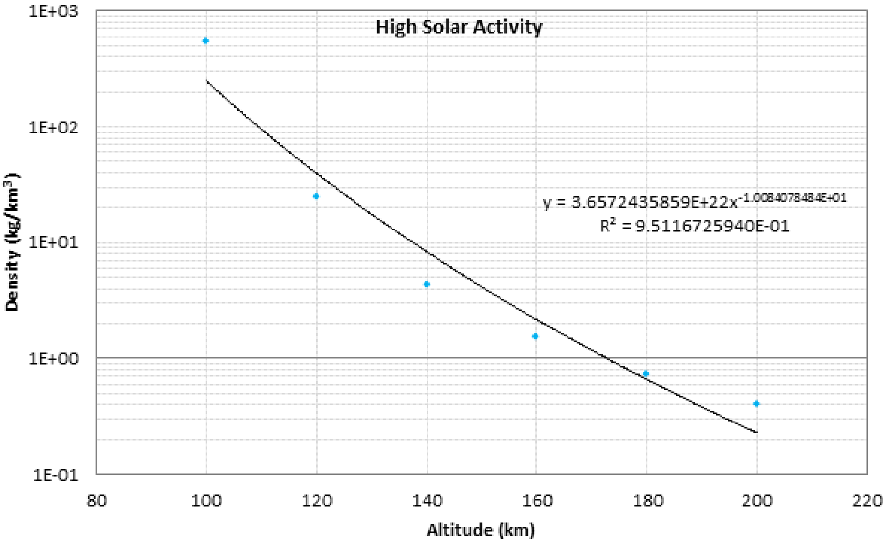

Fig. B.17 Power Curve Segmented Fit for CIRA Atmospheric Density in range 100-180 km at High Solar Activity Level (N.B. logarithmic y-axis)

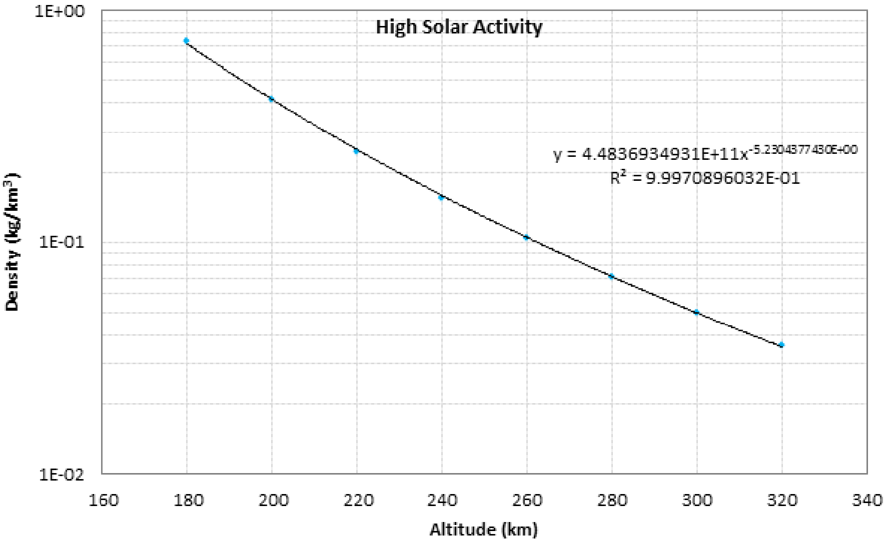

Fig. B.18 Power Curve Segmented Fit for CIRA Atmospheric Density in range 180-300 km at High Solar Activity Level (N.B. logarithmic y-axis)

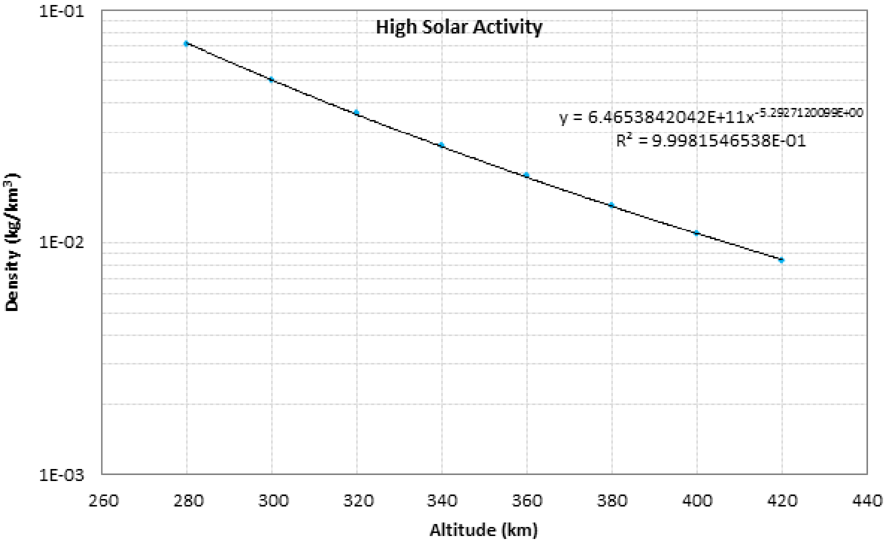

Fig. B.19 Power Curve Segmented Fit for CIRA Atmospheric Density in range 300-400 km at High Solar Activity Level (N.B. logarithmic y-axis)

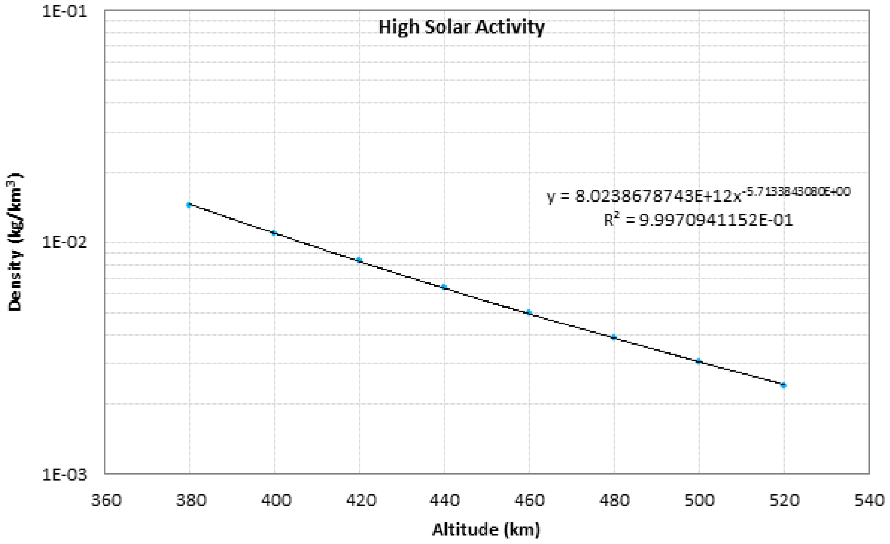

Fig. B.20 Power Curve Segmented Fit for CIRA Atmospheric Density in range 400-500 km at High Solar Activity Level (N.B. logarithmic y-axis)

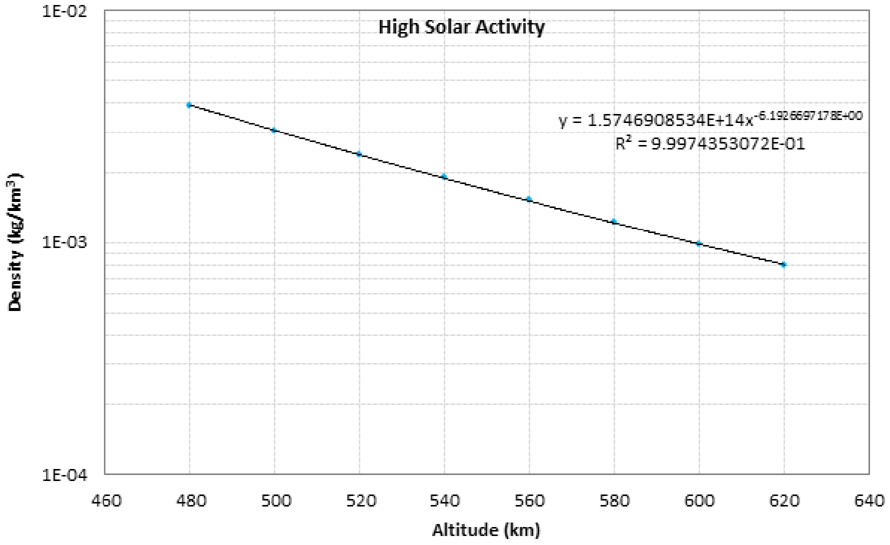

Fig. B.21 Power Curve Segmented Fit for CIRA Atmospheric Density in range 500-600 km at High Solar Activity Level (N.B. logarithmic y-axis)

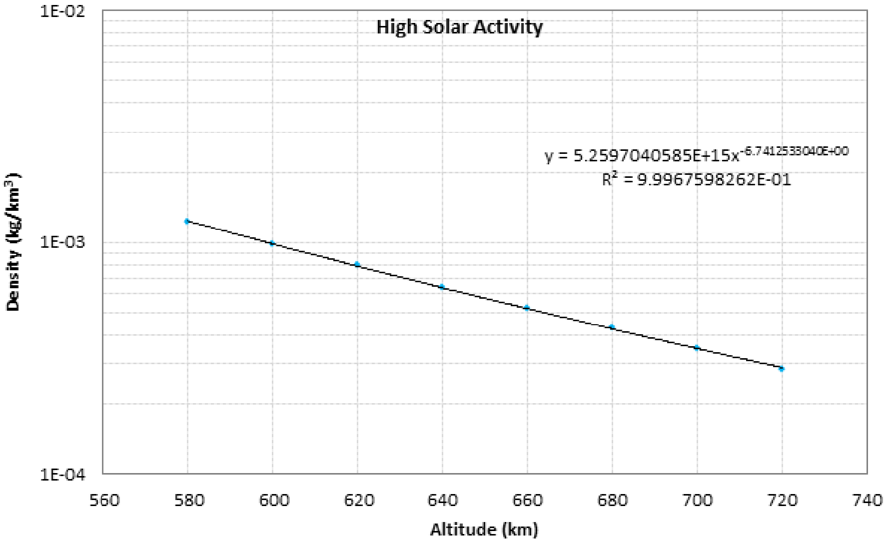

Fig. B.22 Power Curve Segmented Fit for CIRA Atmospheric Density in range 600-700 km at High Solar Activity Level (N.B. logarithmic y-axis)

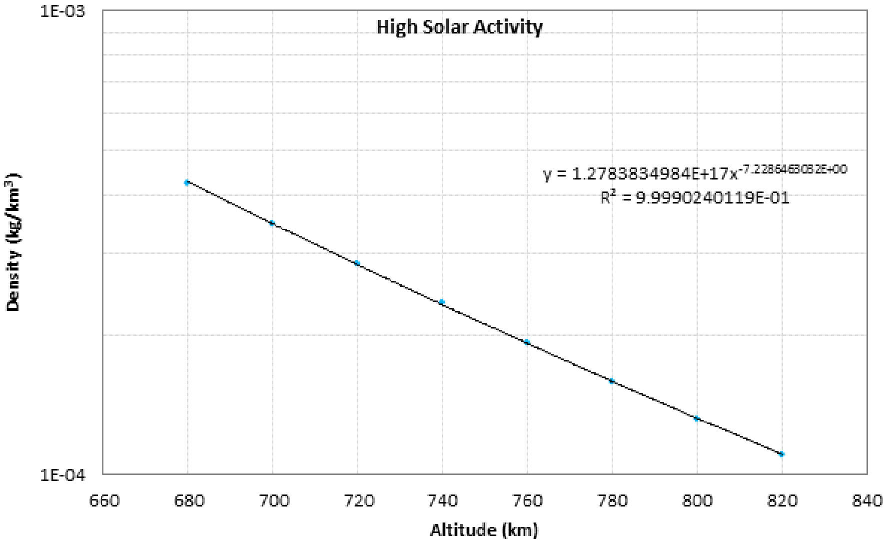

Fig. B.23 Power Curve Segmented Fit for CIRA Atmospheric Density in range 700-800 km at High Solar Activity Level (N.B. logarithmic y-axis)

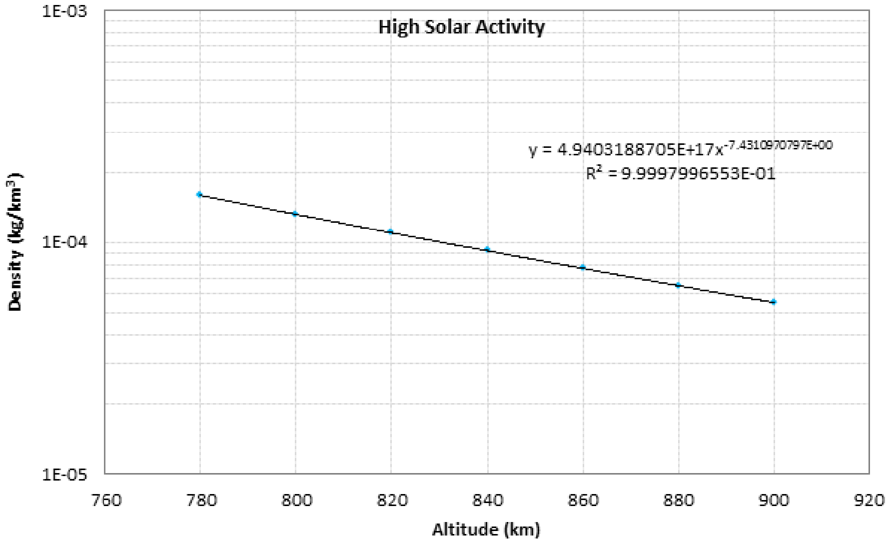

Fig. B.24 Power Curve Segmented Fit for CIRA Atmospheric Density in range 800-900 km at High Solar Activity Level (N.B. logarithmic y-axis)

Appendix C

NRLMSISE Derived Density Model Coefficients

Table C.1 Coefficients for Equation 3.2

Altitude Range	Low Solar Activity $F_{10.7} = 70$ SFU		Moderate Solar Activity $F_{10.7} = 140$ SFU		High Solar Activity $F_{10.7} = 230$ SFU	
	A	B	A	B	A	B
100-1000 km	6.5420811058E+17	-8.0294018845	3.8705227930E+16	-7.3689920764	1.0078104180E+15	-6.6084353925

Table C.2 Coefficients for Equation 3.2

Altitude Range	Low Solar Activity $F_{10.7} = 70$ SFU		Moderate Solar Activity $F_{10.7} = 140$ SFU		High Solar Activity $F_{10.7} = 230$ SFU	
	A	B	A	B	A	B
100-140 km	6.3288680739E+40	-19.0361996491	7.2010273924E+40	-19.0734819569	9.2315659287E+40	-19.1381050575
140-200 km	1.8154369968E+18	-8.2858436967	3.1254971985E+16	-7.4518795850	1.5519787741E+15	-6.8302393492
200-300 km	1.9650569750E+16	-7.4033502790	2.8866982138E+13	-6.0971443754	4.7285076325E+11	-5.2662950161
300-400 km	5.4343980835E+17	-7.9944342183	3.1844414588E+14	-6.5210228262	3.1448303537E+12	-5.5997121608
400-500 km	5.2404895302E+19	-8.7670322700	1.7930345195E+16	-7.2010166173	1.2716290500E+14	-6.2220843906
500-600 km	2.0946988227E+20	-8.9951169517	1.3314305733E+18	-7.9011602607	4.1790580425E+15	-6.7881300949
600-700 km	2.2861129761E+17	-7.9237157666	2.1207022183E+19	-8.3381056397	1.6762694872E+17	-7.3698429007
700-800 km	2.2454743186E+12	-6.1519525504	9.5379981627E+18	-8.2165762802	2.9979230338E+18	-7.8131829090
800-900 km	1.0852561073E+09	-5.0024088253	4.3768222691E+16	-7.4075754840	1.1080367650E+19	-8.0102289341
900-1000 km	6.1199262853E+07	-4.5772155728	2.0759812424E+13	-6.2770569711	4.0715658329E+18	-7.8627865098

Appendix D

Oblateness

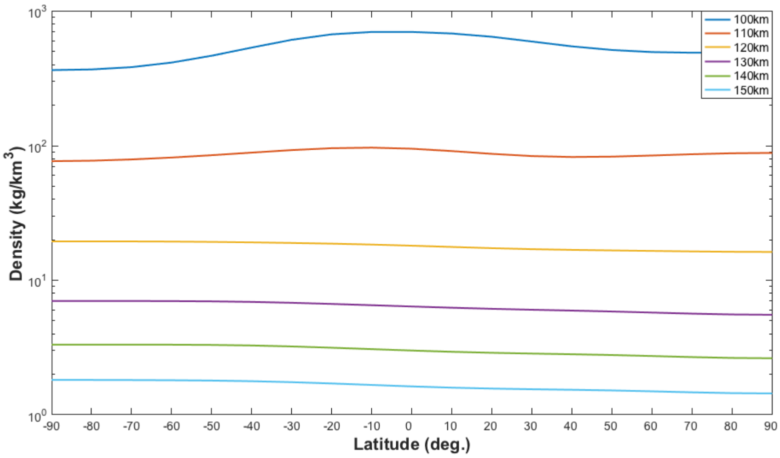

Fig. D.1 Atmospheric oblateness at low solar activity (N.B. logarithmic y-axis)

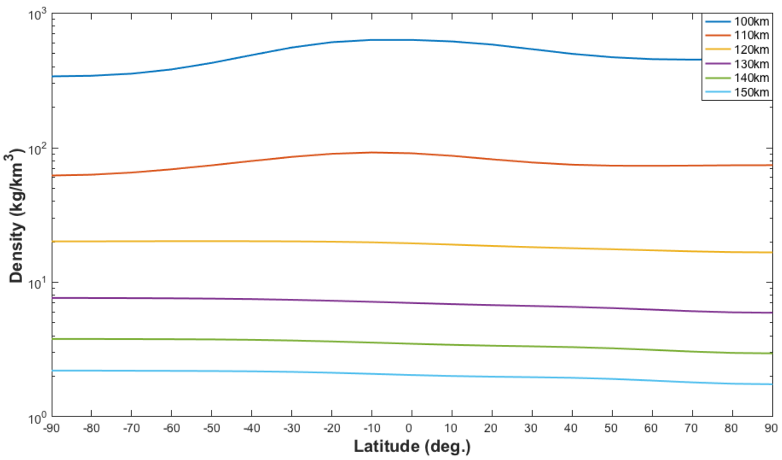

Fig. D.2 Atmospheric oblateness at high solar activity (N.B. logarithmic y-axis)

Appendix E

Diurnal Graphs

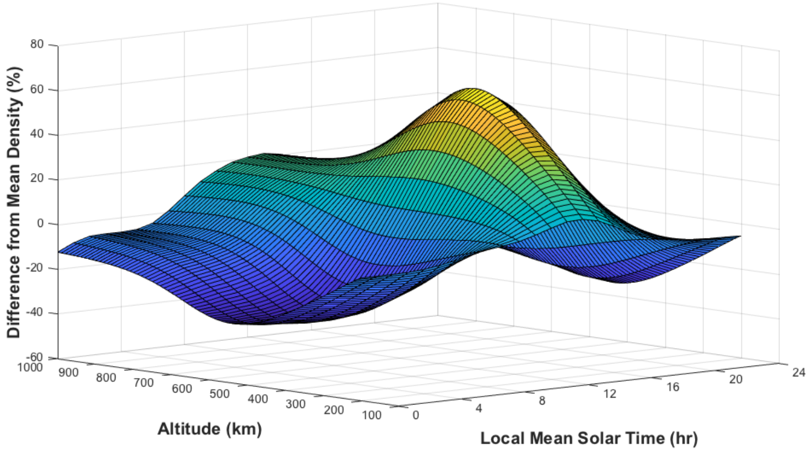

Fig. E.1 3D surface describing density variation at low solar activity ($F_{10.7}$ =70 SFU) due to the diurnal variation

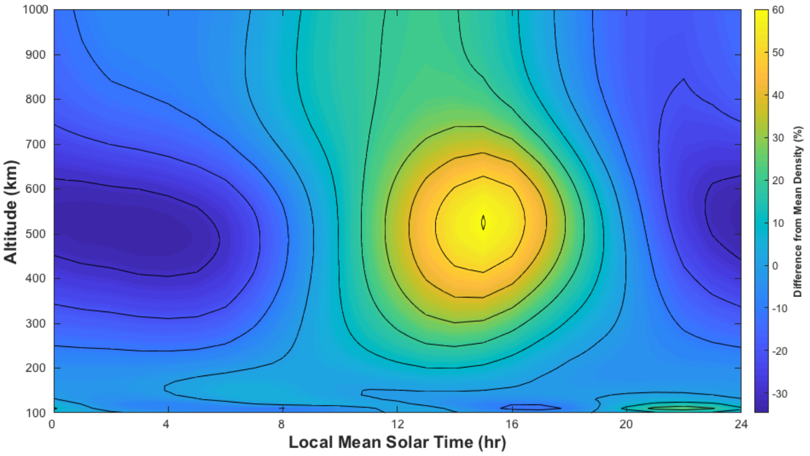

Fig. E.2 Contours describing density variation at low solar activity ($F_{10.7}$ =70 SFU) due to the diurnal variation

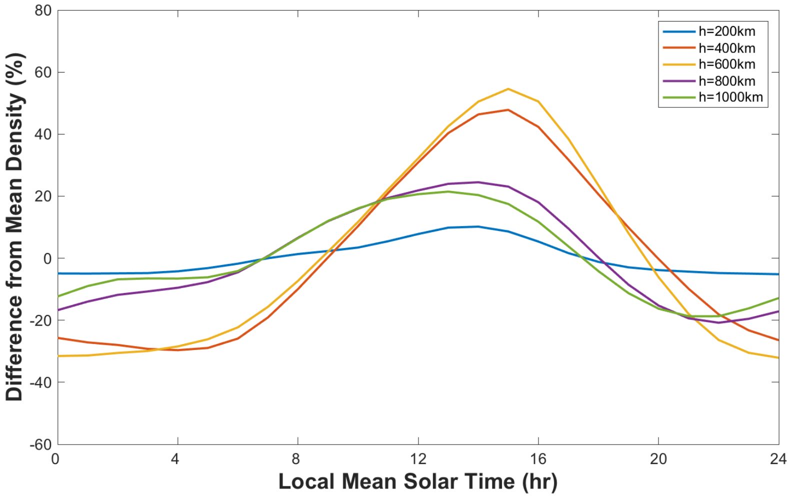

Fig. E.3 Altitude specific curves describing density variation at low solar activity ($F_{10.7}$ =70 SFU) due to the diurnal variation

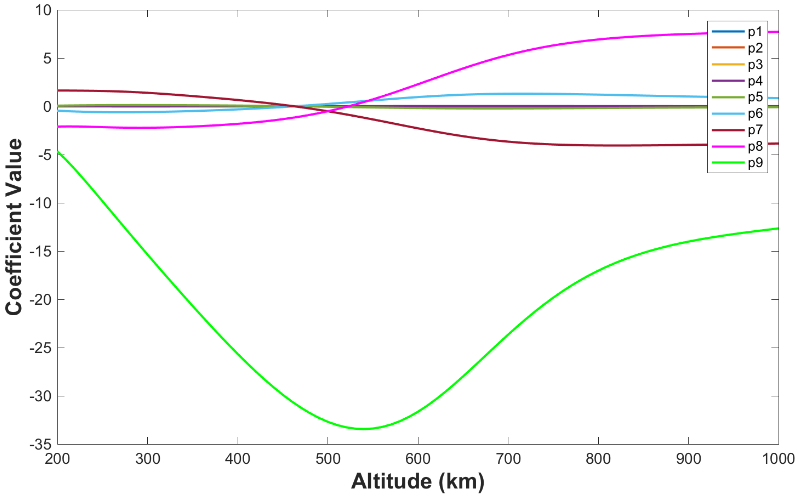

Fig. E.4 Variation due to altitude of coefficients for altitude specific curves from Figure E.3

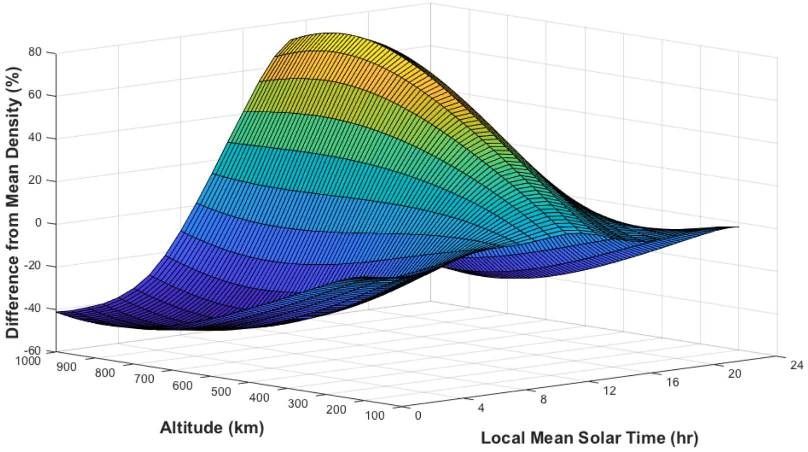

Fig. E.5 3D surface describing density variation at high solar activity ($F_{10.7}$ =230 SFU) due to the diurnal variation

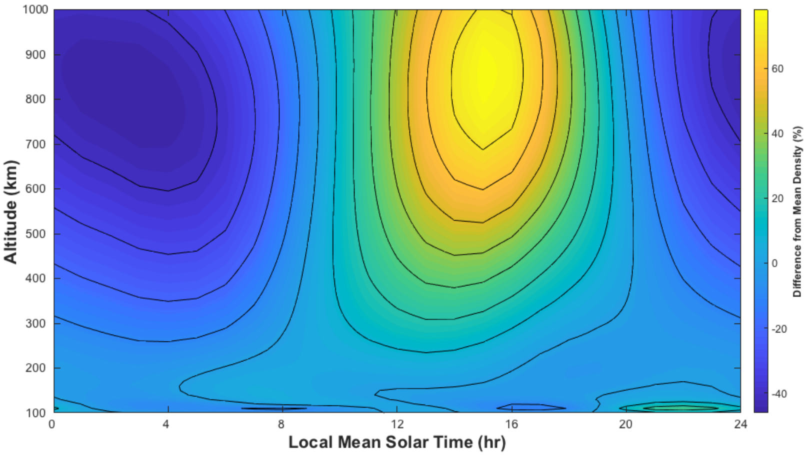

Fig. E.6 Contours describing density variation at high solar activity ($F_{10.7}$ =230 SFU) due to the diurnal variation

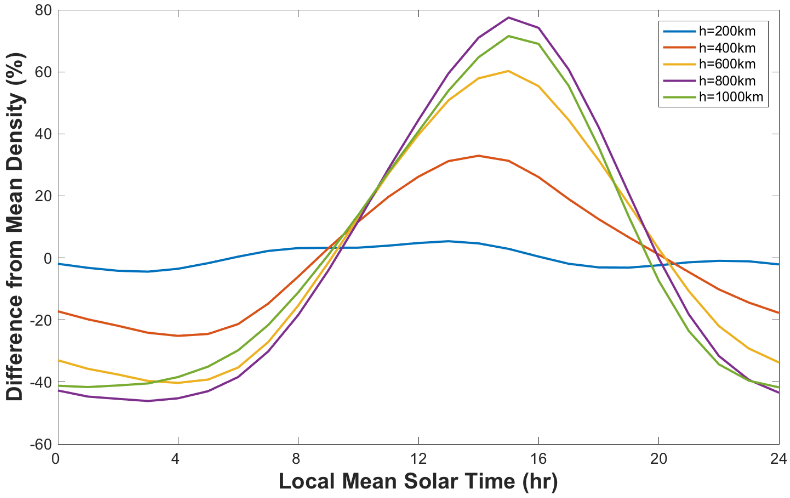

Fig. E.7 Altitude specific curves describing density variation at low solar activity ($F_{10.7}$ =230 SFU) due to the diurnal variation

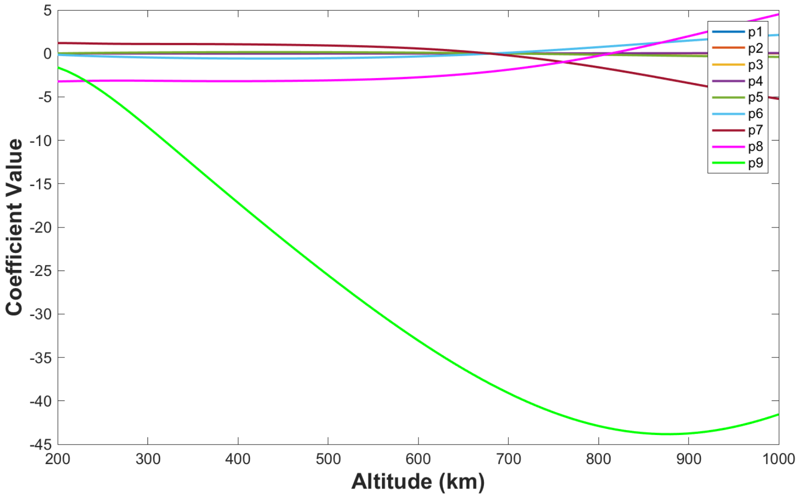

Fig. E.8 Variation due to altitude of coefficients for altitude specific curves from Figure E.7

Appendix F

Diurnal Coefficients

Table F.1 Coefficients for equation 3.10 and 3.11 for low solar activity

	c_1	c_2	c_3
P_1	-2.0521761643E-27	9.9878640740E-24	-2.0414226615E-20
P_2	1.8128769405E-25	-8.8722773217E-22	1.8244293848E-18
P_3	-6.2417357435E-24	3.0784508836E-20	-6.3830447246E-17
P_4	1.0494056896E-22	-5.2333388005E-19	1.0977618414E-15
P_5	-8.7797556306E-22	4.4514515673E-18	-9.4950151599E-15
P_6	3.1918485371E-21	-1.6679988614E-17	3.6619679414E-14
P_7	-1.8704972034E-21	1.2452043719E-17	-3.2691491701E-14
P_8	-5.0756593026E-21	1.9160874670E-17	-2.7450047986E-14
P_9	-5.0069357930E-20	2.2483309409E-16	-4.1865972663E-13

	c_4	c_5	c_6
P_1	2.2772838779E-17	-1.5117116171E-14	6.1253990034E-12
P_2	-2.0486664262E-15	1.3695437307E-12	-5.5895958584E-10
P_3	7.2311454523E-14	-4.8787327739E-11	2.0095640399E-08
P_4	-1.2586486874E-12	8.5957556067E-10	-3.5824557521E-07
P_5	1.1070229717E-11	-7.6845713414E-09	3.2515979124E-06
P_6	-4.3872104048E-11	3.1226861136E-08	-1.3507171180E-05
P_7	4.4924369376E-11	-3.5555607267E-08	1.6672633293E-05
P_8	1.7402860214E-11	-3.0185743304E-09	-1.9501227002E-06
P_9	4.1947778761E-10	-2.4663828685E-07	8.7577728361E-05

	c_7	c_8	c_9
P_1	-1.4933094520E-09	2.0229066197E-07	-1.1648827313E-05
P_2	1.3723634789E-07	-1.8719397276E-05	1.0830096355E-03
P_3	-4.9768795670E-06	6.8432790881E-04	-3.9793936253E-02
P_4	8.9671346138E-05	-1.2442628561E-02	7.2710124714E-01
P_5	-8.2457155093E-04	1.1553813122E-01	-6.7716916946E+00
P_6	3.4865748559E-03	-4.9370064717E-01	2.8840164963E+01
P_7	-4.5658022041E-03	6.6907137304E-01	-3.8537123731E+01
P_8	1.1580281332E-03	-2.3469176167E-01	1.4976562206E+01
P_9	-1.8468006541E-02	2.0198050999E+00	-8.5960811563E+01

Table F.2 Coefficients for equation 3.10 and 3.11 for moderate solar activity

	c_1	c_2	c_3
P_1	3.9463911501E-28	-1.8108950647E-24	3.4227638418E-21
P_2	-3.4958410738E-26	1.6096017656E-22	-3.0492073072E-19
P_3	1.2213406086E-24	-5.6577634221E-21	1.0772597126E-17
P_4	-2.1414367877E-23	1.0027314326E-19	-1.9289715160E-16
P_5	2.0036591477E-22	-9.5602882522E-19	1.8759048344E-15
P_6	-1.0096429729E-21	4.9723825507E-18	-1.0113138837E-14
P_7	2.6933088816E-21	-1.3920194004E-17	2.9927759600E-14
P_8	-2.5875905178E-21	1.4197225227E-17	-3.2251936816E-14
P_9	-7.7268694892E-22	9.7956694081E-18	-3.3469912423E-14

	c_4	c_5	c_6
P_1	-3.4557206046E-18	2.0248655071E-15	-6.9123444804E-13
P_2	3.0786605148E-16	-1.7966285272E-13	6.0643935000E-11
P_3	-1.0908818988E-14	6.3597825883E-12	-2.1305393742E-09
P_4	1.9709333653E-13	-1.1564702148E-10	3.8881957030E-08
P_5	-1.9571501803E-12	1.1747098014E-09	-4.0680326220E-07
P_6	1.1003273874E-11	-6.9550371847E-09	2.5913382085E-06
P_7	-3.4760839191E-11	2.3783044016E-08	-9.8199606522E-06
P_8	3.9465557385E-11	-2.8432196176E-08	1.2400443904E-05
P_9	5.3414926274E-11	-4.6932864928E-08	2.4230498219E-05

	c_7	c_8	c_9
P_1	1.2138157927E-10	-5.6918458613E-09	-5.3163924049E-07
P_2	-1.0334281757E-08	3.8703732628E-07	5.7212733096E-05
P_3	3.5494698911E-07	-1.0667720874E-05	-2.2676853612E-03
P_4	-6.5071279959E-06	2.0479436123E-04	3.9165584167E-02
P_5	7.2748693689E-05	-3.8270155457E-03	-2.1632677057E-01
P_6	-5.3632236726E-04	5.0500633925E-02	-1.4816918855E+00
P_7	2.3850978701E-03	-3.1216989040E-01	1.8323709494E+01
P_8	-3.2028240624E-03	4.4747051432E-01	-2.8523318995E+01
P_9	-7.3326534153E-03	1.1066336074E+00	-6.4415769822E+01

Table F.3 Coefficients for equation 3.10 and 3.11 for high solar activity

	c_1	c_2	c_3
P_1	8.3604667846E-29	-4.3161285535E-25	9.2682190234E-22
P_2	-6.9238207534E-27	3.5821403031E-23	-7.6876274421E-20
P_3	2.1722664192E-25	-1.1308112700E-21	2.4323021126E-18
P_4	-3.1055341843E-24	1.6465399683E-20	-3.5819608848E-17
P_5	1.7556798006E-23	-1.0026173598E-19	2.2960814991E-16
P_6	2.8343194801E-24	9.0529913921E-20	-3.8277467026E-16
P_7	-1.5984696718E-22	3.3674567050E-19	2.9483042276E-16
P_8	-1.4101940496E-22	1.1935294084E-18	-3.6773607982E-15
P_9	-4.2780295215E-21	2.2578804797E-17	-5.1424894358E-14

	c_4	c_5	c_6
P_1	-1.0698573995E-18	7.2070702581E-16	-2.8423394174E-13
P_2	8.8272094356E-17	-5.8713001815E-14	2.2574454040E-11
P_3	-2.7804823868E-15	1.8219055334E-12	-6.7759736745E-10
P_4	4.0963342168E-14	-2.6412822759E-11	9.3951070265E-09
P_5	-2.6938032004E-13	1.7267193735E-10	-5.8151714303E-08
P_6	5.9112125921E-13	-4.3916064794E-10	1.6326104033E-07
P_7	-1.4656337026E-12	1.7351369841E-09	-1.0323507591E-06
P_8	5.6947001638E-12	-4.9833046714E-09	2.5933080516E-06
P_9	6.5744874379E-11	-5.1370345861E-08	2.5112160552E-05

	c_7	c_8	c_9
P_1	5.5943720921E-11	-1.6409201496E-09	-5.3113583042E-07
P_2	-4.1373737579E-09	-6.1189586792E-09	5.8222883272E-05
P_3	1.1158514607E-07	5.9122774998E-06	-2.4296785658E-03
P_4	-1.2913410751E-06	-2.0093614894E-04	4.7956103233E-02
P_5	5.5813685296E-06	2.4121860922E-03	-4.3513698061E-01
P_6	-1.8246671289E-05	-6.5466294698E-03	1.1164197050E+00
P_7	3.3975372706E-04	-5.9276334769E-02	5.4054427947E+00
P_8	-7.9451489444E-04	1.3125140436E-01	-1.2080015717E+01
P_9	-7.4894208702E-03	1.1550638820E+00	-6.9774434895E+01

Appendix G

Diurnal Density vs. LMST

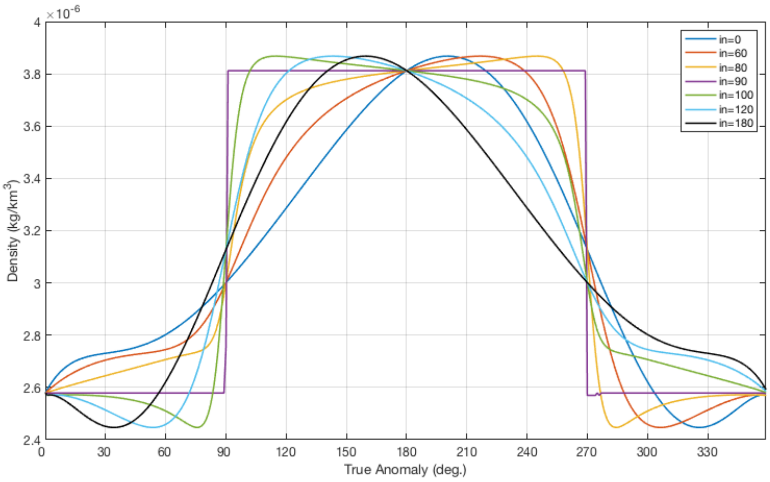

Fig. G.1 Change in density over 1 orbit revolution due to the diurnal variation for a satellite at 800 km altitude and various inclinations during low solar activity ($F_{10.7}$ =70 SFU)

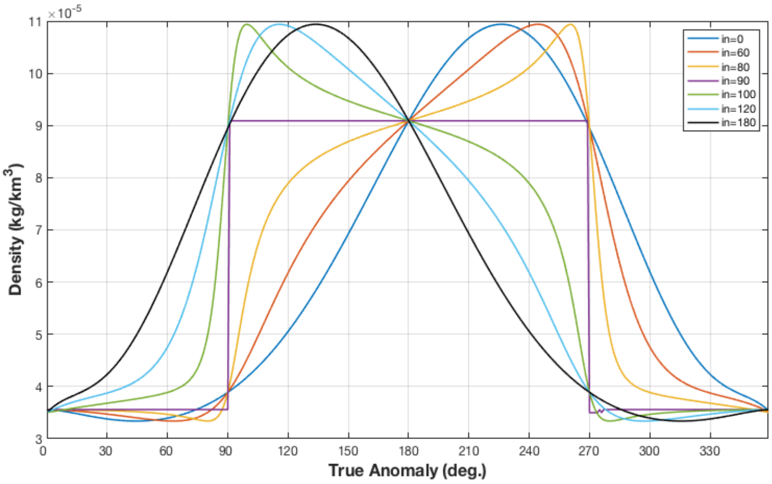

Fig. G.2 Change in density over 1 orbit revolution due to the diurnal variation for a satellite at 800 km altitude and various inclinations during high solar activity ($F_{10.7}$ =230 SFU)

Appendix H

Difference in Density due to Diurnal Effect

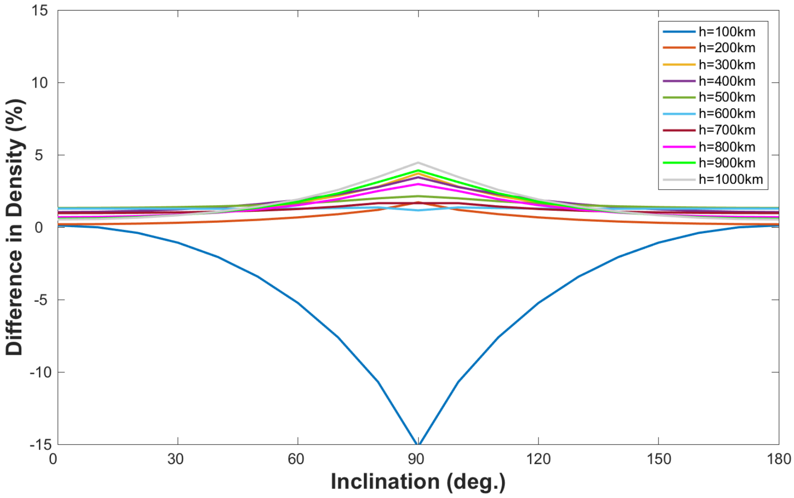

Fig. H.1 Percentage difference in density when comparing the mean density given by the diurnally varying atmospheric model and the mean density from the spherically-symmetrical atmospheric model for a 12am-12pm orbit during low solar activity ($F_{10.7}$ =70 SFU)

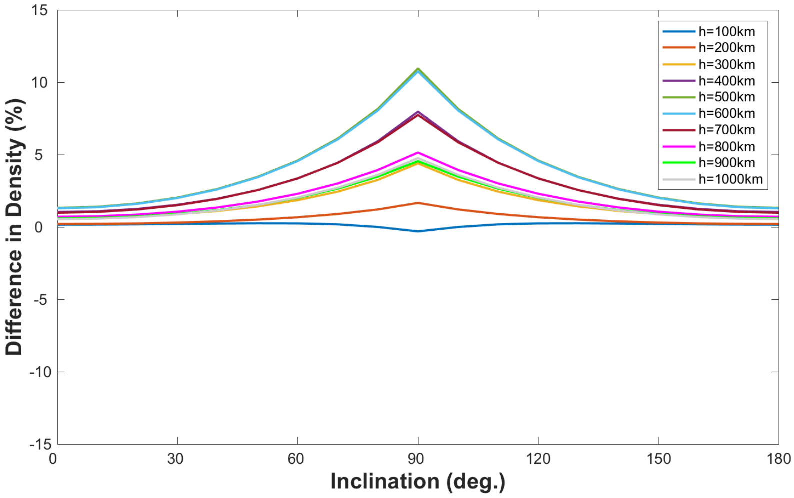

Fig. H.2 Percentage difference in density when comparing the mean density given by the diurnally varying atmospheric model and the mean density from the spherically-symmetrical atmospheric model for a 3am-3pm orbit during low solar activity ($F_{10.7}$ =70 SFU)

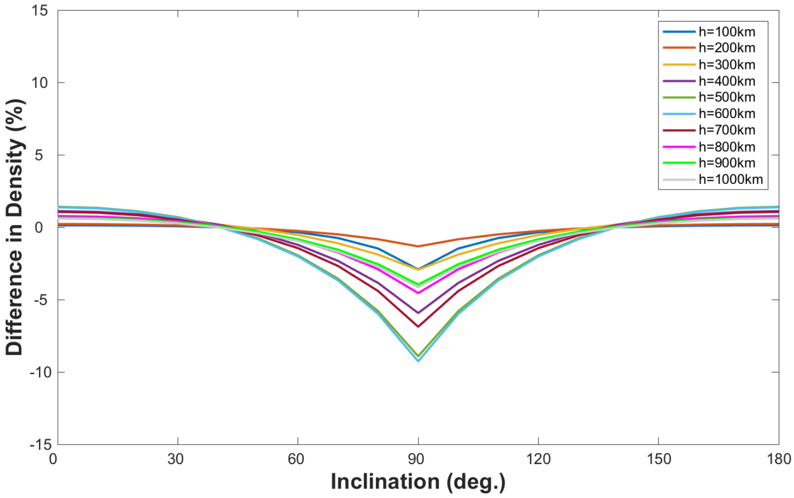

Fig. H.3 Percentage difference in density when comparing the mean density given by the diurnally varying atmospheric model and the mean density from the spherically-symmetrical atmospheric model for a 9am-9pm orbit during low solar activity ($F_{10.7}$ =70 SFU)

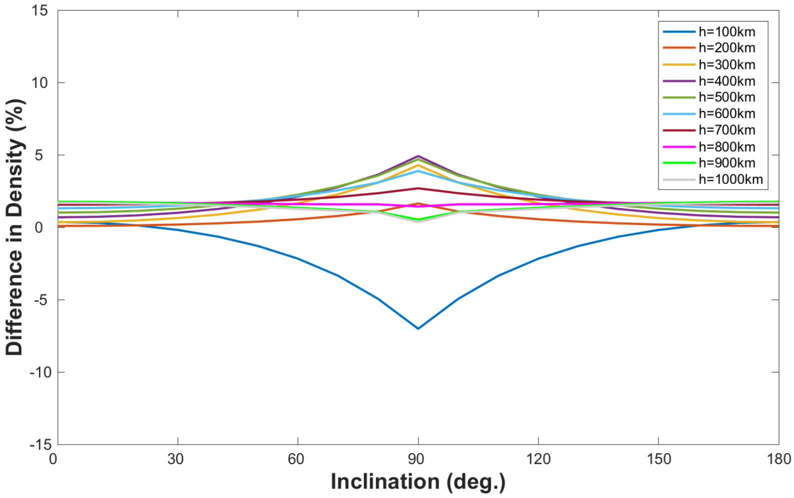

Fig. H.4 Percentage difference in density when comparing the mean density given by the diurnally varying atmospheric model and the mean density from the spherically-symmetrical atmospheric model for a 12am-12pm orbit during high solar activity ($F_{10.7}$ =230 SFU)

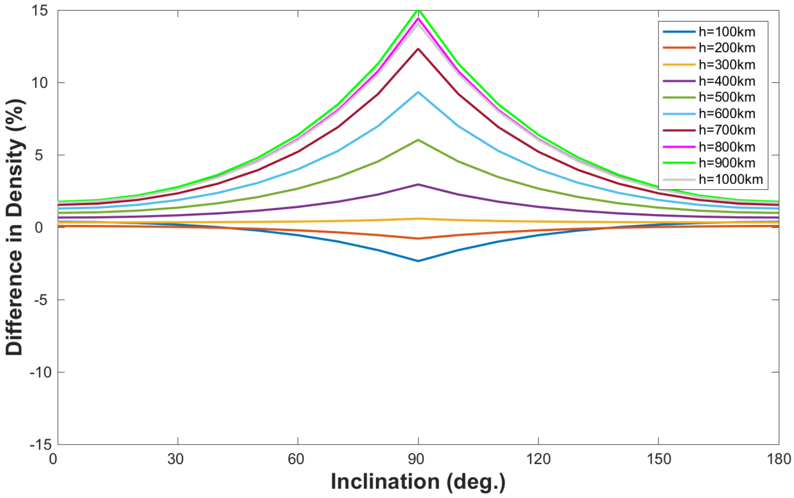

Fig. H.5 Percentage difference in density when comparing the mean density given by the diurnally varying atmospheric model and the mean density from the spherically-symmetrical atmospheric model for a 3am-3pm orbit during high solar activity ($F_{10.7}$ =230 SFU)

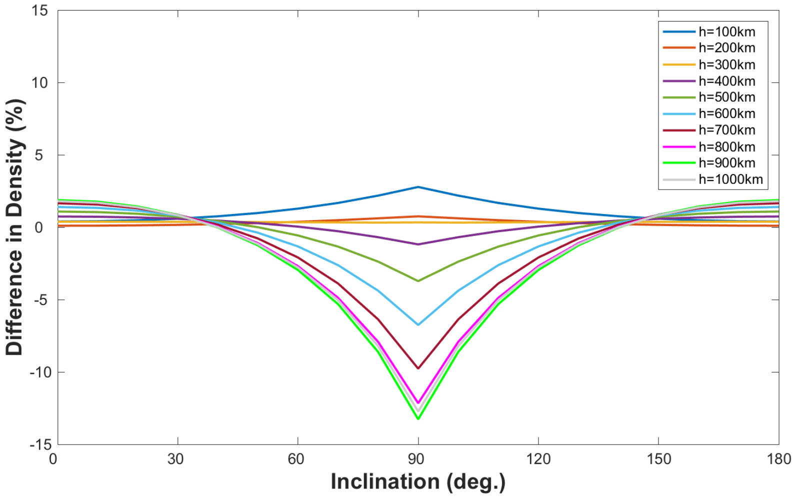

Fig. H.6 Percentage difference in density when comparing the mean density given by the diurnally varying atmospheric model and the mean density from the spherically-symmetrical atmospheric model for a 9am-9pm orbit during high solar activity ($F_{10.7}$ =230 SFU)